

UNIVERSITÀ DEGLI STUDI DI SALERNO

DIPARTIMENTO DI FISICA "E.R. CAIANIELLO"



DOCTORAL THESIS IN MATHEMATICS, PHYSICS AND APPLICATIONS

GRAVITATIONAL LENSING BY MASSIVE AND EXOTIC OBJECTS

Silvia Pietroni

Supervisor: Prof. Valerio Bozza

Coordinator: Prof.ssa Patrizia Longobardi

XXXV CYCLE 2019-2022

A mamma

Vorrei poter invertire lo scorrere del tempo per poterti riabbracciare ancora una volta.

ACKNOWLEDGEMENTS

"Mi fermo e non faccio nulla. Non succede nulla. Non penso nulla.

Ascolto lo scorrere del tempo."

Carlo Rovelli, L'ordine del tempo

In questo intreccio di linee temporali che costituiscono la vita sono riuscita a giungere alla fine di un lungo, importante e faticoso percorso.

Dieci anni fa mi presentai in segreteria alla Sapienza, con il modulo per la rinuncia agli studi a cinque esami dalla fine della laurea. Il segretario mi fece desistere ed aveva ragione: mi sono laureata, ho tentato e fallito un dottorato a Parigi, sto per concludere un dottorato a Salerno ed ho vinto due assegni di ricerca a Napoli.

Sono stati anni intensi, anni in cui la vita mi ha portato via delle persone, anni di pandemia. Ma poi in un modo o nell'altro si ritorna a vivere.

Ringrazio il professor Valerio Bozza per questa opportunità di crescita professionale, il professor Costantino Sigismondi per non aver mai smesso di credere in me, il professor Giovanni Bachelet che mi ha sostenuto nel delicato percorso di rientro agli studi, il professor Jorge Rueda per avermi insegnato le basi di questo mestiere meraviglioso.

Ringrazio mio padre che continua a resistere nella tempesta.

Ringrazio gli amici di sempre per essermi stati vicino, gli amici fisici, gli amici in giro per il mondo, i miei fantastici colleghi campani. Anche se molti rapporti adesso sono cambiati vi ringrazio per esserci stati.

Dedico questa tesi a mia madre e a tutte le donne della mia famiglia che non ci sono più e che non hanno avuto la possibilità di studiare.

A loro va tutto il mio amore.

Abstract

Space-time is curved by the presence of massive bodies and this curvature influences the motion of the bodies themselves: this leads to a geometry in constant evolution. One of the consequences is that even light, supposed to be massless, bends its trajectory while passing close to a massive body. The study of light bending started in the XVIII century and a lot of progress was done so far.

Gravitational lensing is an important tool in astrophysics and in cosmology widely used to study both populations of compact objects (including exoplanets, black holes and other stellar remnants), and extended objects, such as galaxies, clusters of galaxies and large-scale structures. Since most of the mysteries of our Universe do not show up in observations based on electromagnetic interactions, gravitational lensing is more and more employed to study the dark side of the Universe, including dark matter, dark energy, and any kind of exotic matter (such as wormholes) conjectured by theorists.

In the introduction in Chapter 1 we run across the history of gravitational lensing through the explanation of the lens equation, the magnification of images, the description of critical curves and caustics, the binary lenses in the standard theory. In Chapter 2 we focus on gravitational lensing by objects with $1/r^n$ potential giving a complete atlas of the critical curves and caustics in mixed binary systems such as pairs of galaxies with different halos, or cases in which one object is made up of exotic matter and the other one is a normal star or in the case of wormholes when they appear in non-isolated systems.

After the amazing discoveries by the GRAVITY collaboration in the last few years on the star S2 orbiting the black hole Sgr A* in the center of the Milky Way, we present in Chapter 3 a detailed investigation of the impact of gravitational lensing on the reconstruction of stellar orbits around this massive black hole.

Finally, in Chapter 4 we draw the conclusions of this thesis.

CONTENTS

Acknowledgements	2
List of Figures	5
List of Tables	6
1 Introduction	7
1.1 History of Gravitational Lensing	7
1.2 The Lens Equation	9
1.3 Magnification	14
1.4 Critical Curves and Caustics	16
1.5 The Binary Lens	18
2 Gravitational Lensing by Objects with $1/r^n$ Potential	21
2.1 Motivations	21
2.2 Exotic Metrics	23
2.3 The Lens Equation for Exotic Lenses	24
2.4 The Standard Binary Lens Composed by Exotic Objects	25
2.5 The Mixed Binary Lens	26
2.6 Critical curves and caustics for exotic lenses	27
2.6.1 Equal-strength binaries	28
2.6.2 Unequal-strength binary	34
2.6.3 Reversed unequal-strength binary	37
2.7 Transitions between different topologies	40
2.8 Analytical Approximations	43

2.8.1	Wide Binary	43
2.8.2	Extremely unequal-strength ratio limit	44
2.9	Discussion	48
3	From Theory to Observational Effects: S2, Sgr A* and the S-stars	50
3.1	Motivations	50
3.2	The GRAVITY Instrument	53
3.3	The stars S2, S38 and S55	55
3.3.1	Orbital parameters of the real and apparent orbits	58
3.4	Gravitational lensing by Sgr A*	60
3.5	Impact of gravitational lensing on the reconstruction of the orbits of S- stars	62
3.6	Exploring Gravitational lensing at various semimajor axes and inclinations	67
3.7	Discussion	73
4	Conclusions	75

LIST OF FIGURES

1.1	Deflection of light by a massive compact object, credits: Chiara Melchiorre.	8
1.2	The 1919 Edition of Cosmic Times. Image Credit: NASA.	8
1.3	Figure a): Weak lensing; Figure b): Strong lensing. Credits: Chiara Melchiorre. . . .	11
1.4	Gravitational lens scheme. Credits: Valerio Bozza.	12
1.5	Critical curves and caustics for $\gamma = 1$ in the standard binary lenses.	20
2.1	Critical curves and caustics in the equal-strength binary, wide separation. Here and in the following figures the lens on the left has $n = 1$ and the lens on the right has variable m	29
2.2	Critical curves and caustics in the equal-strength binary, intermediate-wide transition.	29
2.3	Critical curves and caustics in the equal-strength binary, intermediate separation. . .	30
2.4	Critical curves and caustics in the equal-strength binary, close-intermediate transition. Dashed magenta circle indicates the pseudocaustic for $m = 0$	30
2.5	Critical curves and caustics in the equal-strength binary, close separation. Dashed magenta circle indicates the pseudocaustic for $m = 0$	31
2.6	The elliptic umbilic catastrophe for $n = 2$, $m = 0.25$ and $0.714 \leq s \leq 0.834$ in steps of 0.02, one colour for each s from red to blue. The separation at which the catastrophe occurs is $s_{euc} = 0.774$. Critical curves on the left side panel, caustics on the right side panel.	33
2.7	Critical curves and caustics in the unequal-strength binary, wide separation. Here and in the following figures the lens on the left has $n = 1$ and the lens on the right has variable m	34
2.8	Critical curves and caustics in the unequal-strength binary, intermediate-wide transition.	35
2.9	Critical curves and caustics in the unequal-strength binary, intermediate separation. .	35

2.10	Critical curves and caustics in the unequal-strength binary, close-intermediate transition. Dashed magenta circle indicates the pseudocaustic for $m = 0$	36
2.11	Critical curves and caustics in the unequal-strength binary, close separation. The dashed magenta circle indicates the pseudocaustic for $m = 0$	37
2.12	Critical curves and caustics in the unequal-strength binary with the standard lens on the right, wide separation. Here and in the following figures the lens on the right has $m = 1$ and the lens on the left has variable n	38
2.13	Critical curves and caustics in the unequal-strength binary with the standard lens on the right, intermediate-wide transition.	38
2.14	Critical curves and caustics in the unequal-strength binary with the standard lens on the right, intermediate separation.	39
2.15	Critical curves and caustics in the unequal-strength binary with the standard lens on the right, close-intermediate transition.	39
2.16	Critical curves and caustics in the unequal-strength binary with the standard lens on the right, close separation.	40
2.17	Critical values of the separation for the intermediate-wide transition s_{IW} as a function of γ (upper curves); critical values of the separation for the close-intermediate transition s_{CI} as a function of γ (lower curves). The upper panel is for $n = 1$ and variable m ; the lower panel is for $m = 1$ and variable n	42
2.18	Upper panel: size of the caustic in the wide case for $s = 4$, $\gamma = 0.01$, for three different fixed $n = 0.5, 1, 2$, with variable m . Lower panel: size of the caustic in the close case for $s = 0.6$, $\gamma = 0.01$, for three different fixed $n = 0.5, 1, 2$, with variable m	47
3.1	The four UTs and the four ATs. Source: eso.org.	53
3.2	Diagram of GRAVITY subsystems. Source: Gravity Collaboration et al.[110].	54
3.3	On the left: S2, S38 and S55 orbit reconstruction around Sgr A*; on the right: orbit reconstruction of other S-stars.	58
3.4	Projection on the sky of the real star's orbit onto the plane of the sky, the osculating orbital parameters are shown.	60
3.5	The angle γ_0 as a function of the source position r_S in a semi-log scale.	61
3.6	Analysis for S2. First row: $\gamma(t)$ (top left) and $r(t)$ (top right) as functions of time; second row: right ascension (on the left) and declination (on the right); last row: astrometric shifts in right ascension (left) and declination (on the right). Computations are done starting from T_0 over two periods.	64

3.7	Analysis for S38. First row: $\gamma(t)$ (top left) and $r(t)$ (top right) as functions of time; second row: right ascension (on the left) and declination (on the right); last row: astrometric shifts in right ascension (left) and declination (on the right). Computations are done starting from T_0 over two periods.	65
3.8	Analysis for S55. First row: $\gamma(t)$ (top left) and $r(t)$ (top right) as functions of time; second row: right ascension (on the left) and declination (on the right); last row: astrometric shifts in right ascension (left) and declination (on the right). Computations are done starting from T_0 over two periods.	66
3.9	S2 orbit with its original fixed inclination $i = 134.7^\circ$ by varying its semimajor axis from $a \times 10^{-0.25}$ (first row, top left) to $a \times 10^{-1.5}$ (second row, bottom right). The red line stands for the unperturbed orbit, which is almost completely hidden behind the green line standing for the orbit affected by gravitational lensing. The circle stands for the position of Sgr A*. The orbit is traced over two periods starting from T_0 and it does not close due to the relativistic precession.	69
3.10	S2 orbit with a fixed reduced semimajor axis by a factor of $10^{-1.5}$ by varying its inclination from $i = 90.5^\circ$ (left top) to $i = 130^\circ$ (right bottom) in steps of 5° . The red line stands for the unperturbed orbit, the green line stands for the orbit affected by gravitational lensing. The circle stands for the position of Sgr A*. The orbit is traced over two periods starting from T_0 and it does not close due to the relativistic precession.	70
3.11	The δ obtained by varying the semimajor axis a and the inclination i . From top left to the sixth panel: δ_a/a , δ_e , δ_i , δ_ω , δ_Ω , δ_P/P as a function of $\log a$ expressed in au. The error bars on the right indicate GRAVITY's fit error, see Table 3.1.	72
3.12	The χ^2 test of all data sets vs $\log a$ expressed in au.	73

LIST OF TABLES

3.1	S2, S38 and S35 osculating orbital parameters from Gravity Collaboration's fit [111, 127].	55
3.2	The black hole mass and the derived distance of the Solar System to the Galactic Center. [111, 127].	55
3.3	Comparison between the systematic error δ committed by ignoring gravitational lensing and the statistical uncertainty σ reported by the GRAVITY Collaboration [111, 127] for S2, S38 and S55.	67

CHAPTER 1

INTRODUCTION

1.1 History of Gravitational Lensing

Historically scientists started studying the bending of light with Newton in 1704 with the treatise *Opticks*. In 1784, Henry Cavendish calculated the bending of light due to Newtonian gravity, without publishing the result and its proof was brought to surface only in the 1900s. In 1801 Johann von Soldner calculated the bending of light as it passes close to a massive object, by using Newton's theory of light as a stream of massive corpuscles (photons) but neglecting their mass in the calculation, and he found out that the deflection angle is $2GM/(c^2u)$ where G is Newton's gravitational constant, c is the speed of light, M is the mass of the massive object and u is the impact parameter. This solution was very close to Cavendish's. In 1802, Thomas Young's interference experiment showed that light must behave as a wave. Scientists then focused on wave optics, forgetting about the interaction of light with gravity.

If we consider a ray of light passing close to a massive object of mass M , the deflection angle is given by

$$\hat{\alpha} = \frac{4GM}{c^2u} \quad (1.1)$$

as shown in Fig. 1.1.

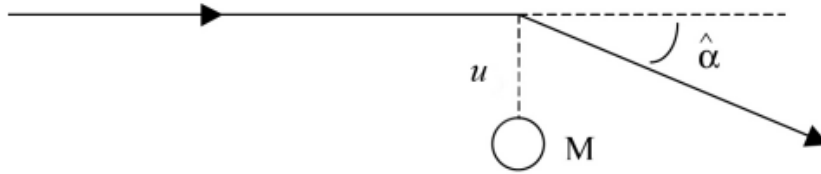


Figure 1.1: Deflection of light by a massive compact object, credits: Chiara Melchiorre.

Einstein deduced the bending of light in 1913, two years before his theory was completed [1], and the British astronomer Arthur Eddington decided to exploit this intuition experimentally. On May 29th 1919 during a solar eclipse in Principe Islands he showed that stars moved from their position by the amount precisely predicted by general relativity. This great result was put in evidence by the main newspapers of that time, such as *Cosmic Time* that titled "Sun's gravity bends starlight", see Fig. 1.2, underlining the triumph of Einstein's theory. This was the first observation of *gravitational lensing* [2].



Figure 1.2: The 1919 Edition of Cosmic Times. Image Credit: NASA.

1.2 The Lens Equation

The Einstein's field equations are [3]:

$$G^{\alpha\beta} = \frac{8\pi G}{c^4} T^{\alpha\beta} \quad (1.2)$$

where $T^{\alpha\beta}$ is the *stress-energy tensor* and $G^{\alpha\beta}$ is the *Einstein tensor*. In the Newtonian limit, these equations reduce to the Poisson's equation

$$\nabla^2 \varphi = 4\pi G \rho \quad (1.3)$$

where φ is the Newtonian potential, ρ is the matter density and ∇^2 is the Laplace operator. The stress-energy tensor satisfies the conservation law $T^{\alpha\beta}{}_{;\beta} = 0$, so $G^{\alpha\beta}{}_{;\beta} = 0$.

The Schwarzschild metric which describes the external gravitational field of a non rotating spherically symmetric body is

$$ds^2 = \left(1 - \frac{2GM}{rc^2}\right) c^2 dt^2 - \left(1 - \frac{2GM}{rc^2}\right)^{-1} dr^2 - r^2 d\theta^2 - r^2 \sin^2 \theta d\phi^2 \quad (1.4)$$

where θ and ϕ are the polar coordinates, t is the coordinate time and r is the radial coordinate. This metric is a first approximation for any kind of gravitational lens and we refer to a point-lens because we do not have any information about the physical size of the body generating the field as long as light rays pass outside the mass distribution.

The Lagrangian of a free particle in the gravitational field is [3]

$$\mathcal{L} = \frac{1}{2} g_{\alpha\beta} \dot{x}^\alpha \dot{x}^\beta \quad (1.5)$$

where $g_{\alpha\beta}$ is the metric tensor, \dot{x}^α and \dot{x}^β are the four-velocities and the action is given by

$$S = \int \mathcal{L}(x^\alpha, \dot{x}^\alpha) d\lambda \quad (1.6)$$

with λ the affine parameter which satisfies $\lambda = \frac{\tau}{m}$ for a massive particle m and being τ the proper time. By varying the action with respect to the coordinates, and by setting the variation equal to zero we obtain the Euler-Lagrange equations:

$$\frac{d}{d\lambda} \left(\frac{\partial \mathcal{L}}{\partial \dot{x}^\alpha} \right) - \frac{\partial \mathcal{L}}{\partial x^\alpha} = 0 \quad (1.7)$$

with $x^\alpha = (t, r, \theta, \phi)$.

The particle moves along a geodesic in the spacetime and the geodesic equations come from the Lagrangian in the Schwarzschild metric [3]

$$\mathcal{L} = \frac{1}{2} \left[\left(1 - \frac{2GM}{rc^2}\right) c^2 \dot{t}^2 - \left(1 - \frac{2GM}{rc^2}\right)^{-1} \dot{r}^2 - r^2 \dot{\theta}^2 - r^2 \sin^2 \theta \dot{\phi}^2 \right] \quad (1.8)$$

1. Introduction

where the dot derivatives stand for $\frac{d}{d\lambda}$. We get from Eq.(1.8) the equations for \dot{t} , $\dot{\phi}$ and $\dot{\theta}$

$$\frac{d}{d\lambda} \left[\left(1 - \frac{2GM}{rc^2} \right) \dot{t} \right] = 0. \quad (1.9)$$

From this last one we find

$$\dot{t} = \frac{E}{c^2 \left(1 - \frac{2GM}{rc^2} \right)}. \quad (1.10)$$

where E is the particle energy per unit mass. At the same way, from Eq.(1.8), we get

$$\frac{d}{d\lambda} (r^2 \sin^2 \theta \dot{\phi}) = 0 \quad (1.11)$$

and from this one we find

$$\dot{\phi} = \frac{L}{r^2 \sin^2 \theta}. \quad (1.12)$$

where L is the particle angular momentum per unit mass. For $\dot{\theta}$ we get

$$\frac{d}{d\lambda} (r^2 \dot{\theta}) = r^2 \sin \theta \cos \theta \dot{\phi}^2. \quad (1.13)$$

The initial conditions are

$$\begin{cases} \theta = \frac{\pi}{2} \\ \dot{\theta} = 0 \end{cases} \quad (1.14)$$

if we let the particle move on the equatorial plane and these conditions identify a unique solution and θ will be $\frac{\pi}{2}$ for all λ : the particle will remain in the equatorial plane. In general relativity orbits are planar as in the Newtonian case. With $\theta = \frac{\pi}{2}$ we get

$$\dot{\phi} = \frac{L}{r^2}. \quad (1.15)$$

L and E are constants of motion which correspond to the ignorable coordinates ϕ and t in Eq.(1.8).

To get \dot{r} we use the condition

$$g_{\alpha\beta} \dot{x}^\alpha \dot{x}^\beta = 1 \quad (1.16)$$

and, for a massless particle (i.e. a photon, when $m = 0$), we get

$$\dot{r} = \pm \sqrt{\frac{E^2}{c^2} - \left(1 - \frac{2GM}{c^2 r} \right) \left(1 + \frac{L^2}{r^2} \right)} \quad (1.17)$$

where the negative solution is for the photon approaching the lens, the positive solution is for the photon moving away from the lens.

The deflection angle $\hat{\alpha}$ is the angle between the incoming trajectory of the photon and the outgoing one. If the photon comes from the direction at azimuth ϕ_i and approaches the origin at a

minimum radial coordinate r_0 when $\lambda = 0$ and then escapes in the direction ϕ_f , the deflection angle is

$$\begin{aligned}\hat{\alpha} &= \phi_f - \phi_i - \pi = -\pi + \int_{\phi_i}^{\phi_f} d\phi = \\ &= -\pi + \int_{-\infty}^0 \frac{d\phi}{d\lambda} d\lambda + \int_0^{+\infty} \frac{d\phi}{d\lambda} d\lambda = \\ &= -\pi + \int_{+\infty}^{r_0} \frac{d\phi}{d\lambda} \frac{d\lambda}{dr} dr + \int_{r_0}^{+\infty} \frac{d\phi}{d\lambda} \frac{d\lambda}{dr} dr\end{aligned}\tag{1.18}$$

By replacing Eq. (1.15) and Eq. (1.17) in Eq. (1.18), by taking care of the correct signs in the approach and escape integrals respectively and by swapping the extrema of the approach integral, we obtain

$$\hat{\alpha} = -\pi + 2 \int_{r_0}^{+\infty} \frac{dr}{r \sqrt{\frac{r^2}{r_0^2} \left(1 - \frac{2GM}{c^2 r_0}\right) - \left(1 - \frac{2GM}{c^2 r}\right)}}\tag{1.19}$$

where r_0 is the closest approach distance of the null geodesic on which the photon is travelling. It is related to the impact parameter u of the asymptotic trajectory at infinity as

$$u = \frac{r_0}{\sqrt{1 - \frac{2GM}{c^2 r_0}}}\tag{1.20}$$

Eq.(1.19) is an elliptic integral but for the majority of physically interesting cases, we can make an expansion for weak fields, and at first order in M we get the deflection angle as in Eq. (1.1).

In gravitational lensing we have two regimes, strong and weak lensing, depending on the alignment of the lens and source as illustrated in Fig. 1.3.

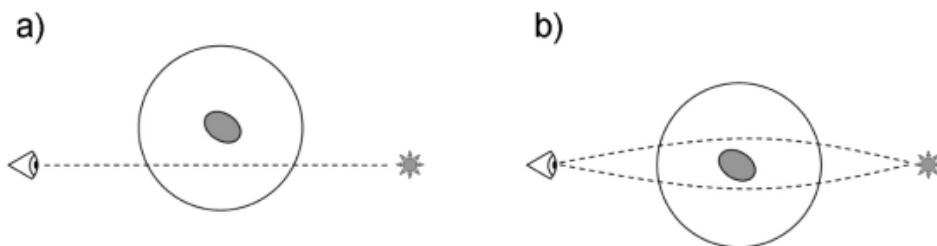


Figure 1.3: Figure a): Weak lensing; Figure b): Strong lensing. Credits: Chiara Melchiorre.

We have weak lensing when the lens is far from the line of sight to the source and we have small magnifications, mild distortions of the images while we have strong lensing when the line of sight from the observer to source is very close to the lens, in this case we have high magnifications, strong distortions, multiple images, arcs and rings in the lens plane.

The gravitational lens configuration scheme is shown in Fig. 1.4

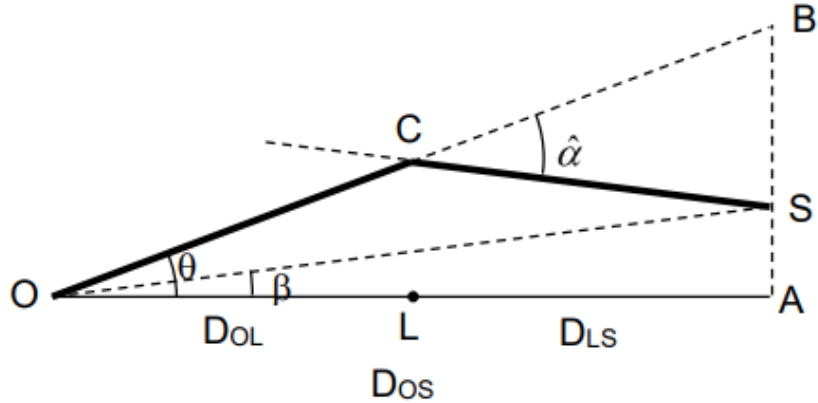


Figure 1.4: Gravitational lens scheme. Credits: Valerio Bozza.

and the lens equation is given by the geometric relation between the source position and the position of the images for a given distribution of mass acting as lens. If we consider a point-lens (i.e. a lens with no physical size of the body generating the field), an observer O and a source S , we call optical axis the line OL , the photons move on the plane defined by O , L (the lens) and S and, by approximating all tangents with their arguments, from the relation $AS = AB - BS$ we get the relation $D_{OS}\beta = D_{OS}\theta - D_{LS}\hat{\alpha}$ and the lens equation becomes [4]

$$\beta = \theta - \frac{D_{LS}}{D_{OS}}\hat{\alpha} \quad (1.21)$$

where D_{LS} is the distance between the lens and the source, D_{OS} is the distance between the observer and the source, D_{OL} is the distance between the observer and the lens, β is the source position, θ is the angle where the observer sees the image and $\hat{\alpha}$ is the deflection angle as given in Eq.(1.1). If we rewrite Eq.(1.1) as $\hat{\alpha} = \frac{4GM}{D_{OL}\theta}$, the lens equation becomes

$$\beta = \theta - \frac{\theta_E^2}{\theta} \quad (1.22)$$

where

$$\theta_E = \sqrt{\frac{4GM}{c^2} \frac{D_{LS}}{D_{OL}D_{OS}}} \quad (1.23)$$

is the Einstein angle. If we solve Eq. (1.22) for a generic source β we find the images position

$$\theta_{\pm} = \frac{\beta \pm \sqrt{\beta^2 + 4\theta_E^2}}{2} \quad (1.24)$$

where θ_+ is the image on the same side of the source and θ_- the one on the other side. For $\theta \gg \theta_E$ we have $\theta_+ \rightarrow \beta$ and $\theta_- \rightarrow 0$; for $\theta \ll \theta_E$ we have $\theta_{\pm} \rightarrow \pm\theta_E$, i.e. the two images form at the same angular distance from the lens and merge together to form a continuous ring (the Einstein ring).

If an extended object acts as a lens we can rewrite the lens equation in a vectorial form. As the extension of the lens in the direction of the optical axis is usually much smaller than the distances between observer and lens and between lens and source, we can assume the lens as a thin lens in comparison with the whole light path. We replace the mass distribution of the lens with the projected surface mass distribution on the lens plane. We define the surface mass density as [4]

$$\Sigma(\vec{\xi}) = \int dz \rho(\vec{\xi}, z) \quad (1.25)$$

which corresponds to the projection of the mass distribution ρ on a plane passing through its center and orthogonal to the light ray direction where $\vec{\xi}$ is the two dimensional vector indicating the positions in the lens plane and z is the coordinate in the orthogonal direction. The gravitational effect of the lens can be calculated by integrating over the surface elements $d^2\xi$, with the surface mass density Σ in the lens plane using Eq. (1.1), so we can rewrite the deflection angle at a position $\vec{\xi}$ as

$$\vec{\alpha}(\vec{\xi}) = \frac{4G}{c^2} \int \frac{(\vec{\xi} - \vec{\xi}') \Sigma(\vec{\xi}')}{|\vec{\xi} - \vec{\xi}'|} d^2\xi' \quad (1.26)$$

The plane parallel to the lens plane at the distance of the source from the observer is called the source plane and for small angles we have the relation $\vec{\beta} D_{OS} = \vec{\theta} D_{OS} - \vec{\alpha} D_{LS}$ where $\vec{\theta} = \vec{\xi} / D_{OL}$ and $\vec{\alpha} = \frac{D_{LS}}{D_{OS}} \vec{\alpha}'$, so we rewrite the lens equation as

$$\vec{\beta} = \vec{\theta} - \vec{\alpha}. \quad (1.27)$$

The rescaled projected gravitational potential is given by

$$\Psi \equiv \frac{2}{c^2} \frac{D_{LS}}{D_{OS} D_{OL}} \psi \quad (1.28)$$

where

$$\psi(\vec{\xi}) = 2G \int d^2\xi' \Sigma(\vec{\xi}') \ln |\vec{\xi} - \vec{\xi}'| \quad (1.29)$$

is the projected potential and by the use of Eq. (1.26) we get

$$\vec{\alpha}' = \frac{2}{c^2} \vec{\nabla}_{\xi} \psi(\vec{\xi}) \quad (1.30)$$

and then we obtain the following relation

$$\vec{\alpha} = \vec{\nabla}_{\theta} \Psi \quad (1.31)$$

and finally the lens equation becomes

$$\vec{\beta} = \vec{\theta} - \nabla_{\theta} \Psi(\vec{\theta}). \quad (1.32)$$

which is a non-linear equation in $\vec{\theta}$ which means that for some source positions $\vec{\beta}$ we could have multiple solutions of the lens equations instead of one. When we have the formation of multiple images we are in the strong lensing regime.

1.3 Magnification

The gravitational lensing brings to the deformation and to the shift of the images and it affects the flux of the sources which experiences the lensing but it also preserves surface brightness and this is due to Liouville's theorem.

The surface brightness is given by

$$I(\nu) = \frac{dE}{dt dA d\Omega d\nu} \quad (1.33)$$

and it is defined as the flux of energy E of a certain frequency ν , crossing a unit area A perpendicular to the direction of propagation, per unit time, per unit solid angle Ω and per unit frequency interval.

The flux received from a source is the product of its surface brightness and the solid angle it subtends. The deflection of light changes the shape and the solid angle that the source subtends on the sky, this leads to a magnification of the source luminosity by the gravitational lensing which is given by [4]

$$\mu = \frac{d\Omega}{d\Omega_0} \quad (1.34)$$

where $d\Omega$ is the observed solid angle and $d\Omega_0$ is the corresponding solid angle in the absence of lensing.

Generally it is not possible to measure the flux from the source and so it is not possible to know the magnification but it is possible to measure the variation of the total flux of the images. If we consider an extended lensing mass distribution with no axis of symmetry, the lens equation written in Eq. (1.27) can be seen as a two-dimensional mapping between the positions of the images $\vec{\theta}$ and the actual source positions in the sky $\vec{\beta}$. We define the Jacobian of the lens mapping by

$$J = \det \frac{\partial \vec{\beta}}{\partial \vec{\theta}} \quad (1.35)$$

and the relation

$$d\Omega = J^{-1} d\Omega_0 \quad (1.36)$$

relates the differential element of solid angle in the image plane $d\Omega = d\vec{\theta}_1 \wedge d\vec{\theta}_2$ with the corresponding element of solid angle in the source plane $d\Omega_0 = d\vec{\beta}_1 \wedge d\vec{\beta}_2$. The magnification is given by

$$\mu = J^{-1}. \quad (1.37)$$

Starting from Eq.(1.32) we can write the Jacobian as

$$J_{ij} \equiv \frac{\partial \beta_i}{\partial \theta_j} = \delta_{ij} - \frac{\partial^2 \Psi}{\partial \theta_i \partial \theta_j} \quad (1.38)$$

where δ_{ij} is the Kronecker delta and $\frac{\partial^2 \Psi}{\partial \theta_i \partial \theta_j}$ is the Hessian of the rescaled projected gravitational potential Ψ seen in Eq.(1.28).

The relation between the projected gravitational potential and the surface mass density distribution is given by the Poisson equation

$$\nabla_{\xi}^2 \psi(\vec{\xi}) = 4\pi G \Sigma(\vec{\xi}) \quad (1.39)$$

and the trace of the Hessian of the rescaled projected gravitational potential is

$$Tr\left(\frac{\partial^2 \Psi}{\partial \theta_i \partial \theta_j}\right) = \nabla_{\xi}^2 \psi = 2 \frac{\Sigma(\vec{\theta})}{\Sigma_{crit}} \equiv 2\kappa(\vec{\theta}) \quad (1.40)$$

where

$$\Sigma_{crit} = \frac{c^2}{4\pi G} \frac{D_{OS}}{D_{OL} D_{LS}} \quad (1.41)$$

is the critical surface density and

$$\kappa(\vec{\theta}) \equiv \frac{\Sigma(\vec{\theta})}{\Sigma_{crit}} \quad (1.42)$$

is the convergence which is a parameter that changes the size of the image of a source without modifying its shape. Now we can rewrite the mapping matrix as

$$\mathcal{T} = \begin{pmatrix} 1 - \kappa - \gamma_1 & -\gamma_2 \\ -\gamma_2 & 1 - \kappa + \gamma_1 \end{pmatrix} \quad (1.43)$$

where

$$\gamma_1 = \frac{1}{2} \left(\frac{\partial^2 \Psi}{\partial \theta_1^2} - \frac{\partial^2 \Psi}{\partial \theta_2^2} \right) \quad (1.44)$$

$$\gamma_2 = \left(\frac{\partial^2 \Psi}{\partial \theta_1 \partial \theta_2} = \frac{\partial^2 \Psi}{\partial \theta_2 \partial \theta_1} \right) \quad (1.45)$$

and the combination of γ_1 and γ_2 is the shear

$$\gamma = \sqrt{\gamma_1^2 + \gamma_2^2} \quad (1.46)$$

which is a parameter responsible for the distortions in the image shape.

If we calculate the trace and the determinant of \mathcal{T}

$$Tr\mathcal{T} = 2(1 - \kappa) \quad (1.47)$$

$$det\mathcal{T} = (1 - \kappa)^2 - \gamma^2 \quad (1.48)$$

from which we can get the eigenvalues of the mapping matrix: $1 - \kappa \pm \gamma$ which say that the image is stretched by a factor $1 - \kappa - \gamma$ in one direction and by a factor $1 - \kappa + \gamma$ in the other direction. If one eigenvalue has a negative value (negative partial parity), the image is inverted in that direction, if both eigenvalues are negative, the total parity of the image is positive and it appears rotated by 180° , if one eigenvalue has a positive value it has positive partial parity and if both images have positive eigenvalues the magnification is greater than one.

A sufficient, but not necessary condition to have the formation of multiple images is given by

$$\Sigma(\vec{\theta}) > \Sigma_{crit} \quad (1.49)$$

which means $\kappa(\vec{\theta}) > 1$, but is also sufficient to have $\kappa > 1 - \gamma$.

For a circularly symmetric system the radial magnification is given by

$$\mu_r = \left(\frac{\partial\beta}{\partial\theta} \right)^{-1} \quad (1.50)$$

while the tangential magnification is given by

$$\mu_t = \frac{\theta}{\beta} \quad (1.51)$$

and the total magnification is

$$\mu = \mu_r \mu_t. \quad (1.52)$$

1.4 Critical Curves and Caustics

The sign of the Jacobian determinant defines the regions where we can find the images. The critical points on the lens plane where the Jacobian is equal to zero are the critical points of the lens map. The corresponding points on the source plane, found by applying the lens map on the critical

points are the caustic points. When the source crosses a caustic, a degenerate image is formed on the corresponding critical point and therefore creation or destruction of images can happen. After the crossing, all images are again ordinary, but according to the theorem on the number of images, it must always change by two units.

A critical point is a singularity in the lens map which means that it is not possible to invert the map in that point. $J = 0$ is the condition which defines a critical point and where one eigenvalue vanishes (i.e., $\text{Tr}J \neq 0$ and $\vec{\nabla}J \neq 0$): these points are the *cusps*. If we define a tangent vector \vec{T} to the critical curve in the critical point, $J\vec{T}$ is tangent to the corresponding caustic. We can distinguish two cases:

- **fold**: when a critical point is a cuspid with $J\vec{T} \neq 0$;
- **cusp**: when a critical point is a cuspid with $J\vec{T} = 0$ and $(\vec{T} \cdot \vec{\nabla})J\vec{T} \neq 0$;

folds and cusps are the only stable singularities.

About the unstable singularities it is necessary to use the Hessian of the Jacobian determinant Δ , so we can distinguish:

- **umbilics**: when $J = 0$, $\text{Tr}J = 0$ and $\vec{\nabla}J = 0$, which are divided in
 - *elliptic umbilics* when $\det\Delta J > 0$, the eigenvalues are both negative and the corresponding critical curve is a single point which, for small variations of the parameters, opens up in a circular critical curve, while the corresponding caustic is triangular with three cusps;
 - *hyperbolic umbilics* when $\det\Delta J < 0$ which are single points joining a fold to a cusp of another critical curve. For small variations the cusp is exchanged between the two critical curves.
- **cusps of higher order**: they are divided in
 - *swallowtail* or second order cuspid with $(\vec{T} \cdot \vec{\nabla})J\vec{T} = 0$;
 - *butterfly* or third order cuspid which merges three cusps leaving only one;
- **gradient singularities**: we have them when J has a non-vanishing eigenvalue and zero gradient. A gradient singularity is a maximum, minimum or saddle point of J . We can distinguish two cases:
 - $\det\Delta J > 0$, in this case it is a maximum or a minimum. When it touches the plane $J = 0$ a new critical curve forms and its caustic has two opposed cusps, with the shape of a mouth, they are called *lips*;

- $\det\Delta J < 0$, in this case we have a saddle. When it is cut by the plane $J = 0$, we have four folds meeting in a cross. When the saddle is cut higher or lower we may have two separated folds or two folds with a cusp each. The two cusps point one against the other and they are called *beak-to-beak*.

1.5 The Binary Lens

If we consider a model with a lens composed by two point masses we are able to describe microlensing by binary stars or planetary systems. One of the advantages is that this lens model is sufficiently simple to be derived analytically. If we indicate the two point-like lenses' masses M_A and M_B in the lens plane forming angles $\vec{\theta}_A$ and $\vec{\theta}_B$ with the optical axes, the lens equation is

$$\vec{\beta} = \vec{\theta} - \mu_A(\vec{\theta} - \vec{\theta}_A)\frac{\theta_E^2}{|\vec{\theta} - \vec{\theta}_A|^2} - \mu_B(\vec{\theta} - \vec{\theta}_B)\frac{\theta_E^2}{|\vec{\theta} - \vec{\theta}_B|^2} \quad (1.53)$$

where $\mu_{A,B} = M_{A,B}/M$ are the reduced masses, $M = M_A + M_B$ is the total mass and θ_E is the one defined in Eq. (1.23) using M as total mass. With a binary lens we have the break of the axial symmetry of the system and the lens becomes astigmatic; the magnification pattern on the source plane also is different and we have the presence of extended caustics. When the source crosses a caustic new images are created or destroyed. According to the separation of the lenses s we can distinguish three topologies:

- wide binary topology;
- intermediate binary topology;
- close binary topology;

and each case corresponds to a specific shape of the caustics as we will show in some applications in the following chapters.

Now we introduce complex coordinates for the source [5]

$$\zeta = \beta_1 + i\beta_2 \quad (1.54)$$

and for the image

$$z = \theta_1 + i\theta_2 \quad (1.55)$$

and the lens equation becomes

$$\zeta = z - \frac{\mu_A}{(\bar{z} - \bar{z}_A)} - \frac{\mu_B}{(\bar{z} - \bar{z}_B)} \quad (1.56)$$

and the Jacobian determinant of the lens map in complex notation is given by

$$J(z, \bar{z}) = \left| \frac{\partial \zeta}{\partial z} \right|^2 - \left| \frac{\partial \zeta}{\partial \bar{z}} \right|^2 \quad (1.57)$$

and from Eq.(1.56) we have $\frac{\partial \zeta}{\partial z} = 1$ and

$$J = 1 - \left| \frac{\partial \zeta}{\partial \bar{z}} \right|^2 \quad (1.58)$$

with

$$\frac{\partial \zeta}{\partial \bar{z}} = \frac{\mu_A}{(\bar{z} - \bar{z}_A)^2} + \frac{\mu_B}{(\bar{z} - \bar{z}_B)^2}. \quad (1.59)$$

The condition $J = 0$ determines the critical curves on the lens plane and we can rewrite Eq.(1.58) as

$$\frac{\partial \zeta}{\partial \bar{z}} = e^{i\varphi} \quad (1.60)$$

with $0 < \varphi < 2\pi$.

By putting the origin of the coordinates at the midpoint between the two lenses and the real axis along the line joining the lenses and with the combination of the last two equations, we get a quartic equation for the points which define the critical lines: by applying the lens equation we get the caustics. The shape of the caustics depends on the mass ratio $\gamma = \mu_B/\mu_A$ and on the lens separation in units of the Einstein angle $s \equiv |z_A - z_B|$.

In order to understand the shape evolution of critical curves and caustics, we show the basic example of a standard binary lens in the Schwarzschild case. By standard binary lens we mean a system composed by two objects described by the same Schwarzschild metric and with the gravitational potential which goes as $1/r$. The starting critical curves configuration in Fig.1.5, first row left-top panel, is given by the close separation, then we move the lenses further to the intermediate and wide separations. On the second row we show the corresponding caustics. These results are for a mass ratio $\gamma = 1$.

1. Introduction

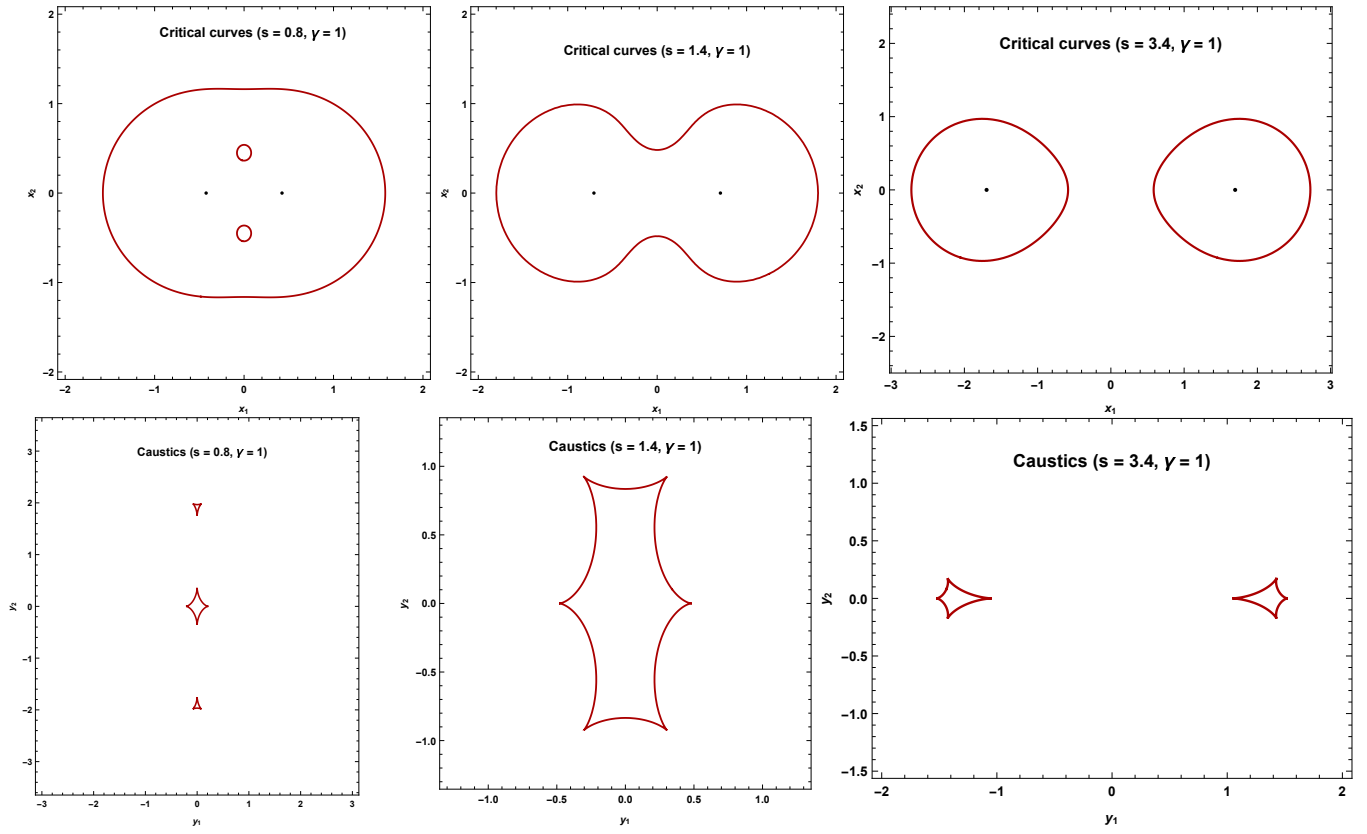


Figure 1.5: Critical curves and caustics for $\gamma = 1$ in the standard binary lenses.

In the next chapter we will study the generalization of caustics when we adopt $1/r^n$ potentials.

CHAPTER 2

GRAVITATIONAL LENSING BY OBJECTS WITH $1/r^n$ POTENTIAL

2.1 Motivations

Gravitational lensing is widely used in astrophysics and in cosmology to study compact objects (such as exoplanets, black holes and other stellar remnants [6, 7]), and extended objects (galaxies, clusters of galaxies and large-scale structures [8–12]) but it is also an important tool in the investigation of dark matter, dark energy and exotic matter (such as wormholes) [13–18].

Gravitational lensing effects by wormholes were investigated in Refs. [19, 20], with negative mass in Refs. [21–25] and with positive mass in Refs. [26–30]. We want to remark that in 1973, Ellis and Bronnikov independently found a massless wormhole (the Ellis wormhole) as a wormhole solution of the Einstein equations, see Refs. [31, 32]. Also spherically symmetric and static traversable Morris-Thorne wormholes were analyzed in Refs. [33, 34]. The most general extension of the Morris-Thorne wormhole is the solution of the stationary and axially symmetric rotating Teo wormhole in Ref. [35], the first rotating wormhole solution, and this was the starting point for the investigation of gravitational lensing by rotating wormholes explored by Jusufi and Ovgun in Ref. [36]. Tsukamoto and Harada studied the light rays passing through a wormhole in Ref. [37]; Ohgami and Sakai studied the images of wormholes surrounded by optically thin dust in Ref. [38] in order to state if it is possible to identify wormholes by observing shadows; this was also investigated in Ref. [39] in rotating dust flow.

The metric of the Ellis wormhole falls down asymptotically as $1/r^2$ and its deflection angle goes as the inverse square of the impact parameter $1/u^2$ as explored in Refs. [40–48]. Metrics falling

as $1/r^n$ were investigated also by Kitamura et al. [49] who found out that the deflection angle falls down with the same exponent as the metric: $\hat{\alpha} \sim 1/u^n$ with $n > 1$. Other investigations include Refs. [50–55]. Power-law deflection terms can also be found in gravitational lensing in the presence of plasma [56–60]. Particular attention was posed on the study of caustics of $1/r^n$ binary lenses by Bozza and Melchiorre in Ref. [61]

Particular attention was posed to the investigation of gravitational lensing by exotic lenses with a non-standard form of the equation of state or with a modified gravity theory by Asada [62]. A new method of detecting Ellis wormholes by the use of the images of wormholes surrounded by optically thin dust was investigated by Ohgami and Sakai [63].

After the Event Horizon Telescope (EHT) results [64], consisting in the detection of the shadow of a supermassive black hole in the center of galaxy M87, many authors tried to explore new frontiers, and an interesting new reference is from Tsukamoto and Kokubu [65]: they investigate the collision of two test particles in the Damour-Solodukhin wormhole spacetime where Damour and Solodukhin stated in Ref. [66] that is not possible to distinguish black holes from wormholes with observations on a limited timescale.

From the side of binary galaxies as binary lenses we must cite the considerable work of Shin and Evans [67] that discussed the critical curves and caustics in the case $n < 1$. This applies to generic galactic halos and isothermal sphere in particular, as the limit $n \rightarrow 0$.

Kovner investigated extremal solutions for a singular isothermal sphere with a tide (SIST) [68]; Evans and Wilkinson studied lens models for representing cusped galaxies and clusters, as isothermal cusps always generate a pseudocaustic [69], while Rhie discussed pseudocaustics of various lens equations [70]. Wang and Turner studied strong gravitational lensing by spiral galaxies, modelling them as infinitely thin uniform disks embedded in singular isothermal spheres [71], while Tessore and Metcalf investigated a general class of lenses following an elliptical power law profile [72]. All these systems possess pseudocaustics that were also investigated by Lake and Zheng in gravitational lensing by a ring-like structure [73]. Higher-order caustic singularities, such as the elliptic umbilic, were discussed by Aazami et al. [74].

In this chapter we want to extend the symmetric structure already studied by Bozza and Melchiorre in Ref. [61] for $1/r^n$ potentials, in which the two lenses have the same index n , to an asymmetric case in which the lenses have different indexes. This generalization is particularly useful in both scientific contexts described by $1/r^n$ potentials. In fact, we may have pairs of galaxies that have very different structures and thus different halo profiles, e.g. a dwarf galaxy as a satellite to a giant galaxy. On the other hand, if wormholes or other exotic objects exist, they might be part of a binary system with an ordinary star or other compact objects. The co-existence of objects with different $1/r^n$ potentials thus seems plausible in many situations, thus justifying the generalization

we are going to undertake here.

In Section 2.2 we describe exotic metrics, we give the lens equation for $1/r^n$ potentials for two exotic lenses with equal and different n . In Section 2.6 we study critical curves and caustics presenting three main cases: equal-strength binary lenses, unequal-strength binary and extreme unequal-strength binary lenses explaining the origin of the pseudocaustic and of the elliptic umbilic catastrophe for $mn < 1$. In Section 2.7 we study the transitions between different caustic topologies. In section 2.8 we derive analytical approximations for the three cases analysed in Section 2.6 in order to have a deeper understanding in the caustic evolution, in its shape and size. Finally in Section 2.9 we draw our discussion.

2.2 Exotic Metrics

The metric of non-Schwarzschild objects falls down asymptotically as $1/r^n$ giving rise to a deflection angle which goes as $1/u^n$ where u is the impact parameter of the ray of light which can be written also as $\alpha \sim 1/|\theta|^n$, where θ is the angular position at which the image is observed.

We consider the metric [49, 50, 61]

$$ds^2 = \left(1 - \frac{\alpha}{r^n}\right) c^2 dt^2 - \left(1 + \frac{\gamma}{r^n}\right) \left(dr^2 - r^2 d\theta^2 + \sin^2 \theta d\phi^2\right) \quad (2.1)$$

where α and γ are two coefficients related to the energy momentum tensor component as required by the Einsteins equations and the index n is either the exponent of the halo profile for a normal matter distribution or the ratio between tangential and radial pressure, $n = -2p_t/p_r$, if we consider exotic matter [55].

The deflection angle for a ray of light is given by [49, 50]

$$\hat{\alpha} = \frac{\sqrt{\pi} \Gamma[(1+n)/2] \alpha + \gamma}{\Gamma[n/2] u^n} \quad (2.2)$$

where $\Gamma[z]$ is the Euler gamma function.

The generalized deflection angle for a generic energy-momentum distribution is given by [75]

$$\hat{\alpha}(\vec{x}) = \frac{4G}{c^4} \int d^2x' \frac{\vec{x} - \vec{x}'}{|\vec{x} - \vec{x}'|^2} \int dz (\rho + p_z) \quad (2.3)$$

where $\hat{\alpha} \equiv \hat{\alpha}\vec{x}/u$ is the vectorial form of the deflection angle, z is referred to the z -axis travelled by the unperturbed photon, p_z is the z -component for the pressure and ρ is the energy density, so it is necessary to refer to a "strength ratio" between these two components in the case of binary lenses which will be deepened in the further sections.

The convergence is given by [49]

$$\kappa = \frac{1}{2} \nabla \cdot \hat{\alpha} \quad (2.4)$$

and by substituting Eq. (2.2) in Eq. (2.4) we get [55]

$$\kappa = \frac{\sqrt{\pi} \Gamma[(1+n)/2] (1-n)(\alpha + \gamma)}{\Gamma[n/2] u^{n+1}}. \quad (2.5)$$

The convergence is proportional to the mass density projected along the line of sight $\int \rho dz$ and, according to Ref. [49], both $n > 1$ and $(\alpha + \gamma) > 0$ (attractive deflection) imply a negative mass density and so we need exotic matter. A bond between convergence and energy-momentum tensor components is given by [55]

$$\kappa = \frac{\lambda_G}{2} \int dz (T_t^t - T_z^z) = \frac{\lambda_G}{2} \int dz \left[\rho + p_t + (p_r + p_t) \frac{z^2}{u^2 + z^2} \right] \quad (2.6)$$

where T_t^t and T_z^z are the non-zero components of the energy-momentum tensor for the energy density and the radial pressure respectively, $\lambda_G = 8\pi G/c^4$ is the gravitational coupling constant. In order to have a negative convergence in Eq. (2.6) we must have $\rho + p_z < 0$ in some regions which is a violation of the weak energy condition which is also a violation of strong energy condition as seen in Eq. (2.4).

2.3 The Lens Equation for Exotic Lenses

The lens equation for a single lens, first studied by Kitamura et. al in Ref. [49] and then generalized by Bozza and Postiglione in Ref. [55], is

$$\beta = \theta - \frac{\theta_E^{n+1}}{|\theta|^n} \text{Sign}(\theta), \quad (2.7)$$

where β is the source angular position with respect to the center of the lens, $\theta = u/D_L$ is the angular position at which the observer observes the image and

$$\theta_E = \left[\frac{D_{LS}}{D_{OL}^n D_{OS}} \frac{\sqrt{\pi} \Gamma[(1+n/2)] (\alpha + \gamma)}{\Gamma[n/2]} \right]^{\frac{1}{n+1}} \quad (2.8)$$

is the Einstein radius of the lens, which depends on D_{OL} , D_{OS} , D_{LS} .

From the lens equation we get two solutions θ_{\pm} : θ_+ is for the image which forms on the same side of the source, θ_- is the one on the other side. In the limit $\beta \gg \theta_E$ the primary image is in $\theta_+ \simeq \beta$ and the secondary image is in $\theta_- \simeq (-\theta_E^{n+1}/\beta)^{1/n}$. For $n > 0$ we have two real images; for $n = 0$ (the singular isothermal sphere) we have the secondary image only when the source is within the Einstein radius $\beta < \theta_E$. Due to the central singularity we have a single image from the crossing of the Einstein ring which violates the theorems on the number of images.

The radial magnification is given by Eq.(1.50)

$$\mu_r = \left(\frac{\partial\beta}{\partial\theta} \right)^{-1} = \left(1 + n \frac{\theta_E^{n+1}}{\theta^{n+1}} \right)^{-1} \quad (2.9)$$

while the tangential magnification is given by Eq.(1.51)

$$\mu_t = \frac{\theta}{\beta} = \left(1 - \frac{\theta_E^{n+1}}{\theta^{n+1}} \right)^{-1} \quad (2.10)$$

and the total magnification is the one found in Eq.(1.52).

In the case of $n > 1$ we can find some value of β giving the demagnifying effect (i.e. $\mu < 1$). We can expand μ around $\theta \simeq \beta \gg \theta_E$ and neglect the contribution of the secondary image

$$\mu \rightarrow 1 + (1 - n) \left(\frac{\theta_E}{\beta} \right)^{n+1} + (1 + n + n^2) \left(\frac{\theta_E}{\beta} \right)^{2n+2} + o \left(\frac{\theta_E}{\beta} \right)^{2n+2} \quad (2.11)$$

For $n > 1$ the first deviation from unity is negative. For the Schwarzschild case, the leading deviation is the second order going as β^{-4} : images created by exotic lenses are extended tangentially as the Schwarzschild ones, but are more compressed on the radial direction. The two deformations do not compensate at first order for exotic lenses. For $n < 1$ (ordinary matter) the situation is reversed, with a radial compression that is smaller than in the Schwarzschild case, allowing a higher total magnification emerging at the β^{-2} order.

2.4 The Standard Binary Lens Composed by Exotic Objects

The binary system composed by two exotic objects was already studied by Bozza and Melchiorre [61]. These symmetric binary lenses are mathematically simpler than the mixed case because the two deflection terms fall with the same power of the impact parameters, furthermore there is a strong astrophysical motivation in studying binary wormholes, exotic objects and $1/r^n$ potentials for their multiple applications already mentioned in Section 2.1 such as isothermal haloes with and without a regular core [67] (the singular isothermal sphere is the limiting case for $n \rightarrow 0$), lensing by two galaxies with spheroidal haloes declining as $1/r^{n+2}$. In general the two regimes of investigation of binary $1/r^n$ objects are for $n < 1$, corresponding to galactic haloes, and for $n > 1$, corresponding to exotic objects violating the energy conditions. For $n = 1$ we find the Schwarzschild metric which divides these two regimes. The light deflection is sensitive to the energy density and to the pressure so, in the binary lens case, it is necessary to refer to a "strength ratio" instead of a "mass ratio".

2.5 The Mixed Binary Lens

In this chapter we want to extend the symmetric structure already studied by Bozza and Melchiorre in Ref. [61] for $1/r^n$ potentials, in which the two lenses have the same index n , to an asymmetric case in which the lenses have different indexes. This generalization is particularly useful in both scientific contexts described by $1/r^n$ potentials. In fact, we may have pairs of galaxies that have very different structures and thus different halo profiles, e.g. a dwarf galaxy as a satellite to a giant galaxy. On the other hand, if wormholes or other exotic objects exist, they might be part of a binary system with an ordinary star or other compact objects. The co-existence of objects with different $1/r^n$ potentials thus seems plausible in many situations, thus justifying the generalization we are going to undertake here.

We give the lens equation for $1/r^n$ potentials for two exotic lenses with different n , we study critical curves and caustics presenting three main cases: equal-strength binary lenses, unequal-strength binary and extreme unequal-strength binary lenses explaining the origin of the pseudocaustic and of the elliptic umbilic catastrophe for $mn < 1$, then we study the transitions between different caustic topologies. Finally we derive analytical approximations for the three cases analysed in order to have a deeper understanding in the caustic evolution, in its shape and size.

We want to explore a system composed by two objects in the asymmetric case in which our lenses have different indexes, here indicated with n and m . The binary lens equation is

$$\vec{\beta} = \vec{\theta} - \theta_{E,A}^{n+1} \frac{\vec{\theta} - \vec{\theta}_A}{|\vec{\theta} - \vec{\theta}_A|^{n+1}} - \theta_{E,B}^{m+1} \frac{\vec{\theta} - \vec{\theta}_B}{|\vec{\theta} - \vec{\theta}_B|^{m+1}}, \quad (2.12)$$

where $\vec{\theta}_A$ and $\vec{\theta}_B$ are the coordinates of the two objects in the sky.

We note that the Einstein radii $\theta_{E,A}$ and $\theta_{E,B}$, appear with different exponents for each lens. It is thus convenient to use $\theta_{E,A}$ as a unit of measure for angles and define the "strength ratio" as $\gamma = \theta_{E,B}/\theta_{E,A}$. We rewrite the lens equation as follows

$$\vec{\beta} = \vec{\theta} - \frac{\vec{\theta} - \vec{\theta}_A}{|\vec{\theta} - \vec{\theta}_A|^{n+1}} - \gamma^{m+1} \frac{\vec{\theta} - \vec{\theta}_B}{|\vec{\theta} - \vec{\theta}_B|^{m+1}}. \quad (2.13)$$

Now we introduce complex coordinates [5] as seen in Eq.(1.54) and (1.55), we take the mid-point between the two lenses as the origin of the coordinates, and orient the real axis along the line joining the two lenses. We thus set $z_A = -s/2$ and $z_B = s/2$, where s is the normalized angular separation between the lenses. The lens equation becomes

$$\zeta = z - \frac{1}{\left(z + \frac{s}{2}\right)^{\frac{n-1}{2}} \left(\bar{z} + \frac{s}{2}\right)^{\frac{n+1}{2}}} - \frac{\gamma^{m+1}}{\left(z - \frac{s}{2}\right)^{\frac{m-1}{2}} \left(\bar{z} - \frac{s}{2}\right)^{\frac{m+1}{2}}} \quad (2.14)$$

The Jacobian determinant of the lens map in complex notation is given by

$$J(z, \bar{z}) = \left| \frac{\partial \zeta}{\partial z} \right|^2 - \left| \frac{\partial \zeta}{\partial \bar{z}} \right|^2, \quad (2.15)$$

which in our case becomes

$$J = \left[1 + \frac{1}{2} \left(\frac{n-1}{\left(z + \frac{s}{2}\right)^{\frac{n+1}{2}} \left(\bar{z} + \frac{s}{2}\right)^{\frac{n+1}{2}}} + \frac{\gamma^{m+1}(m-1)}{\left(z - \frac{s}{2}\right)^{\frac{m+1}{2}} \left(\bar{z} - \frac{s}{2}\right)^{\frac{m+1}{2}}} \right) \right]^2 - \frac{1}{4} \left| \frac{n+1}{\left(z + \frac{s}{2}\right)^{\frac{n+3}{2}} \left(\bar{z} + \frac{s}{2}\right)^{\frac{n-1}{2}}} + \frac{\gamma^{m+1}(m+1)}{\left(z - \frac{s}{2}\right)^{\frac{m+3}{2}} \left(\bar{z} - \frac{s}{2}\right)^{\frac{m-1}{2}}} \right|^2. \quad (2.16)$$

We note that the structure of the Jacobian becomes more complicated with respect to the ordinary point-lenses ($m = n = 1$), in which many terms disappear. We thus expect a correspondingly richer phenomenology. The Schwarzschild case was already explored by Schneider and Weiss in Ref. [76] for lenses with the same mass and by Erdl and Schneider for lenses with different masses [77]; Bozza and Melchiorre investigated the case $m = n$. In order to compare our results with theirs, it is important to note that there is no notion of a combined total Einstein radius when the two lenses have different indexes for their potentials. Therefore, the notation introduced there, with ϵ_i as the ratio of the individual lens strength to the total strength cannot be replicated here. Their results were expressed in terms of the ratio $q = \epsilon_B/\epsilon_A$. The relation between our parameter $\gamma = \theta_{E,B}/\theta_{E,A}$ and q is just $\gamma^{m+1} = q$. As a practical example, the Einstein radius scales as \sqrt{q} in the Schwarzschild case, where q becomes the mass ratio of the two lenses.

2.6 Critical curves and caustics for exotic lenses

The condition $J(z) = 0$ defines the critical curves on the lens plane. By applying the lens map on critical points we find the corresponding points on the source plane, which form the caustics. Critical curves and caustics are of fundamental importance to understand how gravitational lensing works. When a source crosses a caustic, a new pair of images is created on the corresponding point in the critical curve. Therefore, caustics bound regions with a different number of images. Critical curves distinguish regions in which images have opposite parities.

Our model contains four parameters: the indexes of the two potentials n , m , the separation between the two lenses s , and the ratio of the two Einstein radii γ . In order to start the exploration of this parameter space, we first analyze the equal-strength case with $\gamma = 1$, and then move to unequal strength cases.

In all plots presented in this chapter, we keep $n = 1$ fixed for the first lens (ordinary Schwarzschild lens), with variable m for the second lens: $m = 0, 0.5, 1, 2, 3$ (we remind that $m = 0$

is the singular isothermal sphere, already investigated by Shin and Evans in Ref. [67], galactic halos are in the range $0 < m < 1$ and $m = 2$ corresponds to the Ellis wormhole; objects with $m > 2$ require exotic matter).

Critical curves are obtained by the contour plot of the Jacobian determinant and these contours are then mapped through the lens equation in order to get the caustics. All computations are performed by *Wolfram Mathematica 11*¹.

2.6.1 Equal-strength binaries

In the equal-strength case, we set $\gamma = 1$, which means that $\theta_{E,A} = \theta_{E,B}$: both lenses would generate a critical curve with the same radius if they were isolated.

For the standard binary Schwarzschild lens [76], we know that three topologies exist:

- close separation, for $s < s_{CI}$;
- intermediate separation, for $s_{CI} < s < s_{IW}$;
- wide separation, for $s > s_{IW}$;

and the two transitions are $s_{CI} = 1$ and $s_{IW} = 2\sqrt{2}$ in our units.

We find that these three topologies persist for any values of n and m , although the boundary values may vary somewhat. In order to illustrate the evolution of critical curves and caustics in intelligible figures, we present the plots for different values of m at fixed values of separation s , starting from wide separation binaries and then moving the two lens closer.

First, in Fig. 2.1, we have two lenses at wide separations for $s = 3.4$. Here we clearly see how the Einstein ring of each lens is distorted by the presence of the partner lens. Comparing the critical curves obtained at different values of the index m , we clearly see that the distortion is stronger for small values of m . This is a direct consequence of the fact that the potential decays more steeply for larger m and thus the first lens feels a weaker tidal field from the second lens. This is particularly evident for the caustic of the first lens, which becomes very small at $m = 3$, while it becomes larger and more shifted at $m = 0$. The caustic of the second lens is almost independent of m . In practice, the shape and the size of the caustic is mostly determined by the tidal field of the first lens, which we are keeping fixed with $n = 1$.

¹<https://www.wolfram.com/mathematica/>

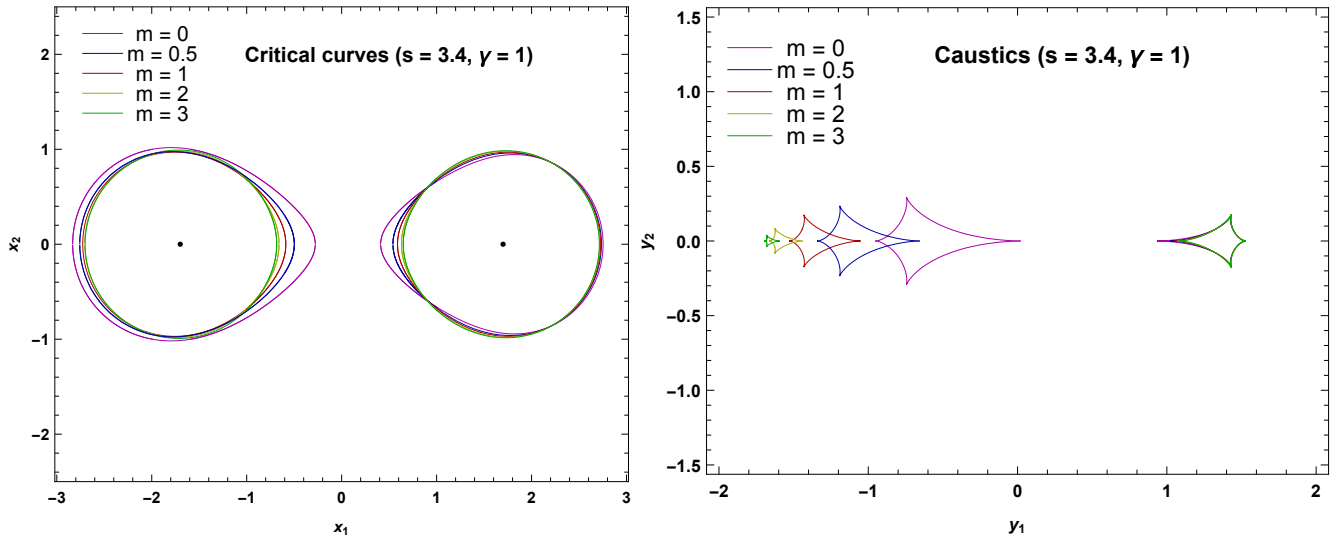


Figure 2.1: Critical curves and caustics in the equal-strength binary, wide separation. Here and in the following figures the lens on the left has $n = 1$ and the lens on the right has variable m .

In Fig. 2.2 we show critical curves and caustics for $s = 2\sqrt{2}$, which corresponds to the intermediate-wide transition in the standard $n = m = 1$ case. In fact, the red curves show the typical beak-to-beak singularity in the origin. For $m < 1$ we are already in the intermediate regime, while for $m > 1$ we are still in the wide regime. As explained before, the fact that the intermediate regime extends to larger separations for $m < 1$ is a consequence of the slower decay of the potential.

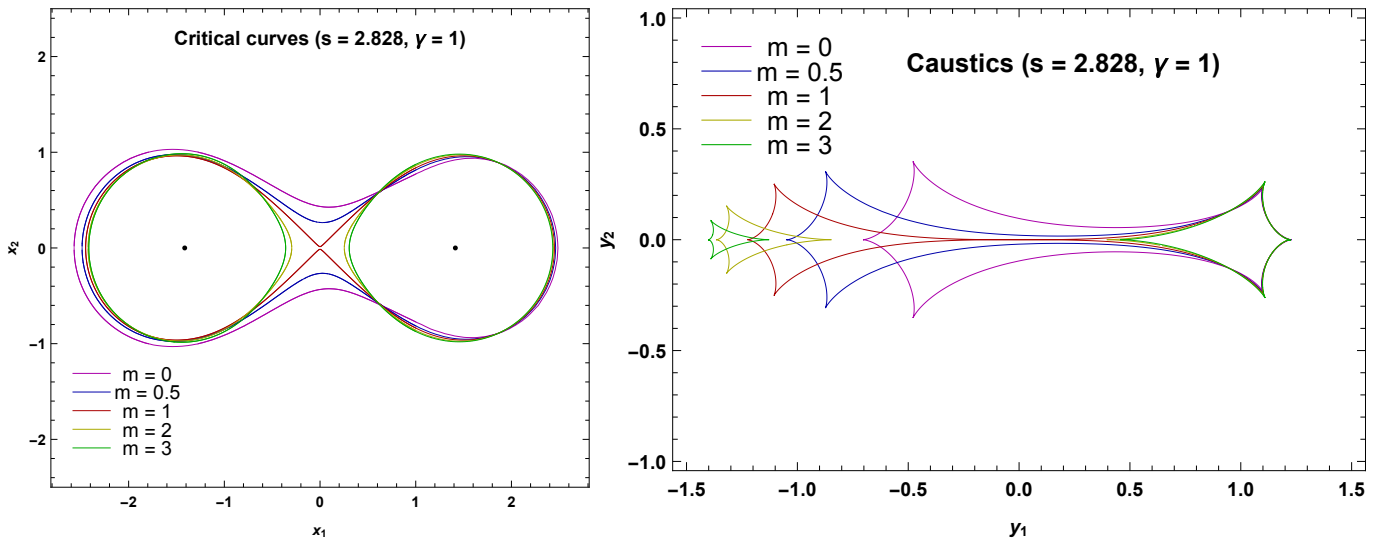


Figure 2.2: Critical curves and caustics in the equal-strength binary, intermediate-wide transition.

In Fig. 2.3 we see an intermediate separation at $s = 1.4$: critical curves are larger for smaller values of m , while caustics are larger for increasing m . Indeed, we are starting to see some kind of inversion in the behavior of the lenses. Steeper profiles are going to dominate at smaller separations, as will be more evident in the incoming figures.

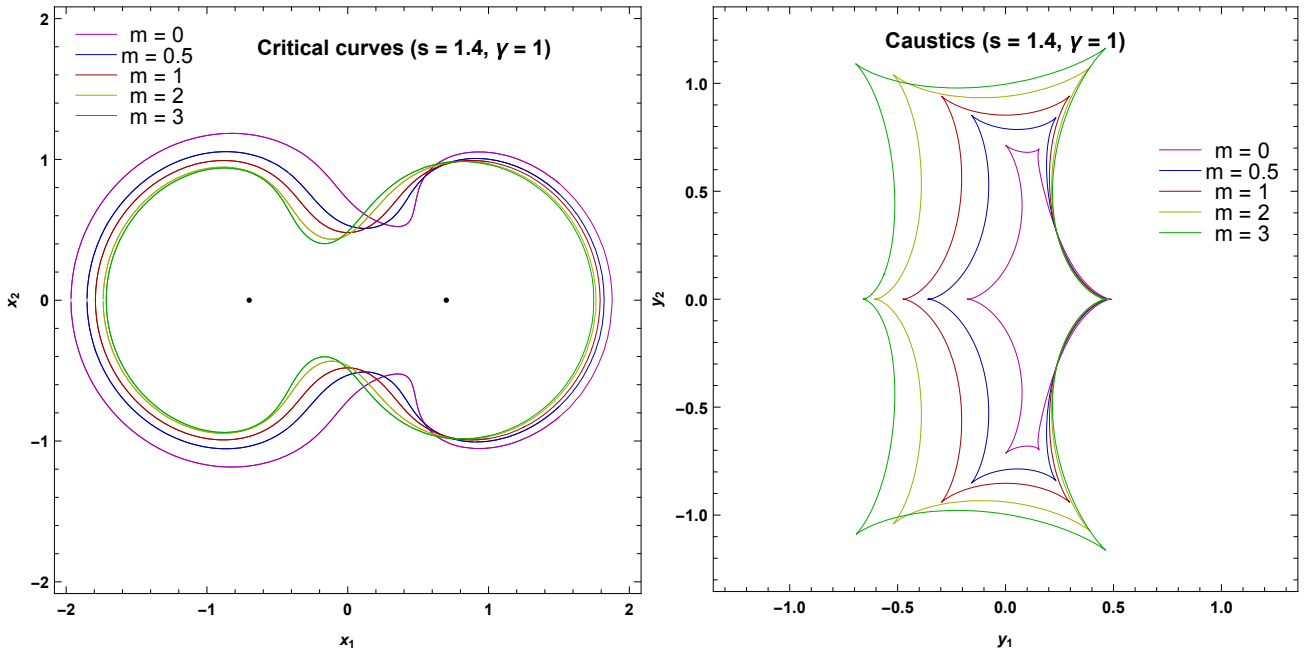


Figure 2.3: Critical curves and caustics in the equal-strength binary, intermediate separation.

In Fig. 2.4 we show the critical curves and caustics at $s = 1$, which corresponds to the close-intermediate transition for the standard $n = m = 1$ case. In fact, the red curve shows the two symmetric beak-to-beak singularities. Contrary to the previous transition, now the $m < 1$ caustics are already in the close regime, with small oval critical curves generating small triangular caustics. The $m > 1$ curves are still in the intermediate regime. Following the same reasoning, $m < 1$ lenses become subdominant in this regime and their influence on the whole system is smaller. In this regime, we also find the *elliptic umbilic catastrophe* that we shall discuss in Subsection 2.6.1.

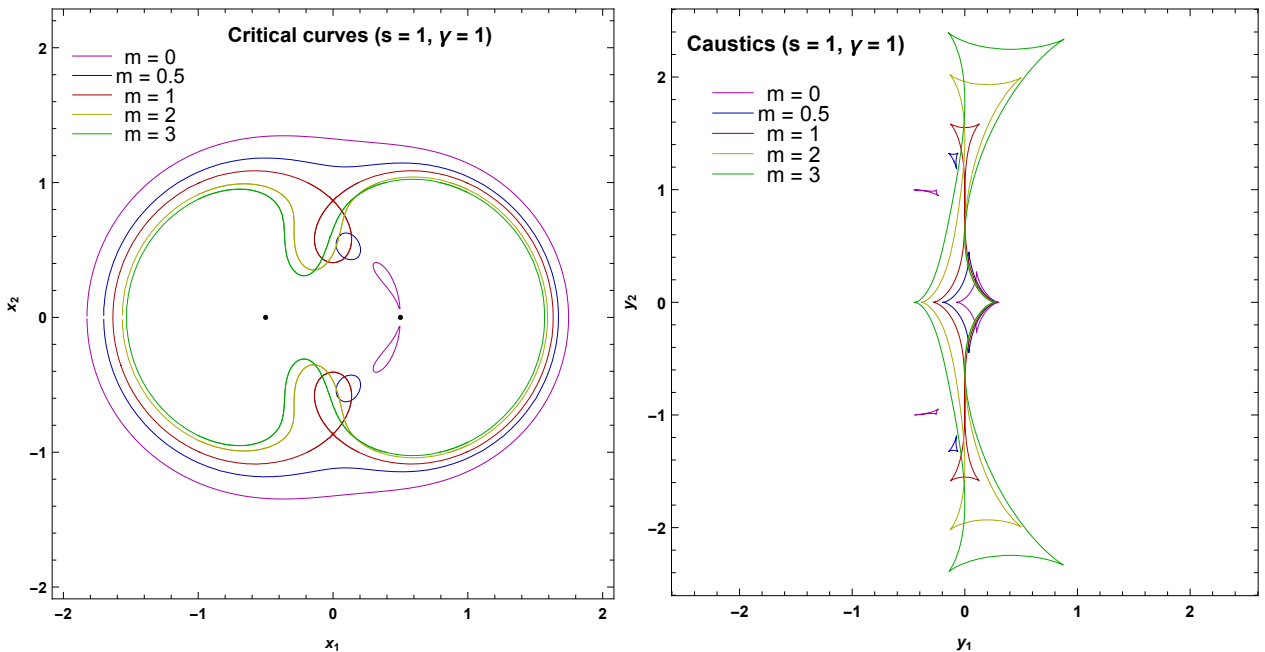


Figure 2.4: Critical curves and caustics in the equal-strength binary, close-intermediate transition. Dashed magenta circle indicates the pseudocaustic for $m = 0$.

In Fig.2.5 we can see critical curves and caustics in the close separation, for $s = 0.8$. Primary critical curves are big ovals that become smaller as m increases. In fact, $m > 1$ curves tend to be closer to an intermediate regime. Secondary critical curves are small ovals that move far from the second lens, in the left direction, for $m > 1$; for $m = 0$ (magenta line) they converge on the second lens with the shape of a lemniscate: in this point the lens map is indeterminate and the correspondent caustics remain opened on a circle that is called pseudocaustic. We shall discuss this structure in subsection 2.6.1.

On the other side we find that the central caustics have the typical 4-cusps shape and they become smaller as m decreases. Secondary caustics are always triangular but are considerably larger for $m > 1$, a fact that was already stressed in Ref. [61]. Note that for $m > 1$ triangular caustics move right, while the central caustic is slightly displaced to the left. The opposite occurs for $m < 1$. We can find a similar behavior for standard Schwarzschild binaries with unequal masses. In practice, although we started with the same Einstein radius for both lenses, steeper profiles ($m > 1$) behave similarly to heavier masses in this regime, while shallower profiles ($m < 1$) behave as lighter masses.

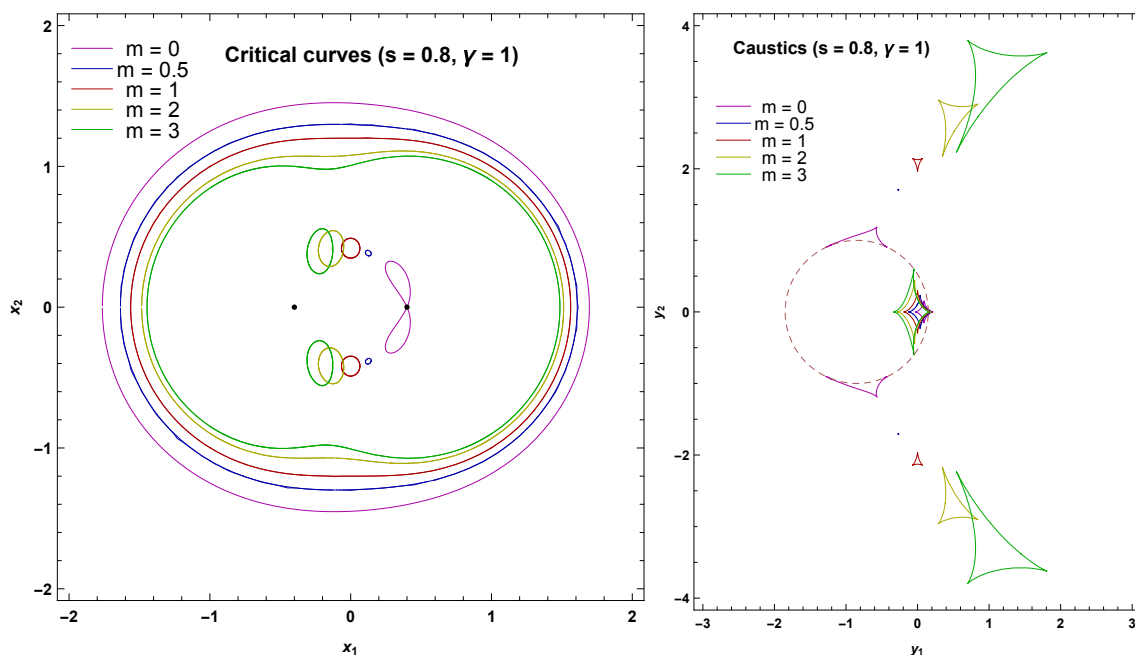


Figure 2.5: Critical curves and caustics in the equal-strength binary, close separation. Dashed magenta circle indicates the pseudocaustic for $m = 0$.

The Pseudocaustic

A pseudocaustic is a closed curve on the source plane that exists for singular distributions with zero core radius. In the singular limit, the radial critical curve collapses onto the center of the lens, leaving no space for the dim central image. When the source crosses the corresponding radial caustic, only one more image forms, while the other image is degenerate with the center of the lens. The radial caustic is then named pseudocaustic, since it behaves differently from normal caustics [68–73].

In the binary case, a pseudocaustic may still exist in the singular limit $m = 0$. Through an analytical exploration we find out the points where the two secondary triangular caustics touch the pseudocaustic.

The pseudocaustic is generated by critical curves collapsing to the center of the lens when $m = 0$. In order to explore what happens around the center of the second lens, we set

$$z = \frac{s}{2} + \epsilon_1 + i\epsilon_2; \quad (2.17)$$

we expand around zero at $1/\epsilon$ order and then we solve with respect to ϵ_2 . We get two symmetric solutions

$$\epsilon_2 = \pm \frac{\sqrt{s^2 + 1}}{\sqrt{1 - s^2}} \epsilon_1 \quad (2.18)$$

These solutions are two straight lines that cross at the origin of the system, and their angular coefficient is real only for $s < 1$. This means that the two small oval critical curves will touch the center of the $m = 0$ lens for separations in this regime. By substituting in the lens equation we find

$$\zeta = \frac{s}{2} - \frac{1}{s} \pm \gamma \sqrt{-s^2 \pm \sqrt{s^4 - 1}} \quad (2.19)$$

These are the coordinates of the four contact points of the two triangular caustics with the pseudocaustic of radius γ and center $(\frac{s}{2} - \frac{1}{s}, 0)$. The term $\frac{1}{s}$ shifts the caustic to the left side with respect to the position of the second lens $\frac{s}{2}$.

If the source only crosses the pseudocaustic, we have the sudden creation of one image of negative parity; if the source crosses a triangular caustic first and then the pseudocaustic, we have the formation of two images and the one inside the lemniscate (with positive parity) collapses on the lens.

The Elliptic Umbilic

As shown in Refs. [61, 67], in the range $0 \leq m < 1$ an *elliptic umbilic catastrophe* exists in the close separation. In an elliptic umbilic, the size of the small oval critical curves goes to zero and then grows up to finite size again. The catastrophe lies on a circle centered in the origin of the system, at the mid-point between the two lenses, and passing through them. It occurs at a specific separation s , which depends on the other parameters of the lens γ, m, n .

To find out the separation s , for any m and n , at which the catastrophe occurs we proceed as follow: first we write the system of equations

$$\begin{cases} J=0 \\ \frac{\partial J}{\partial z} = 0 \end{cases} \quad (2.20)$$

along the circle, i.e. we set

$$z = s \frac{e^{i\theta}}{2}. \quad (2.21)$$

Then we introduce a new angular variable t in order to simplify our computation

$$t = \frac{\sin^{m+1}(\theta/2)}{\cos^{n+1}(\theta/2)} \quad (2.22)$$

From Eq. ((2.20)), we get the angular position of the elliptic umbilic

$$t = \frac{(m+1)\gamma^{m+1}}{(n+1)s^{n-m}} \quad (2.23)$$

and then we finally obtain the value of s at which the catastrophe happens

$$s_{euc} = \left(\frac{1-mn}{m+1} \right)^{\frac{1}{n+1}} \sqrt{1 + \frac{\gamma^2(m+1)^{\frac{2}{n+1}}}{(n+1)^{\frac{2}{m+1}}(1-mn)^{\frac{2(m-n)}{(m+1)(n+1)}}}} \quad (2.24)$$

Note that the solution exists for $mn < 1$. In mixed binaries, we may have an elliptic umbilic also when one of the two lenses has a steep potential with $n > 1$. In order to illustrate this, we choose $n = 2$ (exotic matter) and $m = 0.25$ (a possible galactic halo). We can see, in Fig. 2.6, a zoom on the small oval critical curve for $0.714 \leq s \leq 0.834$ in steps of 0.02. The separation at which the catastrophe occurs is $s_{euc} = 0.774$. The critical curve shrinks to zero size for growing s , from $s = 0.714$ to $s = 0.774$ (lower curves) and then it grows up again. The corresponding triangular caustics behave similarly.

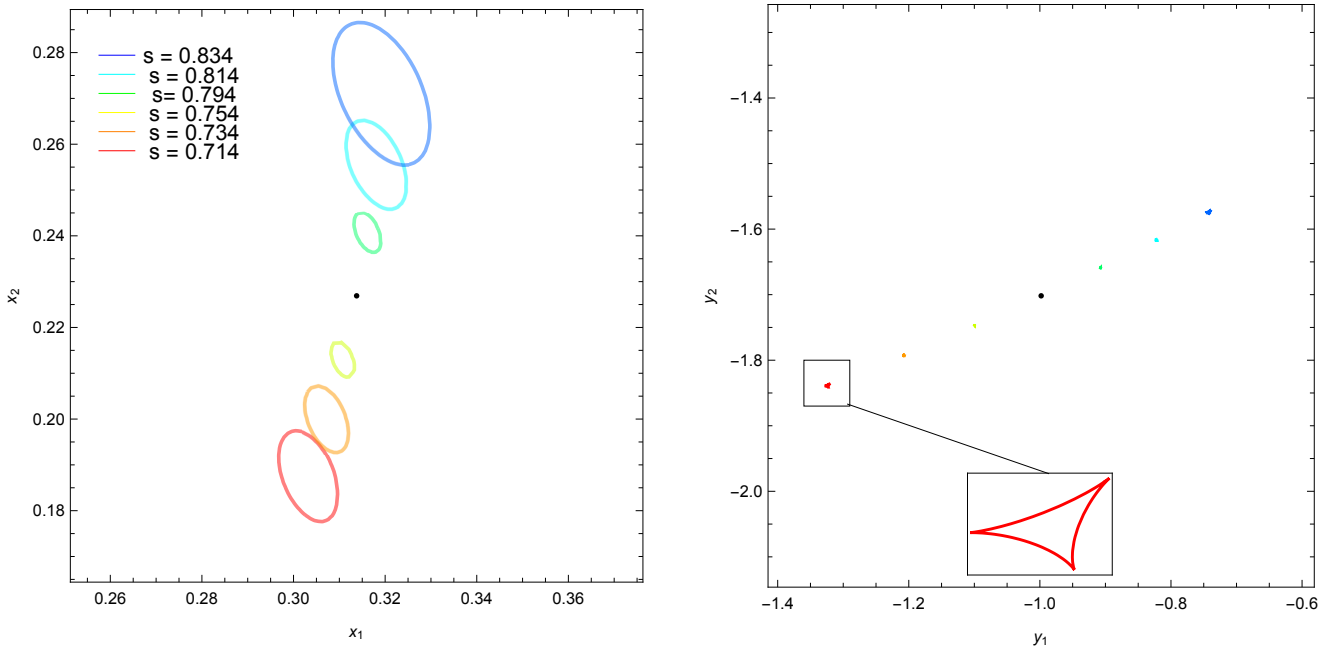


Figure 2.6: The elliptic umbilic catastrophe for $n = 2$, $m = 0.25$ and $0.714 \leq s \leq 0.834$ in steps of 0.02, one colour for each s from red to blue. The separation at which the catastrophe occurs is $s_{euc} = 0.774$. Critical curves on the left side panel, caustics on the right side panel.

2.6.2 Unequal-strength binary

In the unequal-strength binary case, in order to keep contact with the previous work, we consider $q = 0.1$, as in Ref. [61], so in terms of the ratio of the Einstein radii, our strength ratio is $\gamma = \sqrt{0.1}$. We need to multiply s in Ref. [61] by a factor $\sqrt{q+1} = \sqrt{1.1}$, so the transitions between different topologies for $n = m = 1$ occur as follows:

- close-intermediate transition, $s_{CI} = 0.807$;
- intermediate-wide transition, $s_{IW} = 1.772$.

Therefore, in this subsection we have the standard lens on the left with bigger Einstein radius than the lens on the right, for which we vary the potential index m . We shall discuss each value of m in the range $0 \leq m \leq 3$ in detail.

In Fig.2.7 we show the wide separation for $s = 2.1$. Critical curves are separated and slightly deformed. The caustic of the left side lens is smaller since the tidal field from the right side lens is normally weaker. However, for $m < 1$ the potential decays slower enough to make the left side caustic bigger than the caustic on the right.

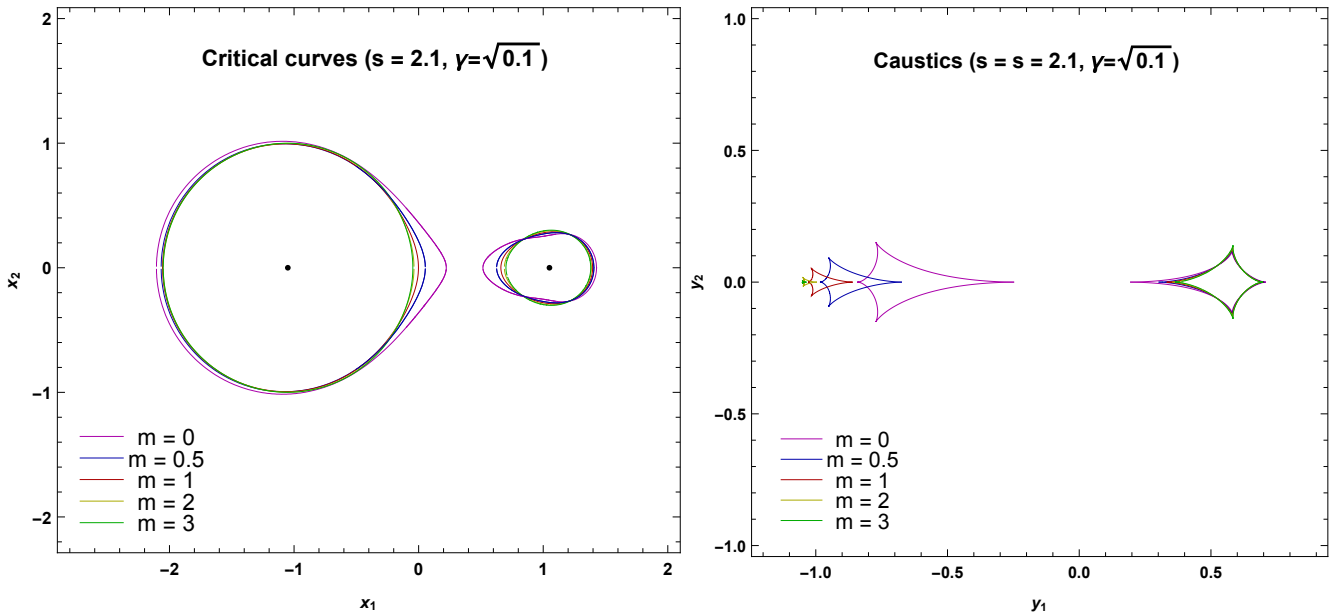


Figure 2.7: Critical curves and caustics in the unequal-strength binary, wide separation. Here and in the following figures the lens on the left has $n = 1$ and the lens on the right has variable m .

In Fig.2.8 we can see the intermediate-wide transition at $s = 1.772$.

For $m < 1$ (magenta and blue lines) the transition to the intermediate regime has already occurred, while we are still in the wide regime for $m > 1$ (green and yellow lines).

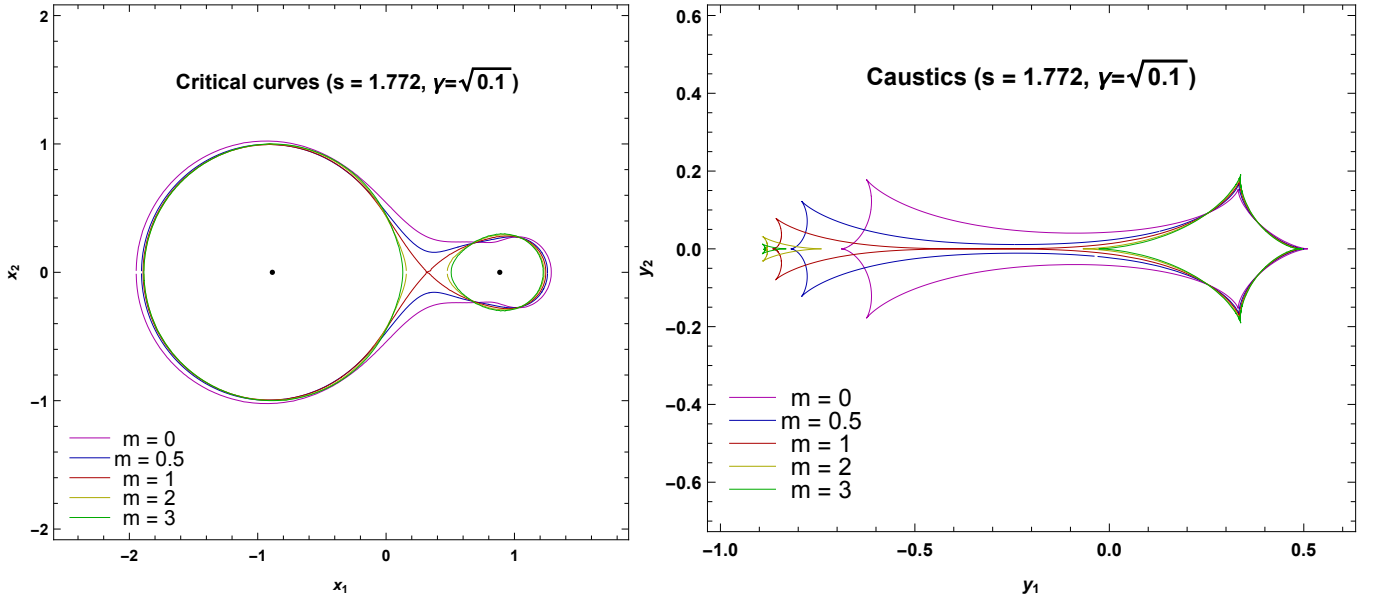


Figure 2.8: Critical curves and caustics in the unequal-strength binary, intermediate-wide transition.

In Fig.2.9 we can see the intermediate separation for $s = 1.05$.

Critical curves now are all joined and they get smaller with increasing m . Caustics now have the 6-cusps shape and they get smaller with decreasing m . Note that the throat of the critical curve is wider for $m > 2$ and narrower for $m < 1$. Correspondingly, the fold between the off-axis cusps is longer for $m > 1$ and is extremely short for $m = 0$, where the two off-axis cusps almost coincide.

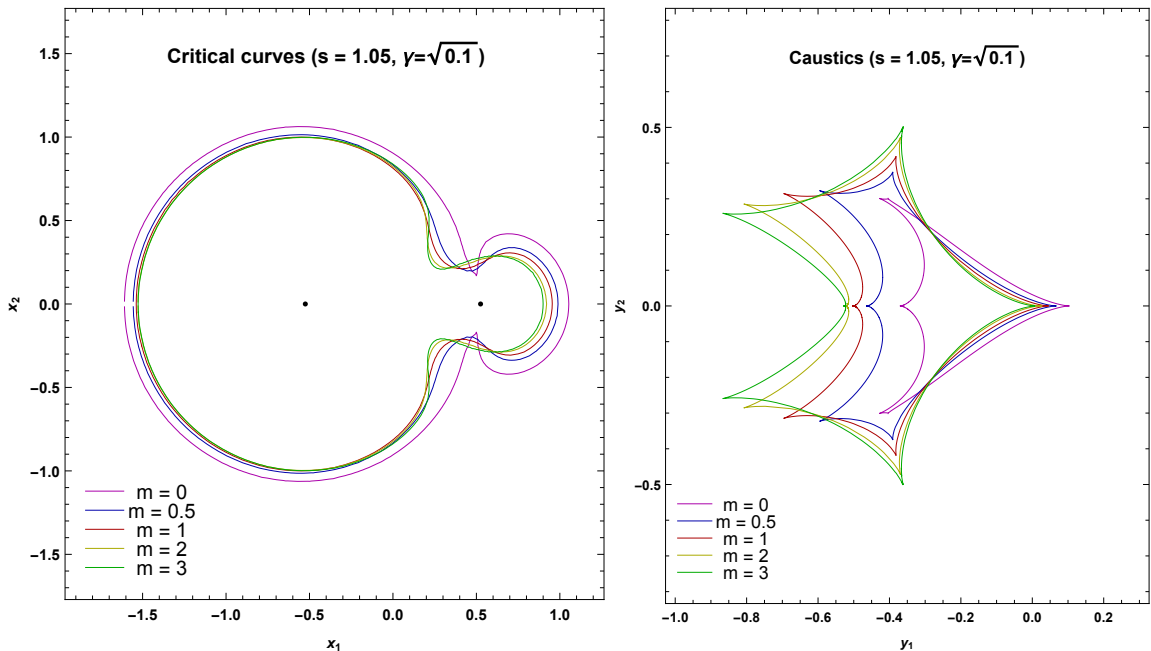


Figure 2.9: Critical curves and caustics in the unequal-strength binary, intermediate separation.

In Fig.2.10 we have the close-intermediate transition for $s = 0.807$. For $m = 0$ and $m = 0.5$, the primary caustics are already in the close regime, with the smaller ovals detached from the primary critical curve; for $m = 1$ we see the transition (red line), for $m > 1$ we are still in the intermediate

regime. Note that the $m = 0$ ovals already reached the right side lens and the triangular caustics reached the pseudocaustic.

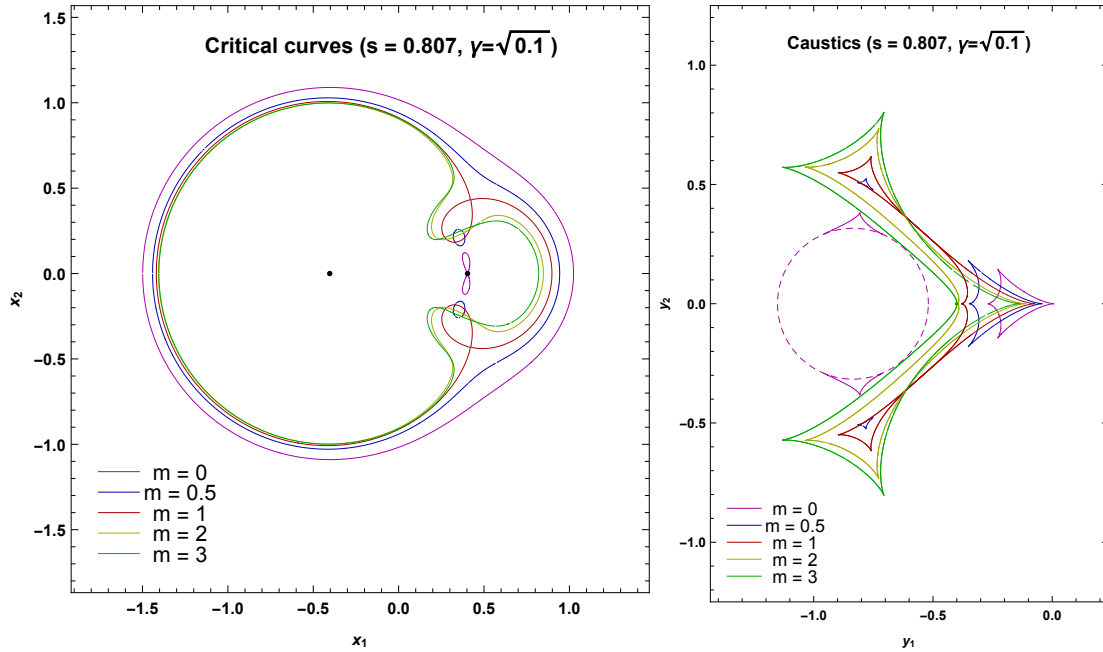


Figure 2.10: Critical curves and caustics in the unequal-strength binary, close-intermediate transition. Dashed magenta circle indicates the pseudocaustic for $m = 0$.

In Fig.2.11 we show the close separation for $s = 0.63$: the main critical curves, that generate the central caustics, are big ovals growing up in size with decreasing m . Secondary critical curves are small ovals close to the second lens, moving in the left direction as m increases. Like the equal-strength ratio case, for $m = 0$ the secondary critical curves are attached in a lemniscate shape and the corresponding caustics remain open on the pseudocaustic (see subsection 2.6.1).

On the right panel we have the caustics: as m decreases, the central caustic moves to the right; secondary caustics become larger for greater values of m .

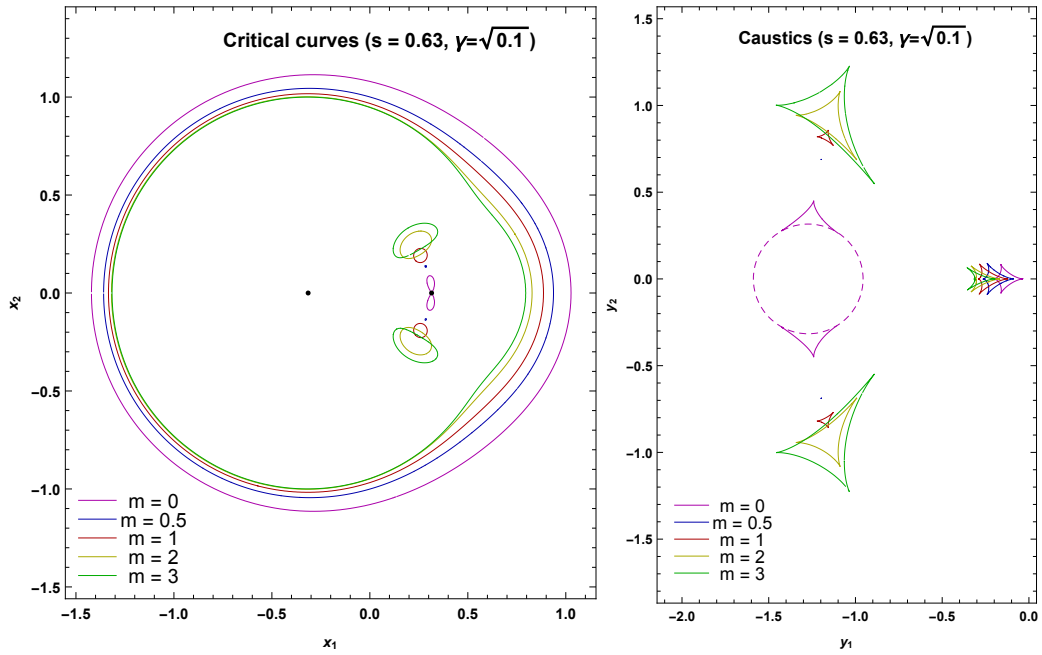


Figure 2.11: Critical curves and caustics in the unequal-strength binary, close separation. The dashed magenta circle indicates the pseudocaustic for $m = 0$.

2.6.3 Reversed unequal-strength binary

In the previous section we assumed that the bigger lens was standard ($n = 1$) and the smaller lens had a different index m . In this section we study the reverse situation: the standard lens is smaller and the other lens is bigger. We thus keep $\gamma = \sqrt{0.1}$, fix $m = 1$ and let n vary.

In Fig.2.12 we start from the wide separation. Similarly to Fig. 2.7, the caustic of the non-standard lens remains unaffected, while the caustic of the standard object strongly depends on the tidal field of the other lens. The shift and the size are much more affected than before, since now the standard lens is the weaker one.

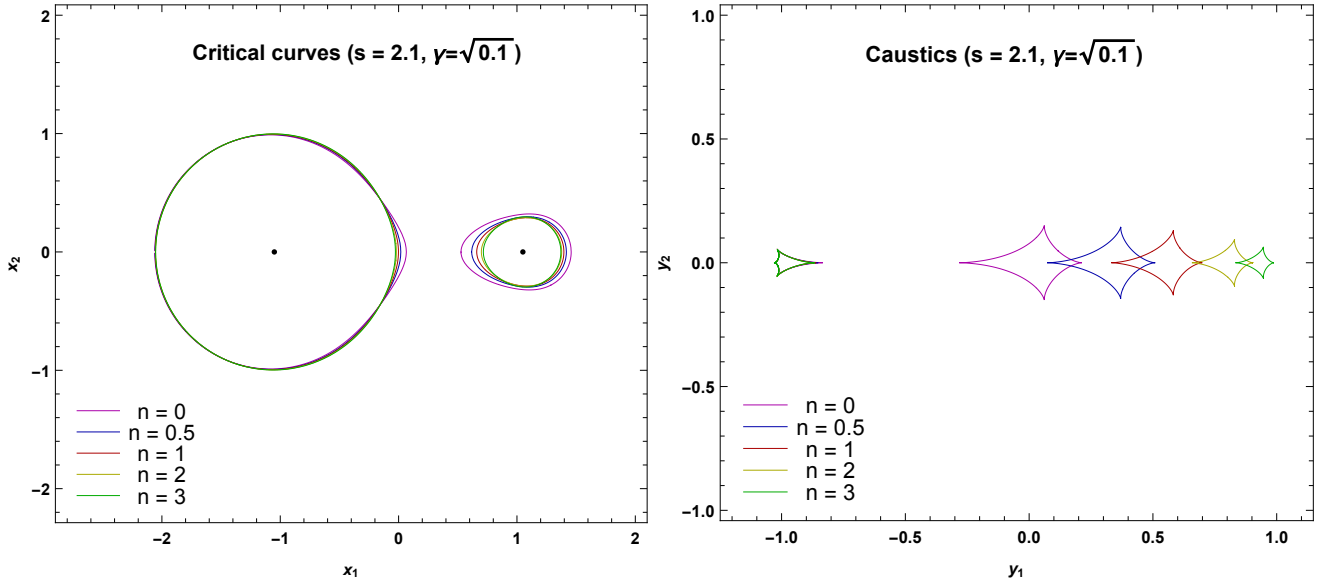


Figure 2.12: Critical curves and caustics in the unequal-strength binary with the standard lens on the right, wide separation. Here and in the following figures the lens on the right has $m = 1$ and the lens on the left has variable n .

In Fig.2.13, we are at the intermediate-wide transition. The situation is quite similar to Fig. 2.8, with stronger dependence on the index n , as discussed before.

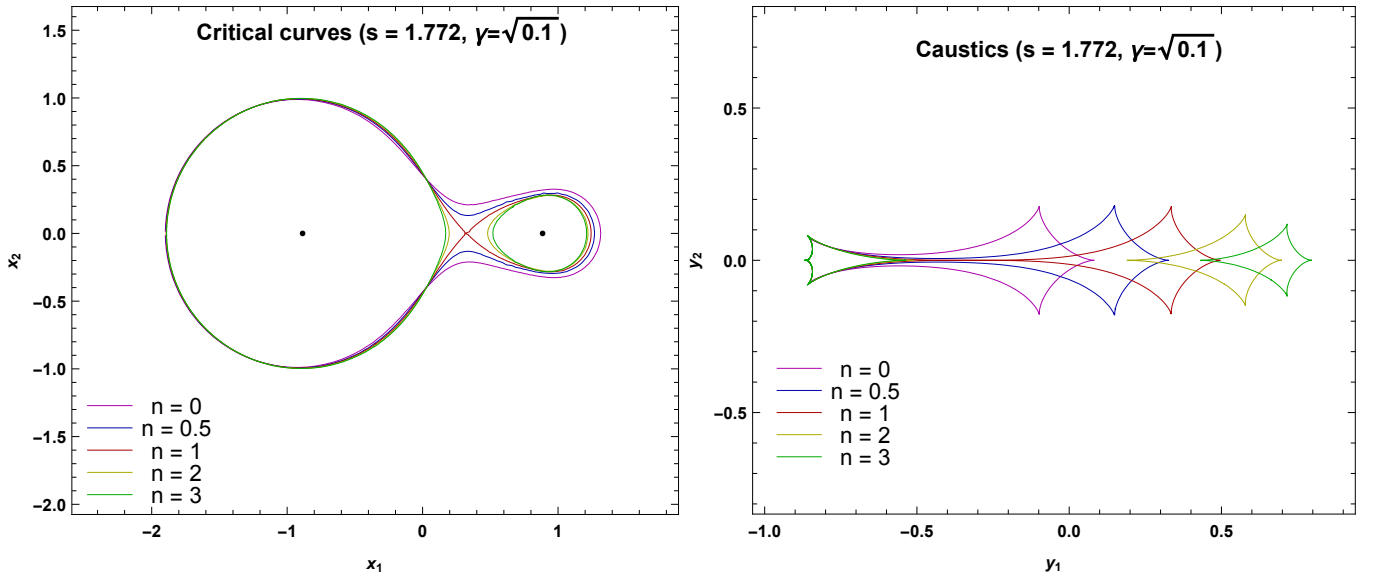


Figure 2.13: Critical curves and caustics in the unequal-strength binary with the standard lens on the right, intermediate-wide transition.

Fig.2.14 shows the intermediate topology. Comparing with Fig. 2.9, it is interesting to note that here the left cusp is common for all caustics, while there it was the right cusp to be shared among all caustics. Of course, we can still interpret this fact through the variations of the tidal fields.

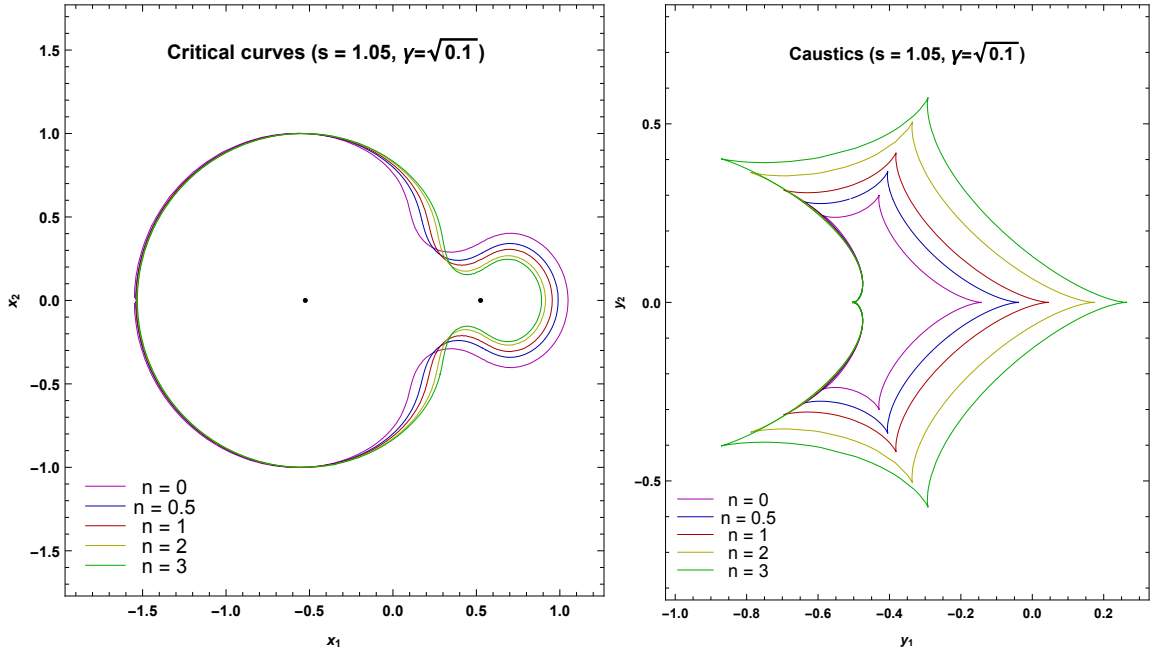


Figure 2.14: Critical curves and caustics in the unequal-strength binary with the standard lens on the right, intermediate separation.

Fig.2.15 shows the close-intermediate transition. Note that the red curves ($n = m = 1$) are exactly at the transition, while both larger and smaller n curves are in the close regime. This is not what happens in Fig. 2.10, where larger m curves were still in the intermediate regime. Then we learn that the close regime is more extended for all $n \neq 1$ in this case.

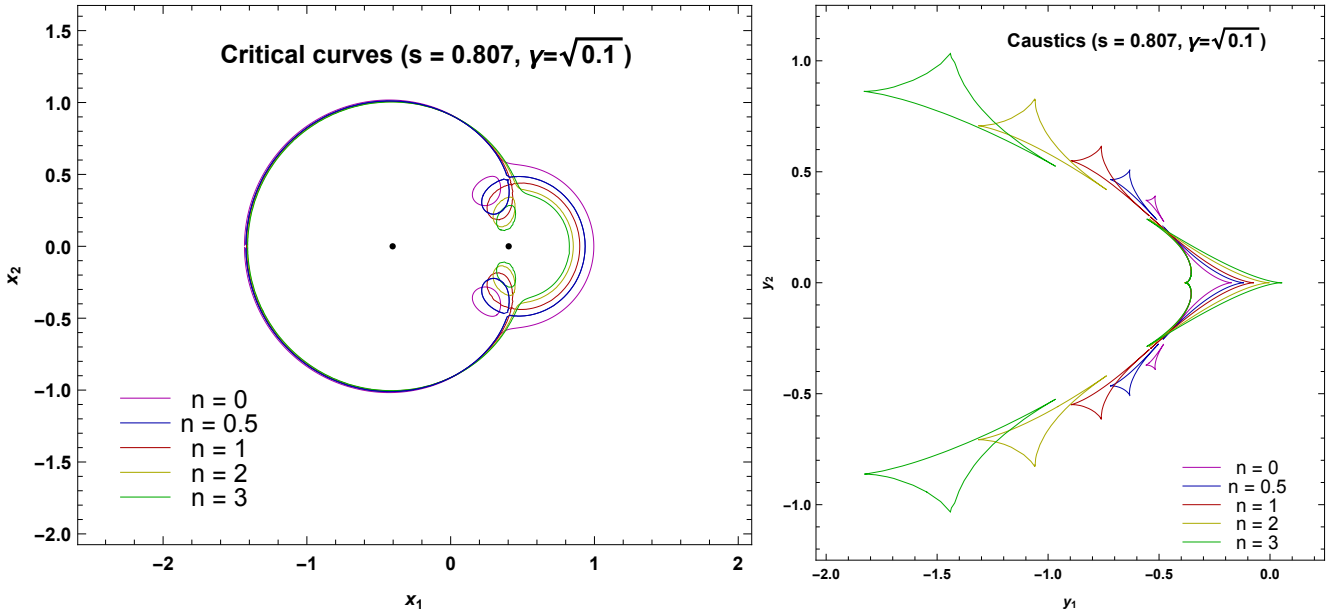


Figure 2.15: Critical curves and caustics in the unequal-strength binary with the standard lens on the right, close-intermediate transition.

Finally, Fig.2.16 shows the close regime. Note that the $n = 0$ small ovals do not collapse to the left lens but remain quite far. The pseudocaustic is never reached by the triangular caustics.

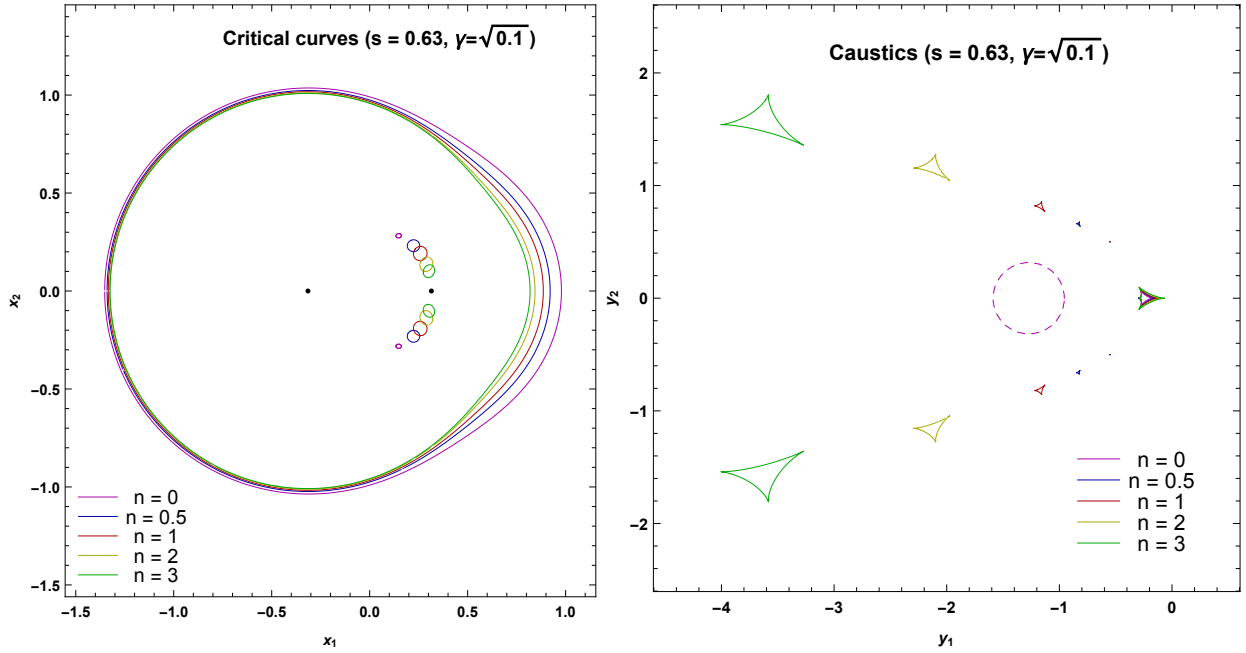


Figure 2.16: Critical curves and caustics in the unequal-strength binary with the standard lens on the right, close separation.

2.7 Transitions between different topologies

Now we want to find out the boundaries for the three topology regimes, s_{CI} and s_{IW} , for any n , m and γ .

As we know that transitions occur via higher order singularities of the lens map (beak-to-beak singularity in the binary lens case), in order to find out s_{CI} and s_{IW} we need to solve again the system of equations

$$\begin{cases} J=0 \\ \frac{\partial J}{\partial z} = 0 \end{cases} \quad (2.25)$$

We put the origin of the system in the first lens, so we rewrite the lens equation as follows

$$\zeta = z - \frac{1}{(z)^{\frac{n-1}{2}} (\bar{z})^{\frac{n+1}{2}}} - \frac{\gamma^{m+1}}{(z-s)^{\frac{m-1}{2}} (\bar{z}-s)^{\frac{m+1}{2}}} \quad (2.26)$$

the Jacobian determinant is

$$J = \frac{1}{4} \left[\left(2 + \frac{n-1}{z^{\frac{n+1}{2}} \bar{z}^{\frac{n+1}{2}}} + \frac{(m-1)\gamma^{m+1}}{(z-s)^{\frac{m+1}{2}} (\bar{z}-s)^{\frac{m+1}{2}}} \right)^2 - \left(\frac{n+1}{z^{\frac{n+3}{2}} \bar{z}^{\frac{n-1}{2}}} + \frac{(m+1)\gamma^{m+1}}{(z-s)^{\frac{m+3}{2}} (\bar{z}-s)^{\frac{m-1}{2}}} \right) \left(\frac{n+1}{z^{\frac{n-1}{2}} \bar{z}^{\frac{n+3}{2}}} + \frac{(m+1)\gamma^{m+1}}{(z-s)^{\frac{m+1}{2}} (\bar{z}-s)^{\frac{m+3}{2}}} \right) \right] \quad (2.27)$$

and

$$\begin{aligned} \frac{\partial J}{\partial z} = \frac{1}{4} \left\{ \frac{1}{2} \left[\left(\frac{n+1}{z^{\frac{n+3}{2}} \bar{z}^{\frac{n+1}{2}}} + \frac{(m+1)\gamma^{m+1}}{(z-s)^{\frac{m+3}{2}} (\bar{z}-s)^{\frac{m-1}{2}}} \right) \left(\frac{n^2-1}{z^{\frac{n+1}{2}} \bar{z}^{\frac{n+3}{2}}} + \frac{(m^2-1)\gamma^{m+1}}{(z-s)^{\frac{m+1}{2}} (\bar{z}-s)^{\frac{m+3}{2}}} \right) + \right. \right. \\ \left. \left(\frac{(n+1)(n+3)}{z^{\frac{n+5}{2}} \bar{z}^{\frac{n-1}{2}}} + \frac{(m+1)(m+3)\gamma^{m+1}}{(z-s)^{\frac{m+5}{2}} (\bar{z}-s)^{\frac{m-1}{2}}} \right) \left(\frac{n+1}{z^{\frac{n-1}{2}} \bar{z}^{\frac{n+3}{2}}} + \frac{(m+1)\gamma^{m+1}}{(z-s)^{\frac{m-1}{2}} (\bar{z}-s)^{\frac{m+3}{2}}} \right) \right] \\ \left. - \left(2 + \frac{n-1}{z^{\frac{n+1}{2}} \bar{z}^{\frac{n+1}{2}}} + \frac{(m-1)\gamma^{m+1}}{(z-s)^{\frac{m+1}{2}} (\bar{z}-s)^{\frac{m+1}{2}}} \right) \left(\frac{n^2-1}{z^{\frac{n+3}{2}} \bar{z}^{\frac{n+1}{2}}} + \frac{(m^2-1)\gamma^{m+1}}{(z-s)^{\frac{m+3}{2}} (\bar{z}-s)^{\frac{m+1}{2}}} \right) \right\} \end{aligned} \quad (2.28)$$

Here we show the analytical procedure to find out s_{IW} ; the other transition, s_{CI} , is only found numerically.

We require $z = \bar{z}$ because the beak-to-beak singularity for the intermediate-wide transition occurs along the line that joins the two lenses, and we introduce two variables

$$y_1 = \frac{(s-z)^{m+1}}{z^{n+1}}, y_2 = \frac{(s-z)^{m+2}}{z^{n+2}} \quad (2.29)$$

we replace y_1 in Eq. (2.27), we solve and we get

$$y_1 = \frac{z^{n+1} - 1}{\gamma^{m+1}}, \quad (2.30)$$

we substitute y_2 in Eq. (2.28), we solve and we find

$$y_2 = \frac{n+1}{(m+1)\gamma^{m+1}}. \quad (2.31)$$

We use Eqs. (2.30) and (2.31) in Eqs. (2.29), we find two new equations and by a combination of them we get a complicated expression for z

$$\frac{\gamma^{\frac{m+1}{n+2}} \left(1 + \gamma^{\frac{n+1}{n+2}}\right)^{m+1} \left[z + \left(\frac{m+1}{n+1}\right)^{\frac{1}{m+2}} \gamma^{\frac{m+1}{m+2}} z^{\frac{n+2}{m+2}} \right]^{n-m}}{\left[z + \left(\frac{m+1}{n+1}\right)^{\frac{1}{m+2}} \gamma^{\frac{m+1}{m+2}} z^{\frac{n+2}{m+2}} \right]^{n+1} - \left(1 + \gamma^{\frac{n+1}{n+2}}\right)^{n+1}} = 1 \quad (2.32)$$

that we can solve only numerically. We call this numerical solution z_{IW} . Finally we get the value of the intermediate-wide transition for general n and m

$$s_{IW} = z_{IW} + (\gamma^{m+1} z_{IW}^{n+2} \frac{m+1}{n+1})^{\frac{1}{m+2}}. \quad (2.33)$$

In Fig. 2.17, upper panel, we plot the cases with fixed $n = 1$ and variable m (upper curves). The close-intermediate transition s_{CI} is found numerically (lower curves). We can see that the value of s_{IW} increases with γ and that the transition occurs earlier for greater values of m . The value of s_{CI} has a different behaviour: first it decreases with increasing γ , with a minimum around $\gamma = 0.5$, and then it starts to grow up again. Also in this case the transition occurs earlier for greater values of m . We remind the reader that we are working in units of the Einstein radius of the first lens.

For the reversed binary case, in Fig. 2.17, lower panel, we plot the cases with fixed $n = 1$ and variable m . We can see that the value of s_{IW} increases with γ similarly to the case with fixed m . For s_{CI} all curves are very closely packed and have a minimum for a value of γ that depends on the specific choice of n . In particular, for $\gamma = \sqrt{0.1}$, corresponding to the situation in Fig. 2.15, the transition occurs for $n = 1$ at smaller separation than for all other curves.

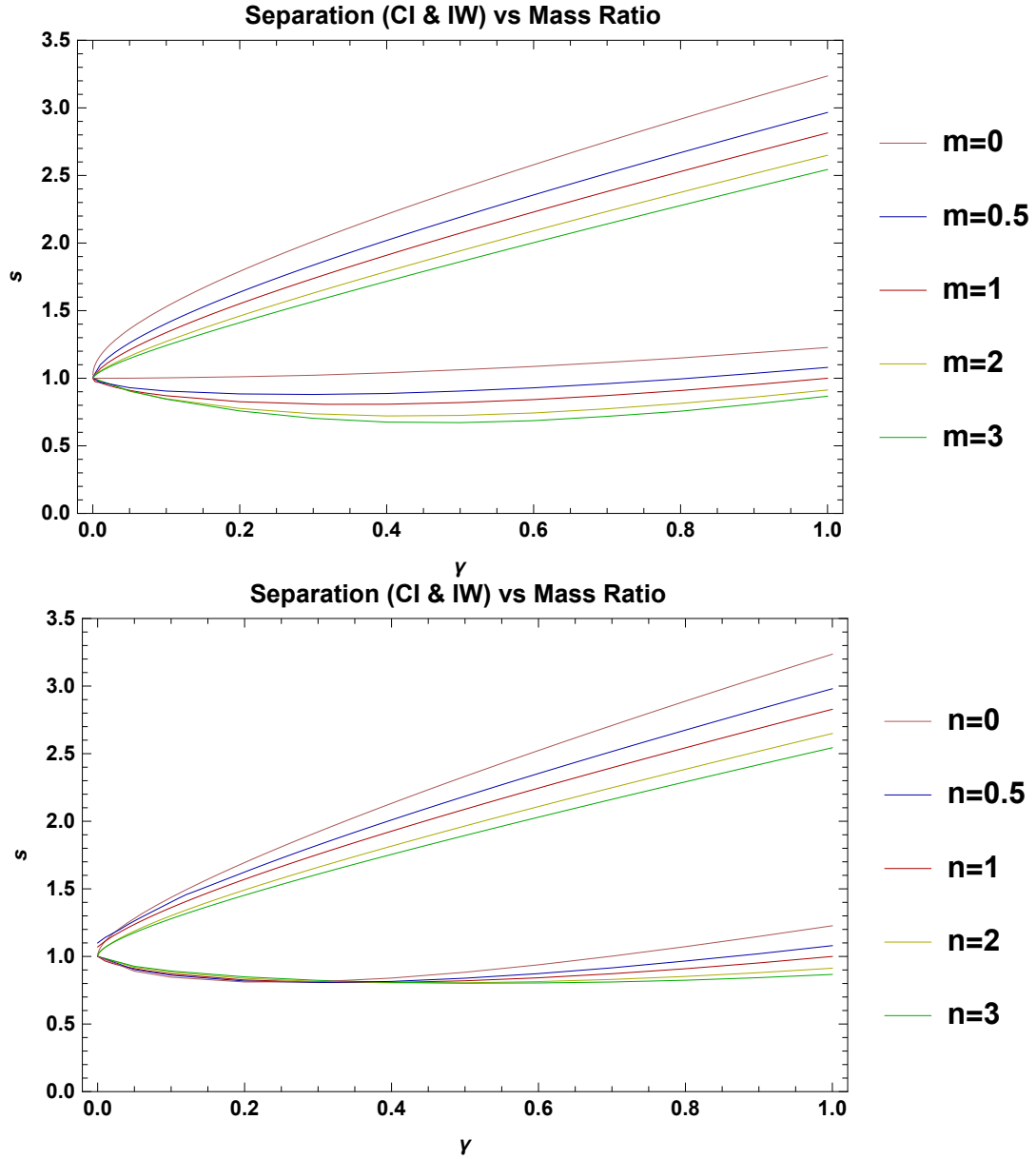


Figure 2.17: Critical values of the separation for the intermediate-wide transition s_{IW} as a function of γ (upper curves); critical values of the separation for the close-intermediate transition s_{CI} as a function of γ (lower curves). The upper panel is for $n = 1$ and variable m ; the lower panel is for $m = 1$ and variable n .

2.8 Analytical Approximations

In order to remark the differences with the Schwarzschild case $n = m = 1$ and to have a deeper understanding in the caustics evolution, we now want to explore the analytical approximations obtained for the most general case, varying both n and m . In particular, we will investigate the wide binary regime and the very small γ regime, but we are not able to get analytical results for the close binary regime. The main difficulty comes from the fact that the starting point of the expansion would have the two lenses coinciding in the origin, but the resulting Einstein radius can only be calculated numerically. Therefore, even the zero order is not analytic.

2.8.1 Wide Binary

Let us consider the wide binary regime with $s \gg 1$: the case in which an isolated object is perturbed by another one at a distance much greater than the Einstein radius θ_E . We can set the origin of our system in the first lens ($z_A = 0$ and $z_B = s$), so we can use the same lens equation written in Eq. (2.26) and the Jacobian determinant in Eq. (2.27). The perturbing object deforms the circular critical curve of the main object with radius ρ and we can find out this deformation δ through a perturbative approach.

We set

$$z = \rho(1 + \delta)e^{i\theta} \quad (2.34)$$

and we substitute in J . In our case $\rho = 1$ (because for $s \rightarrow \infty$ the radius of the critical curves is the Einstein radius, which, in our case, is $\theta_{E,A} = 1$), and take $\delta = O(1/s^{m+1})$. We perform a power series expansion for J about the zero point with respect to $1/s$ at first order. Then, we solve $J = 0$ and find the correction to the critical curve

$$\delta = \frac{\gamma^{m+1}[1 - m + (m + 1)\cos(2\theta)]}{2(n + 1)s^{m+1}} \quad (2.35)$$

Now we put Eq. (2.34) in Eq. (2.26) and we expand around zero with respect to $1/s$ at first order, and we take the real and the imaginary parts

$$\text{Re}[\zeta(\theta)] = \frac{\gamma^{m+1}}{s^m} + \frac{(m + 1)\gamma^{m+1}\cos^3(\theta)}{s^{m+1}} \quad (2.36)$$

$$\text{Im}[\zeta(\theta)] = -\frac{(m + 1)\gamma^{m+1}\sin^3(\theta)}{s^{m+1}} \quad (2.37)$$

The real part contains the shift $\frac{\gamma^{m+1}}{s^m}$ of the caustic toward the direction of perturbing object as we can see in Figs. (2.1), (2.7), (2.12).

The other term, $\cos^3(\theta) + i \sin^3(\theta)$, describes the shape of the caustic (the 4-cusps astroid) that remains unchanged by varying m . The coefficient $\gamma^{m+1} \frac{(m+1)}{s^{m+1}}$ gives the size of the caustic.

In these approximations the error is given by a term $O(\gamma^2)$.

2.8.2 Extremely unequal-strength ratio limit

Now we study the caustic evolution in the extreme limit $\theta_{E,B} \ll \theta_{E,A}$ for the close and wide separations. We remind that, in the case of two Schwarzschild objects ($n = m = 1$) this is the so-called "planetary" limit.

Central Caustic

We put the origin of our system in the first lens ($z_A = 0$), the perturbing object is at $z_B = -s$ and we rewrite the lens equation as follow

$$\zeta = z - \frac{1}{(z)^{\frac{n-1}{2}} (\bar{z})^{\frac{n+1}{2}}} - \frac{\gamma^{m+1}}{(z+s)^{\frac{m-1}{2}} (\bar{z}+s)^{\frac{m+1}{2}}} \quad (2.38)$$

and the Jacobian determinant is

$$J = \frac{1}{4} \left[\left(2 + \frac{n-1}{z^{\frac{n+1}{2}} \bar{z}^{\frac{n+1}{2}}} + \frac{(m-1)\gamma^{m+1}}{(z+s)^{\frac{m+1}{2}} (\bar{z}+s)^{\frac{m+1}{2}}} \right)^2 - \left(\frac{n+1}{z^{\frac{n+3}{2}} \bar{z}^{\frac{n-1}{2}}} + \frac{(m+1)\gamma^{m+1}}{(z+s)^{\frac{m+3}{2}} (\bar{z}+s)^{\frac{m-1}{2}}} \right) \left(\frac{n+1}{z^{\frac{n-1}{2}} \bar{z}^{\frac{n+3}{2}}} + \frac{(m+1)\gamma^{m+1}}{(z+s)^{\frac{m+1}{2}} (\bar{z}+s)^{\frac{m+3}{2}}} \right) \right] \quad (2.39)$$

For the critical curve of the main lens, we use the parametrization in J

$$z = (1 + \delta)e^{i\theta} \quad (2.40)$$

where $\delta = O(\gamma^{m+1})$.

We expand around zero with respect to γ^{m+1} to first order, solve $J = 0$ and we find the correction of the circular critical curve

$$\delta = \frac{2 + 4s \cos \theta + s^2[(m+1) \cos(2\theta) - m + 1]}{2(n+1)(1 + 2s \cos \theta + s^2)^{\frac{m+3}{2}}} \gamma^{m+1}. \quad (2.41)$$

Now we substitute this δ in Eq. (2.38) and we get the caustic

$$\zeta = (1 + \delta)e^{i\theta} - \frac{1}{[(1 + \delta)e^{i\theta}]^{\frac{n-1}{2}} [(1 + \delta)e^{-i\theta}]^{\frac{n+1}{2}}} - \frac{\gamma^{m+1}}{[(1 + \delta)e^{i\theta} + s]^{\frac{m-1}{2}} [(1 + \delta)e^{-i\theta} + s]^{\frac{m+1}{2}}} \quad (2.42)$$

In order to find the size of the caustic, we expand the lens equation around zero to first order in γ^{m+1} and we evaluate it for $\theta = 0$ and $\theta = \pi$. We have

$$\Delta\zeta = \zeta(0) - \zeta(\pi) = s\gamma^{m+1} \left[\frac{1}{(s-1)^{m+1}} - \frac{1}{(s+1)^{m+1}} \right] \quad (2.43)$$

and this is the distance between the left and the right cusp. We find that Eq. (2.42) is invariant under the transformation

$$s \rightarrow \frac{1}{s}, \gamma^{m+1} \rightarrow \frac{\gamma^{m+1}}{s^{m-1}}. \quad (2.44)$$

which expresses the duality of the close-wide regimes in our mixed binary framework.

Caustics of the Perturbing Object

We put the origin of our system in the second lens so that $z_A = -s$ and $z_B = 0$ and the lens equation becomes

$$\zeta = z - \frac{1}{(z+s)^{\frac{n-1}{2}} (\bar{z}+s)^{\frac{n+1}{2}}} - \frac{\gamma^{m+1}}{z^{\frac{m-1}{2}} \bar{z}^{\frac{m+1}{2}}} \quad (2.45)$$

we rewrite the Jacobian determinant as follows

$$J = \frac{1}{4} \left[\left(2 + \frac{n-1}{(z+s)^{\frac{n+1}{2}} (\bar{z}+s)^{\frac{n+1}{2}}} + \frac{(m-1)\gamma^{m+1}}{(z)^{\frac{m+1}{2}} (\bar{z})^{\frac{m+1}{2}}} \right)^2 - \left(\frac{n+1}{(z+s)^{\frac{n+3}{2}} (\bar{z}+s)^{\frac{n-1}{2}}} + \frac{(m+1)\gamma^{m+1}}{z^{\frac{m+3}{2}} \bar{z}^{\frac{m-1}{2}}} \right) \left(\frac{n+1}{(z+s)^{\frac{n-1}{2}} (\bar{z}+s)^{\frac{n+3}{2}}} + \frac{(m+1)\gamma^{m+1}}{z^{\frac{m+1}{2}} \bar{z}^{\frac{m+3}{2}}} \right) \right] \quad (2.46)$$

and we introduce a new expression for z

$$z = \rho^{\frac{1}{m+1}} \gamma e^{i\theta}. \quad (2.47)$$

We substitute in Eq. (2.46) and we expand with respect to γ^{m+1} , around zero at zero order and the Jacobian determinant becomes

$$\frac{(\rho-1)(\rho+m)}{\rho^2} + \frac{(n-1)(m+2\rho-1) - (m+1)(n+1)\cos(2\theta)}{2\rho s^2} - \frac{n}{s^{2n+2}} = 0 \quad (2.48)$$

Then we solve Eq. (2.48), $J = 0$, with respect to ρ and we find two solutions

$$\rho_{\pm} = \frac{(m-1)\{s^{n+1}[(1-n) + (m+1)(n+1)\cos(2\theta) - 2s^{n+1}] \pm \sqrt{\Delta}\}}{4(s^{n+1}-1)(s^{n+1}+n)} \quad (2.49)$$

$$\Delta = s^{2n+2}\{[(m-1)(2s^{n+1}+n-1) - (m+1)(n+1)\cos(2\theta)]^2 + 16m(s^{n+1}-1)(s^{n+1}+n)\} \quad (2.50)$$

We have two scenarios: for external objects (when the secondary lens is outside the Einstein ring of the main lens, $s > 1$) the critical curves are elongated rings, see Fig. (2.12); for internal objects (when the secondary lens is inside the critical curve of the main lens, $s < 1$) it generates two specular ovals, see Fig. 2.16.

In order to get the caustics we put our solutions in the lens equation and we get, at first order:

$$\zeta = \gamma \rho^{\frac{1}{m+1}} \left[e^{i\theta} \left(\frac{n-1}{2s^{n+1}} - \frac{1}{\rho} + 1 \right) + \frac{e^{-i\theta}(n+1)}{2s^{n+1}} \right] - \frac{1}{s^n} \quad (2.51)$$

From Eq. (2.51) we can get all the information for the size and for the displacement of the secondary caustic from the central one.

The displacement along the axis that joins the two lenses is the middle point $[\zeta(0) + \zeta(\pi)]/2$ and in our case is

$$\zeta_{center} = s - \frac{1}{s^n}. \quad (2.52)$$

because the origin of our system is in the second lens.

Now we want to find out the size of the caustics in the close and wide separation. For the wide case we have an extension of the caustics in the parallel direction (with respect to the lens axis), given by $[\zeta(0) - \zeta(\pi)]$

$$\Delta\zeta_{\parallel,wide} = 2(n+1) \frac{\gamma}{s^{\frac{m(n+1)}{m+1}} (s^{n+1} - 1)^{\frac{1}{m+1}}} \quad (2.53)$$

and in the vertical direction, orthogonal to lens axis, $[\zeta(-\pi/2) - \zeta(\pi/2)]$:

$$\Delta\zeta_{\perp,wide} = 2(n+1) \frac{\gamma}{s^{\frac{m(n+1)}{m+1}} (s^{n+1} + n)^{\frac{1}{m+1}}} \quad (2.54)$$

In Fig.2.18, upper panel, we show the size of the caustic for three different fixed $n = 0.5, 1, 2$ with variable m

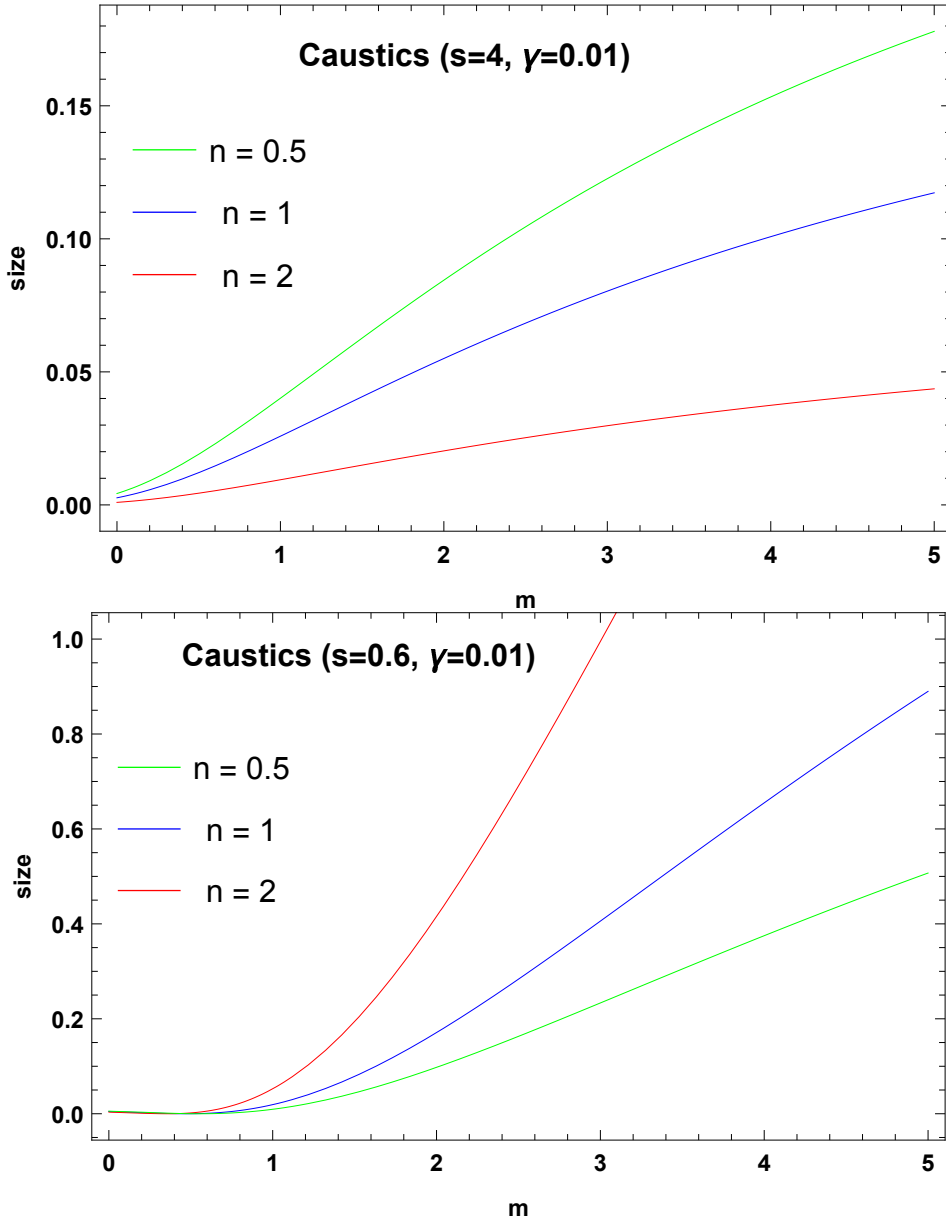


Figure 2.18: Upper panel: size of the caustic in the wide case for $s = 4$, $\gamma = 0.01$, for three different fixed $n = 0.5, 1, 2$, with variable m . Lower panel: size of the caustic in the close case for $s = 0.6$, $\gamma = 0.01$, for three different fixed $n = 0.5, 1, 2$, with variable m .

and we can see that the size grows up with increasing m , slower for larger n .

In the close regime, in order to find the position of the central caustic, we evaluate the lens equation in ρ_{\pm} for $\theta = \pm\pi/2$ and we need to distinguish the case $mn > 1$ from the case $mn < 1$ changing the sign after taking the square root.

We put $\theta = \pi/2$ and ρ_+ in Eq. (2.51), we take the imaginary part and we find

$$Im[\zeta_+(\pi/2)] = \begin{cases} (m+1)\gamma \left[\frac{(1-s^{n+1})}{ms^{n+1}} \right]^{\frac{m}{m+1}}, & \text{if } mn < 1 \\ (n+1)\gamma \left[\frac{1}{s^{m(n+1)}(n+s^{n+1})} \right]^{\frac{1}{m+1}}, & \text{if } mn > 1 \end{cases}, \quad (2.55)$$

and to find the position of the two secondary caustics we need to calculate $\zeta(\pi/2)$ with ρ_- , then we

take the imaginary part and we find

$$Im[\zeta_-(\pi/2)] = \begin{cases} (n+1)\gamma \left[\frac{1}{s^{m(n+1)}(n+s^{n+1})} \right]^{\frac{1}{m+1}}, & \text{if } mn < 1 \\ (m+1)\gamma \left[\frac{(1-s^{n+1})}{ms^{n+1}} \right]^{\frac{m}{m+1}}, & \text{if } mn > 1 \end{cases}, \quad (2.56)$$

The measure of the transverse size of the secondary caustics is the difference between the last two formulas, $Im[\zeta_+(\pi/2)] - Im[\zeta_-(\pi/2)]$ and we plot the result in Fig. 2.18, lower panel, for $s = 0.6$, $\gamma = 0.01$, for three different fixed $n = 0.5, 1, 2$, with variable m .

We can see that the size increases with m , quicker for larger n . We underline that, for $mn < 1$, and so for $n = 0.5$ especially (green line), the two branches exchange role because of the elliptic umbilic catastrophe. Then, we must change the sign in our formula for the size.

In these approximations the error is given by a term $O(1/s^{m+2})$.

2.9 Discussion

In this chapter we have generalized the previous study of binary lenses with $1/r^n$ potential [61], by extending it to the case of mixed binaries. Of course the mathematics of this general case is interesting from several points of view, since many earlier results are put in a more general context. However, this case is also important from the astrophysical point of view. In fact, we now have the critical curves and caustics of pairs of galaxies with different halos, or we may apply our results to cases in which one object is made up of exotic matter and the other one is a normal star.

Our figures, together with those of Ref. [61] may be considered as a complete atlas of critical curves and caustics in binary lensing by $1/r^n$ potentials. We have studied different limits in which the stronger (weaker) lens has a steeper (gentler) potential in all three topology regimes.

We have shown that an elliptic umbilic catastrophe exists for $mn < 1$ and calculated its position. We have also described the pseudocaustic in the $m = 0$ limit. We have calculated the boundaries of the three topology regimes and provided analytic approximations for the wide binary and the extremely small-strength secondary lens.

With respect to the $m = n$ binary lens case, we note that for large m we still have large secondary triangular caustics, but they are not as giant as those in Ref. [61]. In fact, the presence of a more standard lens in the system mitigates the behavior at large distances and pushes back these caustics to more normal sizes. Indeed, these structures are quite sensitive to the parameters of the lens.

This fact helps us recall that the mixed binary lens described here is still obtained by the linear superposition of the potentials of two isolated objects. This is physically relevant whenever we can

neglect the non-linear terms in Einstein equations. Even when this is not possible, our results may serve as a basis for more accurate calculations. The complete work was published on *Universe* in 2020 [78].

CHAPTER 3

FROM THEORY TO OBSERVATIONAL EFFECTS: S2, SGR A* AND THE S-STARS

3.1 Motivations

The Galactic Center (GC) is one of the most attractive regions of the Milky Way that has been monitored for about three decades [79]. The Sgr A complex of radio sources extends over the central 10 parsecs of our Galaxy. A compact object called Sgr A* with a mass of several million solar masses lies in its center, traditionally accepted as a massive black hole (MBH) [80, 81]. A striking confirmation of this conclusion has come from the recent release of the image of the shadow of the black hole from the Event Horizon Collaboration [82].

The central parsec hosts old, late-type red giants, supergiants, asymptotic giant branch stars, but also many hot young, early-type stars, like post-main sequence blue supergiants and Wolf-Rayet stars [83–93], and two different observational campaigns from VLT and Keck observatories, revealed a hundred of B stars within 1 arcsecond in the neighborhood of Sgr A*, known as the S-stars [85, 87–89, 94]. Many of the orbits of these stars have been reconstructed in detail after many years of observations.

De Paolis et al. [95] showed that the binary system S2-Sgr A* offers an opportunity to study the retro-lensing phenomenon proposed by Holz & Wheeler [96], taking advantage of both the large black hole (BH) mass and the small separation of the binary components. Bozza and Mancini [97] calculated the light curves for the secondary and the first two relativistic images, in the Schwarzschild black hole hypothesis for S2, S12, S14, S1, S8, and S13, throughout their orbital periods showing that for most of these stars the secondary image should be observable during its brightness peak.

Amitai and Bin-Nun [98] add in a $1/r^2$ term to the Schwarzschild metric near Sgr A* in order to determine the effect of this extra term on the properties of the secondary images of the S-stars in the GC showing that when this term is positive, this represents a Reissner-Nordstrom (RN) metric, leading to the conclusion that secondary images may not be a useful probe of electrical charge in black holes, while a negative value for the term can enter through modified gravity scenarios.

Zakharov et al. [99] consider shadows around black holes as a tool to evaluate their parameters by analyzing Kerr and Reissner-Nordström cases and for a significant charge one can expect that geodesics of bright stars near the black hole and their observed fluxes may be different for these metrics due to a difference in gravitational lensing. Therefore, a deviation from the Schwarzschild case flux may be measured for a significant charge and the signature of extra dimensions may found. However, as a theoretical analysis shows that a tidal charge has to be very close to zero and a suggested charge value which may lead to measurable flux deviations for S2 like stars (or their essential displacements or astrometrical lensing) is not consistent with observational constraints on a shadow size.

The possibility of determining the spin of the SMBH in Sgr A* by using secondary images of stars orbiting it was explored by [100].

Strong gravitational lensing effects around rotating black holes in different gravity theories were explored by [101] and also by [102] for a photon sphere in spherically symmetric regular electrically charged (REC) black hole and with those by corresponding REC no-horizon spacetimes, where in a no-horizon spacetime images by lensing from the inside of the photon sphere can also appear and the deflection angle α also increases with the impact parameter u ; the lensing observables were analyzed by modeling Sgr A* and the REC black holes agree with the EHT results in finite space. The results offered by the EHT gave motivation to study gravitational lensing in strong-field limit by a static spherically symmetric black hole in quartic scalar field Horndeski gravity having additional hair parameter [103] where an increase in the deflection angle, photon sphere radius, and angular position is found. The astrophysical consequences in the supermassive black holes at the center of several galaxies was also discussed. Rahman and Sen [104] studied the strong lensing and time delay effect of static spherically symmetric black hole solutions for the case of gravitational lensing of the star S2 by Sgr A*, they constructed the rotating black hole solution from this static spherically symmetric solution in Proca theories using the Newman-Janis algorithm and they studied lensing, time delay and black hole shadow effect in this rotating black hole spacetime. The axially symmetric counterpart of an existing spherical hairy black hole in Horndeski gravity was presented by [105].

Signatures from charged black holes were also investigated by [106] in the weak and strong deflection limit, the SMBH in the GC is taken as the lens, and the observables are evaluated in order to compare these signatures with those of the Schwarzschild, Reissner-Nordström, tidal

Reissner-Nordström and charged Galileon black holes.

A major breakthrough in the astrometric precision in these campaigns has been achieved when GRAVITY became operational. GRAVITY is an interferometer part of the second generation of VLTI [107–110], the Very Large Telescope Interferometer. GRAVITY observed Sgr A* for 6 months in 2019 in order to detect the weakest objects closer to it and follow their movement across the sky.

Indeed, the major result of these observations has been the detection of the relativistic precession of the star S2 [111], which has marked an exceptional milestone for General Relativity (GR), astrophysical black holes and Near Infrared interferometric observations. S2 is characterized by the most favorable characteristics for such gravity test: it is bright enough for clear detection both in astrometry and spectroscopy, it has a relatively small orbital period of about 16 years, it comes as close as 120 au to the central black hole. Its nearly elliptical orbit only perturbed by GR effects is evidence of the existence of a massive compact object located at its focus.

Astrometric measurements of the positions of the stars around a black hole are obviously subject to light bending, which shifts the observed light outwards from the black hole. There is a number of expectations related to gravitational lensing by Sgr A*. The apparent density of background stars should decrease around the black hole [112]. The orbits of stars and the velocity distribution should be distorted [113]. Extremely dim negative parity images should appear on the opposite side of the stars with respect to the black hole [95, 97, 114]. These will be probably detectable by next generation instruments, such as the ELT [115]. However, the most accessible effect of light bending remains the astrometric shift of the primary image, which should be within reach of GRAVITY for a number of S-stars [116]. The deflection is generally too weak for known stars to bear any memory of the spin of the black hole [116, 117]. Other GR effects such as the relativistic precession or time delay tend to dominate [118] and return more information on the characteristics of the black hole, including its angular momentum [119]. Grould et al. [118] investigated the detection by GRAVITY of different relativistic effects affecting the astrometric and/or spectroscopic observations of S2 such as the transverse Doppler shift, the gravitational redshift, the pericenter advance and higher-order general relativistic (GR) effects, in particular the Lense-Thirring effect due to the angular momentum of the black hole.

Nevertheless, even a very weak distortion of the orbits of S-stars introduces systematic errors in the determination of the orbital parameters if the astrometric shift is neglected. This error needs to be correctly quantified and compared to statistical uncertainties. The purpose of the present chapter is to assess the level of systematics induced by gravitational lensing in the orbits of three short period S-stars (S2, S38, S55). This is achieved by forcing an orbital fit without lensing to reproduce the orbit including lensing and evaluating the shift in the parameters. As expected, we find that the systematic error is below current uncertainties but not so far. After that, with the same

spirit of similar studies [119], by varying the semimajor axis and the orbital inclination of the star S2, we determine the region of the orbital parameters in which a similar star would show evidence of gravitational lensing beyond statistical noise.

In Section 3.2 we present a description of the instrument, Section 3.3 introduces the three stars investigated in our study and their orbits. Section 3.4 discusses gravitational lensing by Sgr A*. Section 3.5 evaluates the impact of gravitational lensing on the aforementioned stars. Section 3.6 repeats the same study on a clone of star S2 with different semimajor axis and inclination. Section 3.7 contains the discussion.

3.2 The GRAVITY Instrument

The European Southern Observatory (ESO) on Cerro Paranal in the Atacama Desert of Northern Chile, shown in Fig.3.1,



Figure 3.1: The four UTs and the four ATs. Source: eso.org.

is the observing site for optical astronomy. It hosts ten telescopes: two of them (VST (VLT Survey Telescope) and VISTA) are used for survey observations, the other eight are two quadruplets of telescopes forming the VLTI (Very Large Telescope Interferometer) when they do operate simultaneously, while operated individually they are called Very Large Telescope (VLT). The VLTI combines the light of the four VLT telescopes (the four Unit Telescopes (UTs)) and the Auxiliary Telescopes (ATs). The four UTs have a primary mirror of 8.2 m diameter assisted by both active and adaptive optics with a laser guide star if needed. When they do operate simultaneously they form an optical interferometer with a maximum baseline of 130 m used to study sources up to apparent magnitude in the K -band $m_K = 19$, such as the GC, AGNs, exoplanets or young stellar objects.

The four ATs are a set of telescopes with a primary mirror of 1.8 m and they can be only operated in the interferometric mode with a maximum baseline available of 200 m for targets up to $m_K = 16.5$.

For the UTs part of the collected light is sent to a curvature wavefront sensor which corrects the atmospheric aberration due to the atmospheric turbulence by acting over a deformable mirror in real time. For the ATs, the interferometer is used during nights with an excellent quality of the sky [120].

GRAVITY provides a spectro-interferometry in the K-band between 2 and 2.4 μm and a resolution between 4 mas (milli-arcsecond) and 50 mas with the UTs, and between 2 mas and 140 mas with the ATs. The project was accepted by ESO after concluding a study period finished in 2007 [107] and the commissioning phase started at the end of 2015 for the ATs and in 2016 for the UTs. GRAVITY observed Sgr A* for 6 months in 2019 in order to detect the weakest objects closer to it and follow their movement across the sky.

A scheme of the GRAVITY instrument can be seen in Fig. 3.2 [110]

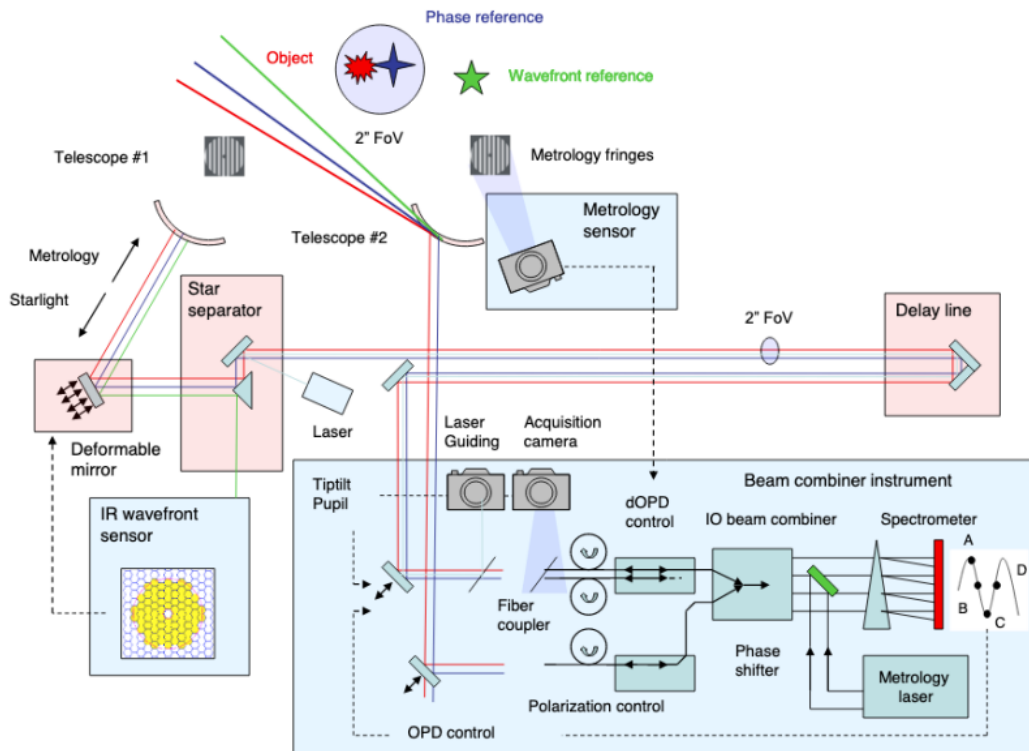


Figure 3.2: Diagram of GRAVITY subsystems. Source: Gravity Collaboration et al.[110].

where only two telescopes and one of the wavefront sensors and beam combiner are shown. For a complete description of the instrument, which is not part of the plan of this thesis, we refer to the references cited above in this Section.

Osculating Orbital Parameters				
Parameter	Unit	S2	S38	S55
a	mas	124.95 ± 0.04	142.54 ± 0.04	104.40 ± 0.05
e		0.88441 ± 0.00006	0.81451 ± 0.00015	0.72669 ± 0.00020
i	$^\circ$	134.70 ± 0.03	166.65 ± 0.4	158.52 ± 0.22
ω	$^\circ$	66.25 ± 0.03	27.17 ± 1.02	322.78 ± 1.13
Ω	$^\circ$	228.19 ± 0.03	109.45 ± 1	314.94 ± 1.14
T_0	Years	2018.38 ± 0.00	2003.15 ± 0.01	2021.69 ± 0.01
P	Years	16.046 ± 0.001	19.55 ± 0.01	12.25 ± 0.01

Table 3.1: S2, S38 and S35 osculating orbital parameters from Gravity Collaboration’s fit [111, 127].

Parameter	Unit	Value
M_{BH}	$10^6 M_\odot$	4.261 ± 0.01
D_\bullet	pc	8246.7 ± 9.3

Table 3.2: The black hole mass and the derived distance of the Solar System to the Galactic Center. [111, 127].

3.3 The stars S2, S38 and S55

The S-stars present a variety of orbital parameters, according to an isotropic distribution with projected density $\Sigma(\theta) \sim \theta^{-0.3}$ [121]. Many S-stars lie on very eccentric long-period orbits. The most favorable case for a full orbital reconstruction is provided by low-period stars, with $P \leq 20$ yrs, which are suitable for a long-term follow-up. The three stars discussed in this section fulfill this requirement.

S2 (or S02 in the UCLA nomenclature) is a single and slowly rotating main-sequence B-star of age $\simeq 6.6$ Myr, apparent magnitude $K = 14.1$ and estimated mass $M_{S2} \simeq 13.6 M_\odot$ [110, 111, 122–126]. S2 represents the only case in which a prograde orbital precession of 12 arcminutes has been measured. Therefore, here we refer to the osculating orbital parameters.

In Table 3.1 we display the current estimates of S2 orbital parameters as in Refs. [111, 127], where a is the semimajor axis of the ellipse, e its eccentricity, i is the angle of inclination between the real orbit and the observation plane, Ω is the angle of the ascending node measured from the north direction, ω is the argument of the pericenter, T_0 is the epoch of pericenter passage, P is the orbital period, M_{BH} the black hole mass, D_\bullet is the derived distance of the Solar System to the Galactic Center as shown in Table 3.2.

The relativistic precession changes the orbit orientation by increasing ω by 12’ per orbit. The

last apocenter passage was in 2010, the next one is expected in 2026, the furthest distance from the MBH is $r_{max} = 1954.24$ au according to Eq.(3.7), the last pericenter passage is $T_0 = 2018.38$ (May 19th 2018) [128, 129], the closest distance estimated according to Eq.(3.8) is $r_{min} = 119.87$ au and the next pericenter passage is expected to be in 2034.

S38 is a main-sequence B-star of apparent magnitude $K = 17$. In Table 3.1 we display the orbital parameters for S38 as in Ref. [111]. The last apocenter passage was at the end of 2012, the next one is expected in 2032, the furthest distance from the MBH is $r_{max} = 2146.66$ au according to Eq.(3.7), the last pericenter passage is $T_0 = 2003.15$, the closest distance estimated according to Eq.(3.8) is $r_{min} = 219.44$ au and the next pericenter passage is expected to be in 2022.

S55 is a main-sequence B-star of apparent magnitude $K = 17.5$. In Table 3.1 we display the orbital parameters for S55 as in Ref. [111]. The last apocenter passage was in 2015, the next one is expected in 2027, the furthest distance from the MBH is $r_{max} = 1496.17$ au according to Eq.(3.7), the last pericenter passage is $T_0 = 2021.69$, the closest distance estimated according to Eq.(3.8) is $r_{min} = 236.82$ au and the next pericenter passage is expected to be at the end of 2033.

For the orbit calculation of the S-stars, we start from the Lagrangian of a particle in the Schwarzschild metric

$$\mathcal{L} = \frac{1}{2}m \left[A(r)c^2\dot{t}^2 - A(r)^{-1}\dot{r}^2 - r^2\dot{\phi}^2 \right] \quad (3.1)$$

where m is the reduced mass of the star, ϕ is the true anomaly, r is the radial coordinate, t is the time for the observer at infinity and dots denote derivatives with respect to the proper time τ . The Schwarzschild metric is characterized by

$$A(r) = \left(1 - \frac{R_S}{r} \right) \quad (3.2)$$

where

$$R_S = \frac{2GM_{BH}}{c^2} \quad (3.3)$$

is the Schwarzschild radius, G is the gravitational constant, c is the speed of light.

The equations of motion can be expressed in terms of the constants of motion E and L as

$$\dot{t} = \frac{E}{c^2 \left(1 - \frac{R_S}{r} \right)} \quad (3.4)$$

$$\dot{\phi} = \frac{L}{r^2} \quad (3.5)$$

$$\dot{r} = \pm \sqrt{\frac{E^2}{c^2} - \left(1 - \frac{R_S}{r} \right) \left(1 + \frac{L^2}{r^2} \right)} \quad (3.6)$$

where the negative solution is for the particle approaching the black hole, the positive solution is for the particle moving away from the black hole. E represents the energy and L is the angular momentum of the particle per unit mass which we can get by solving the system with Eq.(3.6) evaluated for $r = r_{max}$ and $r = r_{min}$, where

$$r_{max} = a(1 + e) \quad (3.7)$$

$$r_{min} = a(1 - e) \quad (3.8)$$

are the apocenter and the pericenter respectively as functions of the semimajor axis and the eccentricity.

The equation of motion is [130]:

$$\ddot{r} = -\frac{A(r)}{2} \left(\frac{dA(r)}{dr} \dot{t}^2 - \frac{1}{A(r)^2} \frac{dA(r)}{dr} \dot{r}^2 - 2r\dot{\phi}^2 \right). \quad (3.9)$$

We solve Eq.(3.9) for $r = r(\tau)$ numerically from the last pericenter passage T_0 starting from null velocity as initial conditions, Eq.(3.5) and Eq.(3.4) respectively give $\phi = \phi(\tau)$ and $t = t(\tau)$, then we invert the latter in order to have $\tau = \tau(t)$ to finally obtain $r = r(t)$ and $\phi = \phi(t)$ which give the position and the true anomaly as functions of the observer time. All these solutions are found numerically and their stability over several periods has been carefully checked. We have then evaluated the orbital precessions of our three stars by comparing the true anomaly at two consecutive pericenters, i.e. minima of r . For the relativistic precession of S2 we find $\delta\phi = \phi(P) - 2\pi = 12'.17$, in agreement with GRAVITY results [111]. For S38 we get $\delta\phi = \phi(P) - 2\pi = 6'.79$ and for S55 $\delta\phi = \phi(P) - 2\pi = 6'.46$.

Finally, the orientation of the orbits in space is described by the standard orbital elements i , Ω , ω . The detailed geometric transformation from $r(t)$ and $\phi(t)$ to the position in the sky described by $\Delta R.A.$ and $\Delta Dec.$ is reported in Subsection 3.3.1 for completeness.

The orbits of the three stars are shown in Fig. 3.3 as they appear on the observer sky.

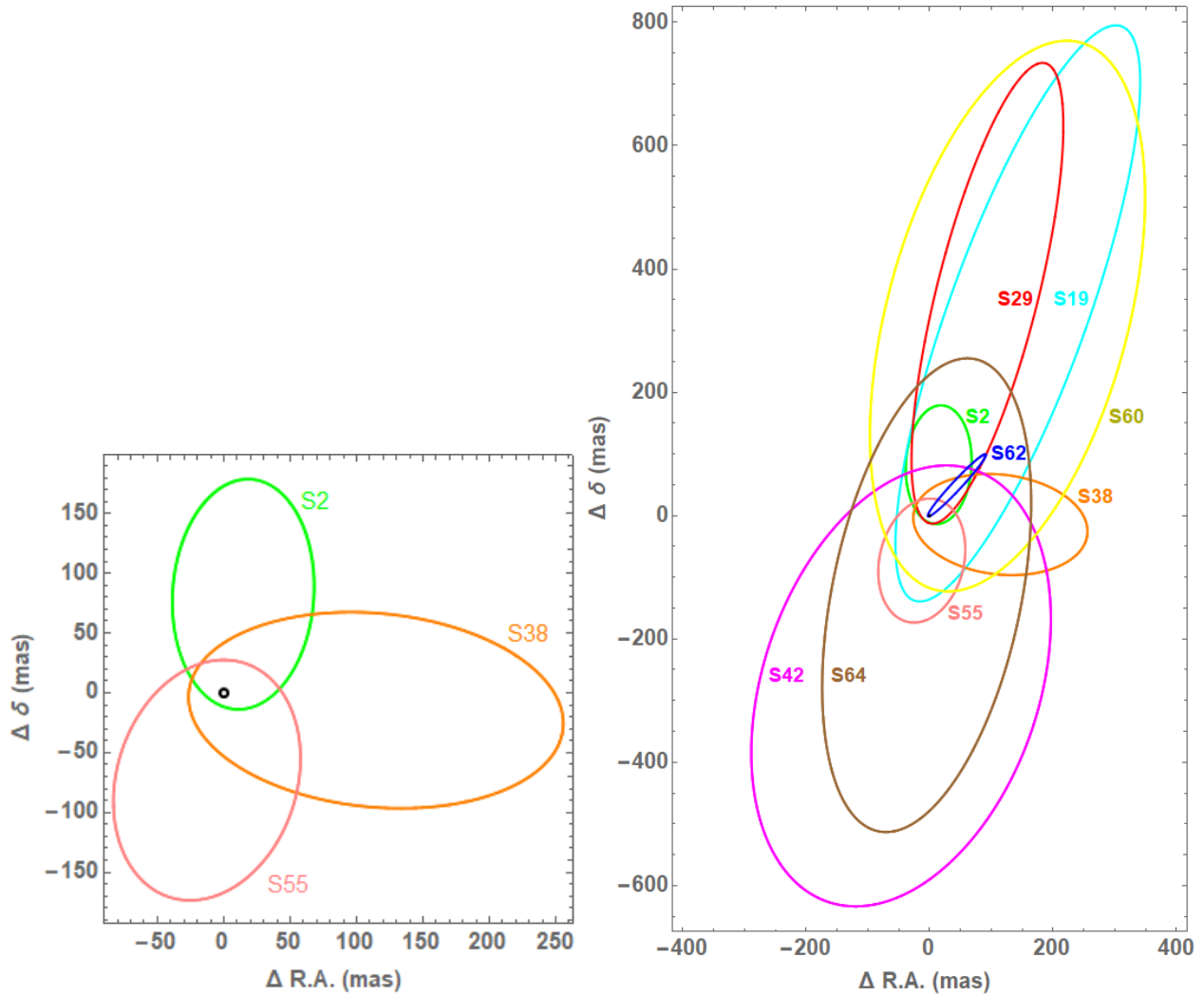


Figure 3.3: On the left: S2, S38 and S55 orbit reconstruction around Sgr A*; on the right: orbit reconstruction of other S-stars.

3.3.1 Orbital parameters of the real and apparent orbits

We deal with a two-body problem where S2 and the other S-stars have an elliptic orbit and Sgr A* lies in the focus located at the center of mass and we denote $OXYZ$ the coordinate system of the apparent orbit of the star: the axes origin is centered at Sgr A*. The Z-axis of the coordinate system is defined by the vector pointing from the Solar System to the Galactic Center, and the X and Y axes are defined such that the X-Y plane is parallel to the plane of the sky, with the X-axis pointing North and the Y-axis pointing East; we denote $Oxyz$ the plane of the real star's orbit.

In polar coordinates the ellipse equation in the $Oxyz$ system is given by

$$\begin{cases} x = r \cos \phi \\ y = r \sin \phi \\ z = 0 \end{cases} \quad (3.10)$$

where $r(\tau)$ is the star position that we get as a function of the proper time from Eq.(3.9) and, in our case, it coincides with D_{LS} , i.e. the distance between the lens (Sgr A*) and the source (the S-star); ϕ is the true anomaly that we get, as a function of the proper time $\phi(\tau)$, from Eq.(3.5), a is the semimajor axes of the ellipse and e its eccentricity.

We can always obtain the apparent orbit in the $OXYZ$ system by applying a matrix transformation on the $Oxyz$ system:

$$\begin{pmatrix} X \\ Y \\ Z \end{pmatrix} = R \begin{pmatrix} x \\ y \\ z \end{pmatrix} \quad (3.11)$$

where $R = R_\Omega \cdot R_i \cdot R_\omega$ is the rotation matrix where i is the angle of inclination between the real orbit and the observation plane, Ω is the angle of the ascending node, and ω is the argument of pericenter, and

$$R_\Omega(Z) = \begin{pmatrix} \cos \Omega & -\sin \Omega & 0 \\ \sin \Omega & \cos \Omega & 0 \\ 0 & 0 & 1 \end{pmatrix} \quad (3.12)$$

$$R_i(X) = \begin{pmatrix} 1 & 0 & 0 \\ 0 & \cos i & -\sin i \\ 0 & \sin i & \cos i \end{pmatrix} \quad (3.13)$$

$$R_\omega(Y) = \begin{pmatrix} \cos \omega & -\sin \omega & 0 \\ \sin \omega & \cos \omega & 0 \\ 0 & 0 & 1 \end{pmatrix} \quad (3.14)$$

where R_Ω represents the rotation along the Z-axes, R_i the rotation along the X-axes and R_ω is the rotation along the Y-axes. Then finally we get the Cartesian coordinates of the apparent orbit of the star on the sky plane,

$$\begin{cases} X = r[\cos \Omega \cos(\phi + \omega) - \sin \Omega \sin(\phi + \omega) \cos i] \\ Y = r[\sin \Omega \cos(\phi + \omega) + \cos \Omega \sin(\phi + \omega) \cos i] \\ Z = r[\sin(\phi + \omega) \sin i] \end{cases} \quad (3.15)$$

The observed displacement from Sgr A* are

$$\begin{cases} \Delta Dec. \equiv \frac{X}{D_\bullet} \\ \Delta R.A. \equiv \frac{Y}{D_\bullet} \end{cases} \quad (3.16)$$

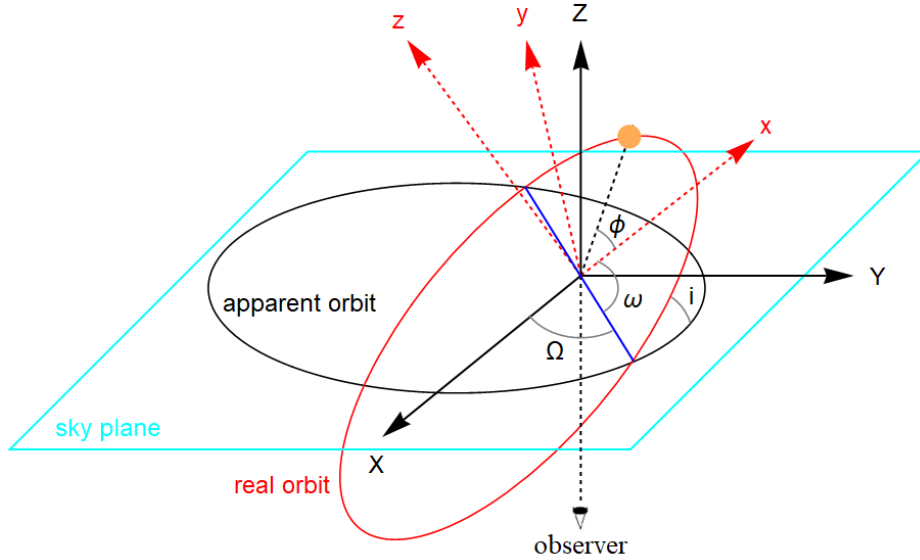


Figure 3.4: Projection on the sky of the real star's orbit onto the plane of the sky, the osculating orbital parameters are shown.

When we turn on the gravitational lensing effect, both coordinates are multiplied by $D_{\bullet}\theta/\sqrt{X^2 + Y^2}$ with θ given by Eq. (3.23).

3.4 Gravitational lensing by Sgr A*

The light from the S-stars is deviated by the gravitational field of Sgr A*. The deflection for the primary image can be generally studied in the weak deflection limit, unless the source is well-aligned behind it and is very close to it. However, this is precisely the situation in which gravitational lensing effects become appreciable. Therefore, we decide to keep the calculation of the deflection exact so as not to miss any potentially interesting effects. The source position is tracked by its radial coordinate $r_S \equiv r(t)$ as calculated from the orbital motion, and by the angle γ between the source position and the optical axis, defined as the line of sight from the observer to the black hole. In terms of the true anomaly and the orbital elements defined before, this angle is

$$\gamma(t) = \arccos [\sin (\phi(t) + \omega) \sin i] \quad (3.17)$$

and ranges from 0 (perfect alignment of the source behind the lens) to π (perfect anti-alignment, with the source in front of the lens).

A photon travelling from some radial coordinate r_1 to r_2 experiences an azimuthal shift

$$I(r_1, r_2; r_0) = \int_{r_1}^{r_2} \frac{dr}{r \sqrt{\frac{r^2}{r_0^2} \left(1 - \frac{R_S}{r_0}\right) - \left(1 - \frac{R_S}{r}\right)}}, \quad (3.18)$$

where r_0 is the closest approach distance of the null geodesic on which the photon is travelling. It is related to the impact parameter u of the asymptotic trajectory at infinity as

$$u = \frac{r_0}{\sqrt{1 - \frac{R_S}{r_0}}}. \quad (3.19)$$

For a photon emitted by a source at r_S and reaching an observer at distance D_\bullet , we have two possibilities: the photon may approach the black hole, reach the minimum distance r_0 and then travel toward the observer; otherwise, the photon may directly travel from r_S to the observer at D_\bullet without approaching the black hole. This is the case when the source is in front of the black hole as seen by the observer. Therefore, the azimuthal shift is

$$\Delta\phi(r_S, r_0) = \begin{cases} I(r_0, r_S; r_0) + I(r_0, D_\bullet; r_0) & \text{if } \gamma < \gamma_0 \\ I(r_S, D_\bullet; r_0) & \text{if } \gamma \geq \gamma_0 \end{cases} \quad (3.20)$$

The angle γ_0 , distinguishing the two cases, corresponds to the limiting case in which the photon is emitted with $r_0 = r_S$, i.e. when the photon is emitted at the closest approach point of its geodesic. For a given source distance r_S , the angle γ_0 is calculated by imposing

$$I(r_S, D_\bullet; r_S) = \pi - \gamma_0, \quad (3.21)$$

but is obviously very close to $\pi/2$ in all practical situations as shown in Fig.3.5.

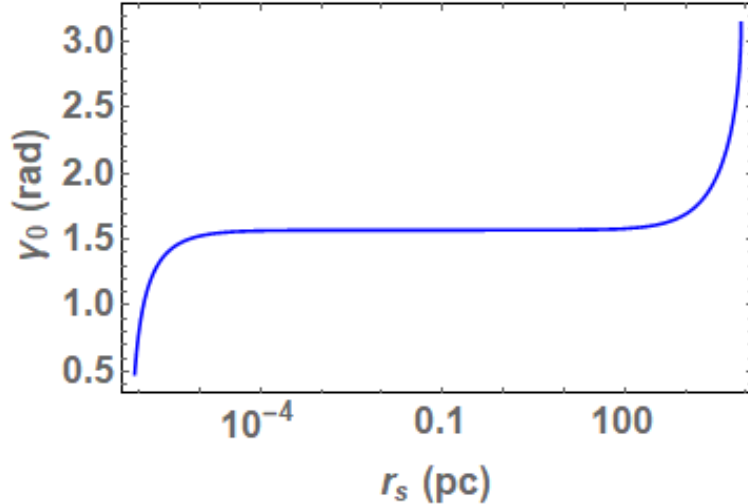


Figure 3.5: The angle γ_0 as a function of the source position r_S in a semi-log scale.

Only when the source is at a distance similar to the one of the observer, i.e. when $r_S = D_\bullet$, γ_0 grows and exceeds π . On the other extremum γ_0 negatively diverges when the source approaches the photon sphere at $1.5 R_S$ because photons will reach a far observer only if they are emitted in an outward direction.

Finally, by imposing that the azimuthal shift is just the correct one to let the photon move from γ to π (where the observer lies), we have a lens equation

$$\Delta\phi(r_S, r_0) = \pi - \gamma. \quad (3.22)$$

We solve numerically for the closest approach r_0 and find the corresponding impact parameter u . The angular distance of the image from the black hole as seen by the observer is then

$$\theta = \frac{u}{D_\bullet}, \quad (3.23)$$

since the observer distance D_\bullet is much larger than any u of our interest.

The star position including the astrometric shift is then obtained by increasing the angular coordinates $\Delta Dec.$ and $\Delta R.A.$ so that the angular distance from the black hole matches θ while keeping the position angle fixed. Note that the astrometric shift steadily increases from zero (when the source is in front of the black hole with $\gamma = \pi$) to the maximum value corresponding to the Einstein radius $\theta_E = \sqrt{2R_S r_S / D_\bullet(D_\bullet + r_S)}$, which is reached if the source is behind the black hole with $\gamma = 0$.

As already stated before, we neglect any lensing effects from the spin of the black hole following the findings of previous works [116, 117].

3.5 Impact of gravitational lensing on the reconstruction of the orbits of S- stars

The orbital fit of the S-stars is typically performed ignoring the astrometric shift due to gravitational lensing [118, 131]. However, forcing an orbital fit without including gravitational lensing may lead to a systematic error in the derived parameters. The most obvious one is the semimajor axis: since the astrometric shift pushes the observed images away from the black hole, the real semimajor axis should be slightly smaller than what we naively deduce from the observations. However, as we shall see, the 3-D reconstruction of the orbital parameters may lead to some combined effects on different correlated parameters.

In order to quantify this systematic error, we create simulated observations of the S-stars along their orbits including the astrometric shift due to gravitational lensing. These “data points” are generated from the tabulated orbital elements as reported by recent observations [127] and summarized in Table 3.1. We then try to fit these data points with orbits that do not include gravitational lensing. The new orbital elements will be slightly offset from the original ones and quantify the systematic error committed by ignoring gravitational lensing.

Since the offsets from the original parameters are very small, it is sufficient to perform a few iterations with the Gauss-Newton method to find the new minimum of the χ^2 [132]. In detail, denoting the 7 orbital elements with the vector

$$\boldsymbol{\eta} = (a, e, i, \omega, \Omega, T_0, P), \quad (3.24)$$

and the shift in the parameters with

$$\boldsymbol{\delta} = (\delta_a, \delta_e, \delta_i, \delta_\omega, \delta_\Omega, \delta_{T_0}, \delta_P), \quad (3.25)$$

we compare the positions including lensing $f_{lens,i}(\boldsymbol{\eta})$ and the positions without lensing $f_{0,i}(\boldsymbol{\eta})$. Here the index i spans the number of generated data points n , including both $\Delta Dec.$ and $\Delta R.A.$. Introducing the gradients

$$\mathbf{J}_i = \frac{\partial f_{0,i}(\boldsymbol{\eta})}{\partial \boldsymbol{\eta}} \quad (3.26)$$

the shifts are obtained by solving the linear equation

$$(\mathbf{J}^T \mathbf{J}) \boldsymbol{\delta} = \mathbf{J}^T [\mathbf{f}_{lens} - \mathbf{f}_0(\boldsymbol{\eta})] \quad (3.27)$$

where \mathbf{J} is the Jacobian matrix, whose i -th row equals \mathbf{J}_i , and where $\mathbf{f}_0(\boldsymbol{\eta})$ and \mathbf{f}_{lens} are vectors with i -th component $f_{0,i}$ and $f_{lens,i}$ respectively. The calculation of the offsets $\boldsymbol{\delta}$ can be iterated so as to minimize the χ^2

$$\chi^2 = \sum_{i=1}^n \left[\frac{f_{lens,i} - f_{0,i}(\boldsymbol{\eta} + \boldsymbol{\delta})}{\sigma_i} \right]^2, \quad (3.28)$$

where σ_i is the statistical uncertainty in each measurement. Here for simplicity we adopt a standard value of $\sigma = 0.4$ mas for the uncertainty of each individual measurement, as reported by GRAVITY [127]. A different value has no effect in the estimate of the systematic error calculated with our procedure, but is important to assess the relevance of systematic errors compared to statistical errors. In fact, the statistical uncertainty in each parameter scales as σ/\sqrt{n} .

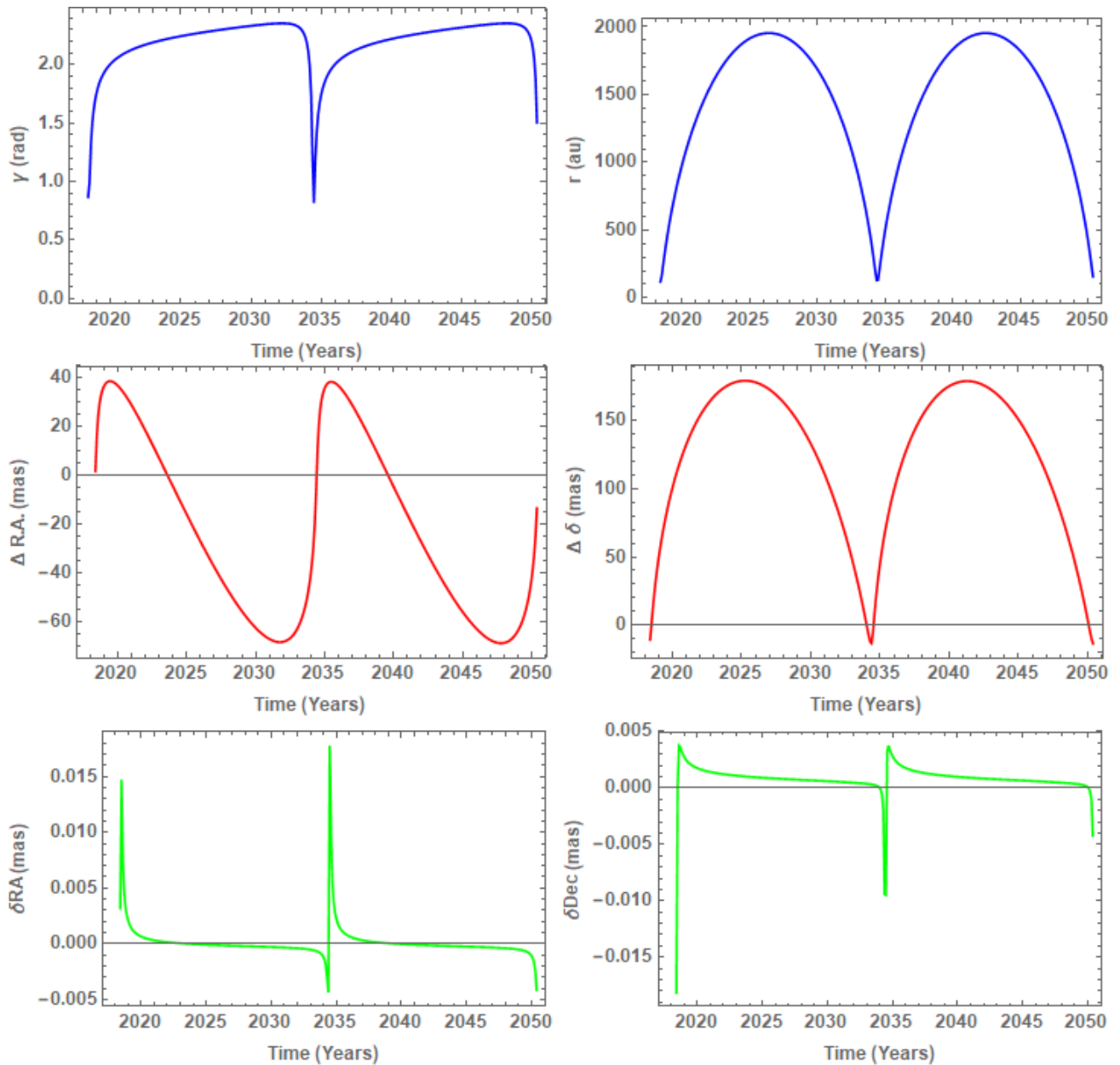


Figure 3.6: Analysis for S2. First row: $\gamma(t)$ (top left) and $r(t)$ (top right) as functions of time; second row: right ascension (on the left) and declination (on the right); last row: astrometric shifts in right ascension (left) and declination (on the right). Computations are done starting from T_0 over two periods.

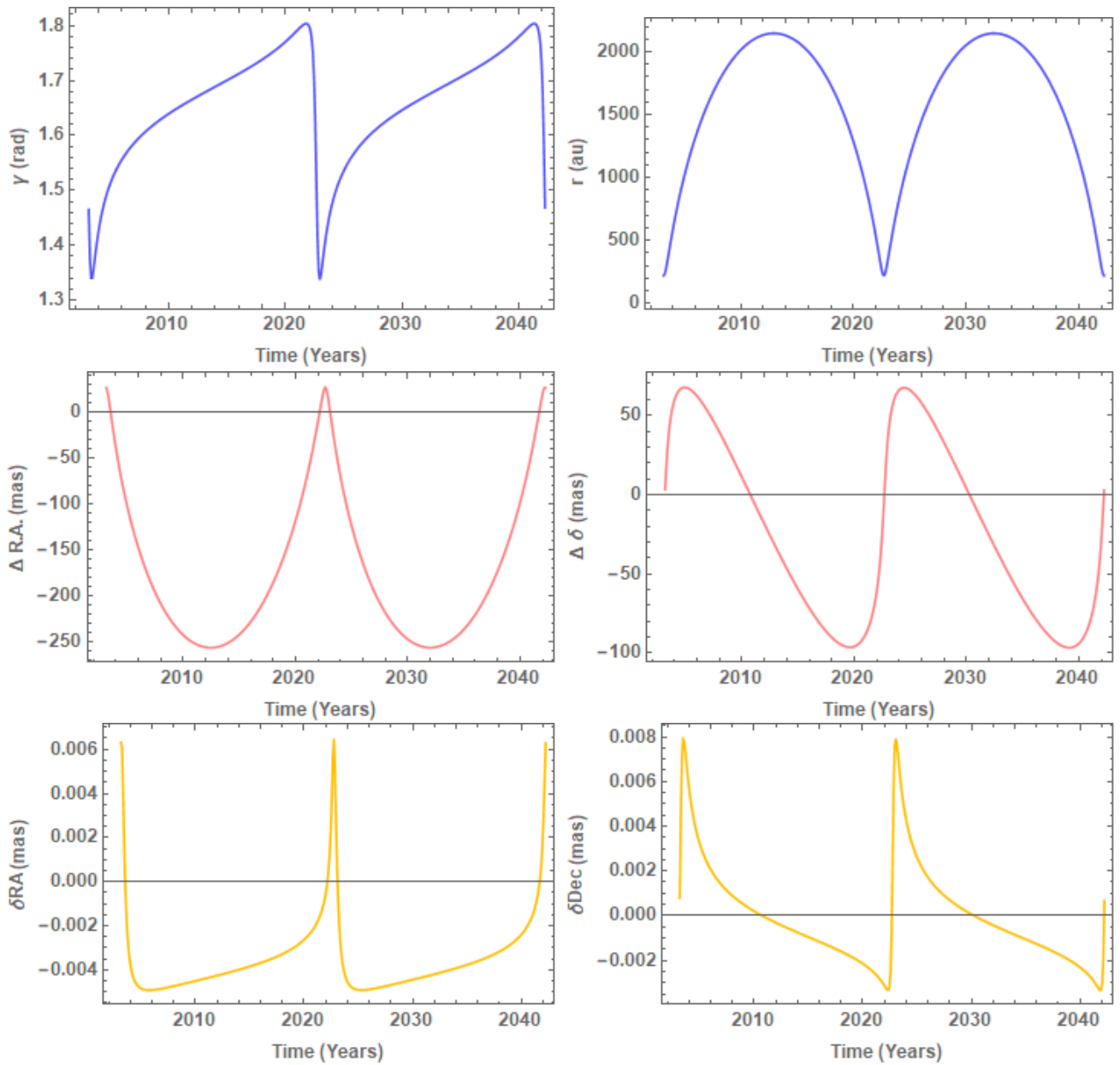


Figure 3.7: Analysis for S38. First row: $\gamma(t)$ (top left) and $r(t)$ (top right) as functions of time; second row: right ascension (on the left) and declination (on the right); last row: astrometric shifts in right ascension (left) and declination (on the right). Computations are done starting from T_0 over two periods.

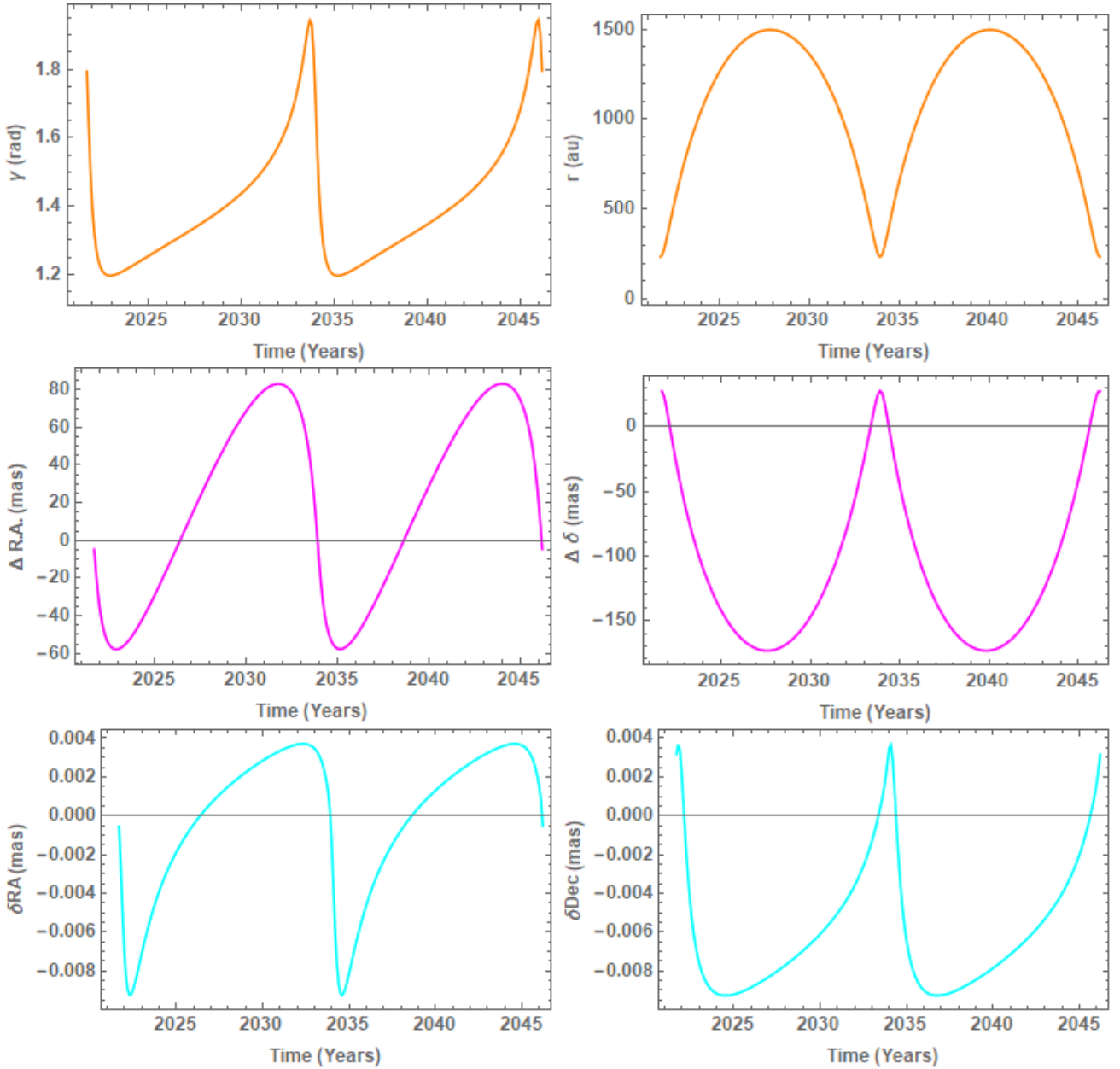


Figure 3.8: Analysis for S55. First row: $\gamma(t)$ (top left) and $r(t)$ (top right) as functions of time; second row: right ascension (on the left) and declination (on the right); last row: astrometric shifts in right ascension (left) and declination (on the right). Computations are done starting from T_0 over two periods.

Figs. 3.6, 3.7, 3.8 show the angular coordinates $\Delta R.A.$ and $\Delta Dec.$ as functions of time for the three stars S2, S38 and S55 respectively. In addition, we include plots of the alignment angle γ and the radial distance from the black hole r . These are the two quantities that determine the amount of the astrometric shift, which is finally reported in the bottom panels of each figure for both coordinates. We can appreciate that while the angular distances from the black hole are of the order of tens or hundred mas, the astrometric shifts are of the order of ten μas . Such small astrometric shifts are due to the fact that for all the three stars considered here, the alignment angle γ remains quite far from perfect alignment. For S2 we have $45^\circ < \gamma < 135^\circ$, for S38 $77^\circ < \gamma < 103^\circ$, for S55

$69^\circ < \gamma < 111^\circ$.

Table 3.3 contains the results of our investigation of the systematic shifts in the orbital parameters due to gravitational lensing compared with the statistical uncertainties as declared by GRAVITY. As expected, the estimates of the parameters are robust against gravitational lensing: all systematic errors are well below the uncertainties, but not too far! For S2 we see that for most parameters the shift is just one order of magnitude below the current uncertainty in the parameters. Even keeping the current astrometric accuracy for each individual data point, just by adding new observations in future years it will be possible to let the astrometric shift emerge and be detected. This is indeed an interesting perspective, since the astrometric shift provides another constraint on the enclosed mass that should be compatible with the dynamically derived mass. For S38 and S55 the situation is just slightly less favorable for lensing detection because the orbits are closer to face-on and the periastron is not as close as for S2. For these two stars, the most affected parameter remains the semimajor axis.

	S2		S38		S55	
Parameter	$\sigma(stat.)$	$\delta(syst.)$	$\sigma(stat.)$	$\delta(syst.)$	$\sigma(stat.)$	$\delta(syst.)$
a (mas)	4.0×10^{-2}	3.5×10^{-3}	4.0×10^{-2}	3.2×10^{-3}	5.0×10^{-2}	5.0×10^{-3}
e	6.0×10^{-5}	4.7×10^{-6}	1.5×10^{-4}	6.1×10^{-6}	2.0×10^{-4}	7.8×10^{-6}
i ($^\circ$)	3.0×10^{-2}	-1.2×10^{-3}	4.0×10^{-1}	3.9×10^{-3}	2.2×10^{-1}	4.6×10^{-3}
ω ($^\circ$)	3.0×10^{-2}	1.9×10^{-3}	1.0	2.9×10^{-3}	1.1	-1.3×10^{-2}
Ω ($^\circ$)	3.0×10^{-2}	1.9×10^{-3}	1.0	2.9×10^{-2}	1.1	-1.3×10^{-2}
P (years)	1.0×10^{-3}	-2.9×10^{-5}	1.0×10^{-2}	9.9×10^{-7}	1.0×10^{-2}	-5.3×10^{-6}

Table 3.3: Comparison between the systematic error δ committed by ignoring gravitational lensing and the statistical uncertainty σ reported by the GRAVITY Collaboration [111, 127] for S2, S38 and S55.

3.6 Exploring Gravitational lensing at various semimajor axes and inclinations

As shown in the previous section, the astrometric shifts of S2 and the other stars are about one order of magnitude smaller than the current uncertainties in the parameters. Indeed, their orbital inclinations keep the stars relatively far from perfect alignment. For stars getting closer to the black hole, the emitted light also experiences stronger deflections. Motivated by the interest in the detection of effects related to gravitational lensing, in this section we repeat the analysis for S2 after

varying the two parameters that have the strongest impact on gravitational lensing: the semimajor axis and the orbital inclination.

We start from the original value of the semimajor axis a reported in Table 3.1, and go down to $a \times 10^{-1.5} \approx 388 R_S$ in steps of $10^{-0.25}$ with a minimum periastron of $45 R_S$. The smallest value of a is safely far from the *tidal radius*, i.e. the maximal distance from the MBH where the tidal forces of the MBH would overwhelm the stellar self-gravity and tear the star apart [133]:

$$R_T = R_{S2} \left(\frac{M_{BH}}{M_{S2}} \right)^{1/3} \approx 31 R_S \quad (3.29)$$

where we have adopted $R_{S2} = 8.4 R_\odot$ for a normal main sequence star with $M = M_{S2}$ [134].

For each of the six semimajor axes in the described range, we also vary the inclination angle i in the range $90.5^\circ < i < 135^\circ$ in steps of 5° , so as to investigate the effects on the parameter shifts from the S2 inclination $i = 134.7^\circ$ to an edge-on orbit.

In our simulated observations, we keep the number of data points fixed and span two full orbits starting from T_0 with a total of 107 data points. Obviously, if the semimajor axis changes, the orbital period changes according to the third Kepler's law.

In Fig.3.9 we show how the S2 orbit changes as the semimajor axis becomes smaller keeping the inclination fixed at the real value. We compare the orbit including the lensing shift (green line) with the orbit without gravitational lensing (red line). The circle marks the position where Sgr A* is located. The orbit is traced over two periods starting from T_0 and it does not close due to the relativistic precession. The scale of the figures follows the same factor as the semimajor axis, so as to show the orbits always with the same size. We may note that the green line perfectly overlaps the red line, meaning that the astrometric shift is smaller than the thickness of the lines, save for the last figure in the bottom right, where we can barely appreciate a difference between the green line (including lensing) passing out of the red line (orbit with no lensing). In particular, the effect is visible at the periastron passage in the last panel.

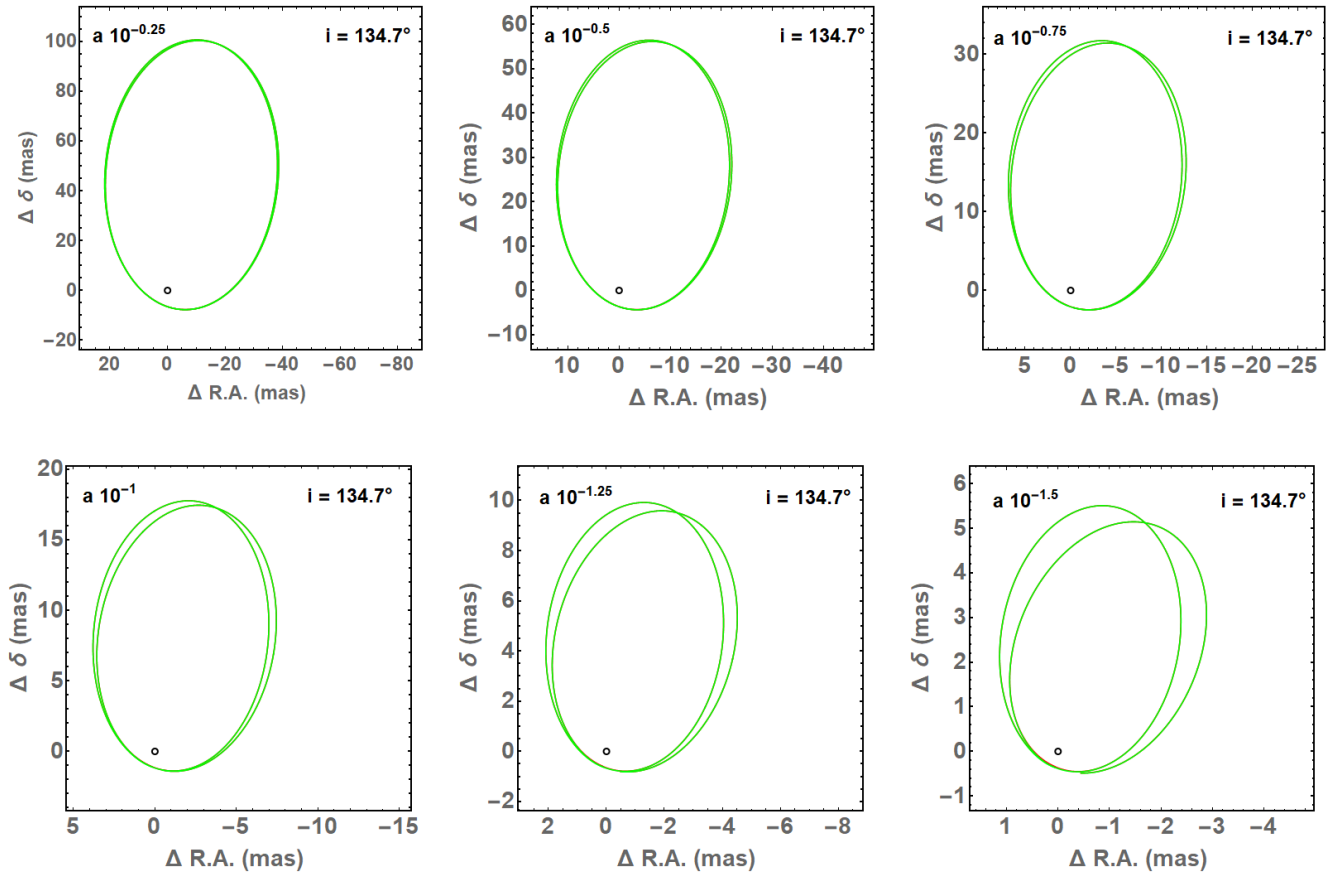


Figure 3.9: S2 orbit with its original fixed inclination $i = 134.7^\circ$ by varying its semimajor axis from $a \times 10^{-0.25}$ (first row, top left) to $a \times 10^{-1.5}$ (second row, bottom right). The red line stands for the unperturbed orbit, which is almost completely hidden behind the green line standing for the orbit affected by gravitational lensing. The circle stands for the position of Sgr A*. The orbit is traced over two periods starting from T_0 and it does not close due to the relativistic precession.

In Fig.3.10 we show the orbits of S2 with a fixed reduced semimajor axis by a factor of $10^{-1.5}$ and with a varying orbital inclination from $i = 90.5^\circ$ (first row, top left) to $i = 130^\circ$ (second row, bottom right) in steps of 5° . With the smallest semimajor axis, the effect of gravitational lensing is evident in all plots. In particular, nearly edge-on orbits show the typical circular section as the image rapidly revolves around the Einstein ring [113].

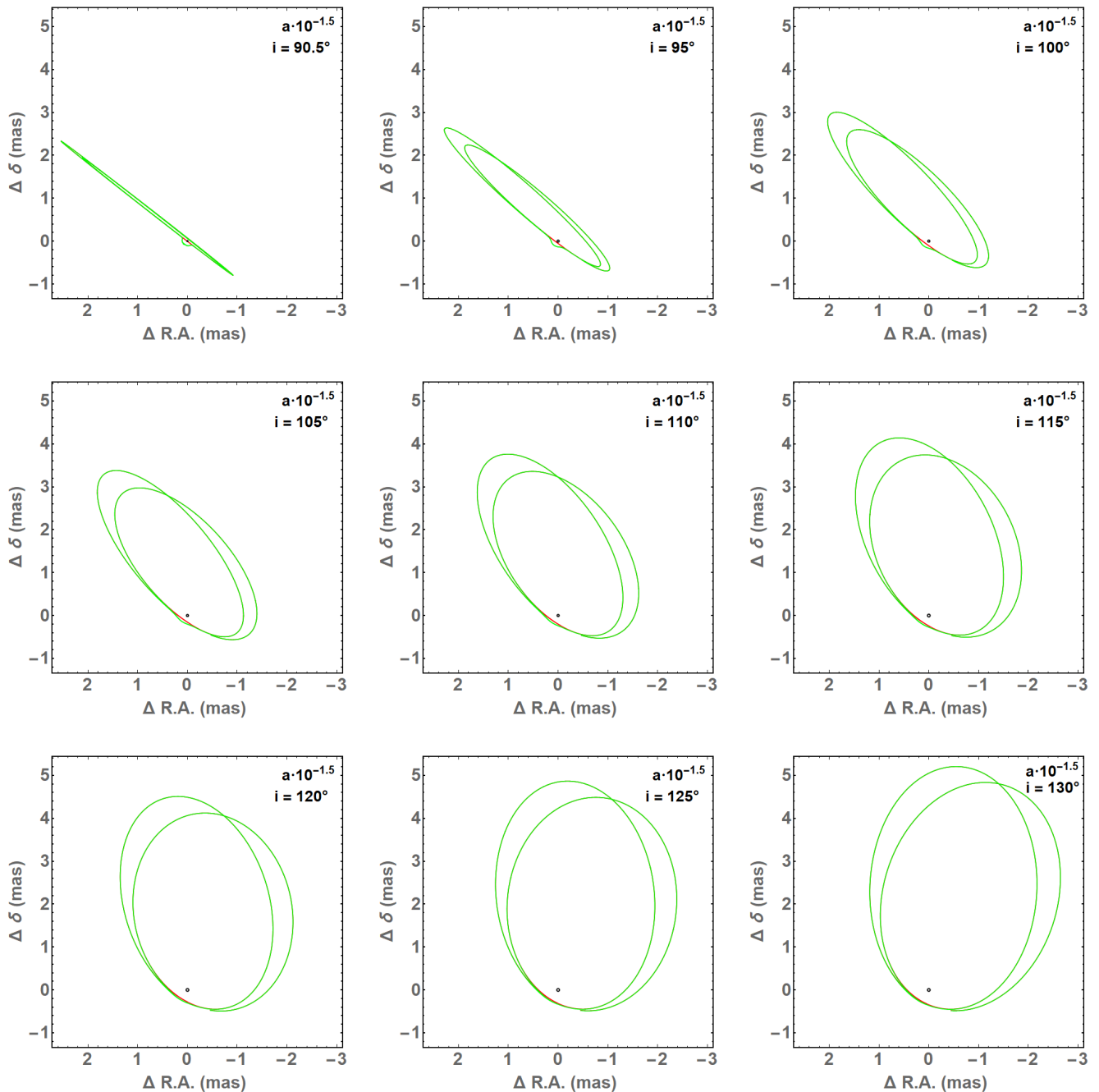


Figure 3.10: S2 orbit with a fixed reduced semimajor axis by a factor of $10^{-1.5}$ by varying its inclination from $i = 90.5^\circ$ (left top) to $i = 130^\circ$ (right bottom) in steps of 5° . The red line stands for the unperturbed orbit, the green line stands for the orbit affected by gravitational lensing. The circle stands for the position of Sgr A*. The orbit is traced over two periods starting from T_0 and it does not close due to the relativistic precession.

Finally, Fig. 3.11 shows the systematic shift δ in each orbital element due to gravitational lensing for all values of the semimajor axis in our range and for the different inclinations. The maximum semimajor axis corresponds to the actual measured value of S2. Therefore, the gray lines in each plot, which correspond to an inclination of 135° , match the values reported in Table 3.3 at their right ends.

First we note that the shifts in the semimajor axis and the eccentricity are very sensitive to the orbital inclination. For edge-on inclinations, the shifts rapidly approach the current uncertainty in the parameters. If we also decrease the semimajor axis, the shifts exceed the uncertainties. It may look quite counter-intuitive that the shift in the semimajor axis and the eccentricity decreases and even changes sign for closer stars, but we should be aware that the circular deviation of the star image around the Einstein ring cannot be fit by an unlensed orbital trajectory in any effective way. In these cases, the quality of the fit is rapidly degraded and the orbital elements become less and less reliable.

For the angular orbital elements, there is no particular evolution when we go to smaller semimajor axes. For the inclination we note that we start with a negative shift (toward a more edge-on orbit) and we end with a positive shift (more face-on orbit) when the deviation is closer to the Einstein ring. This inversion looks coherent with the plots for the semimajor axis and the eccentricity. A similar effect, but less pronounced, is in the argument of the periastron ω . The shift in the longitude of the ascending node Ω just increases very slowly.

The negative shift in the period can be interpreted as a combination of the increase in a and the need to follow the relativistic precession: a larger a with the same relativistic precession can only be obtained with a slightly larger mass of the black hole and a slightly shorter period.

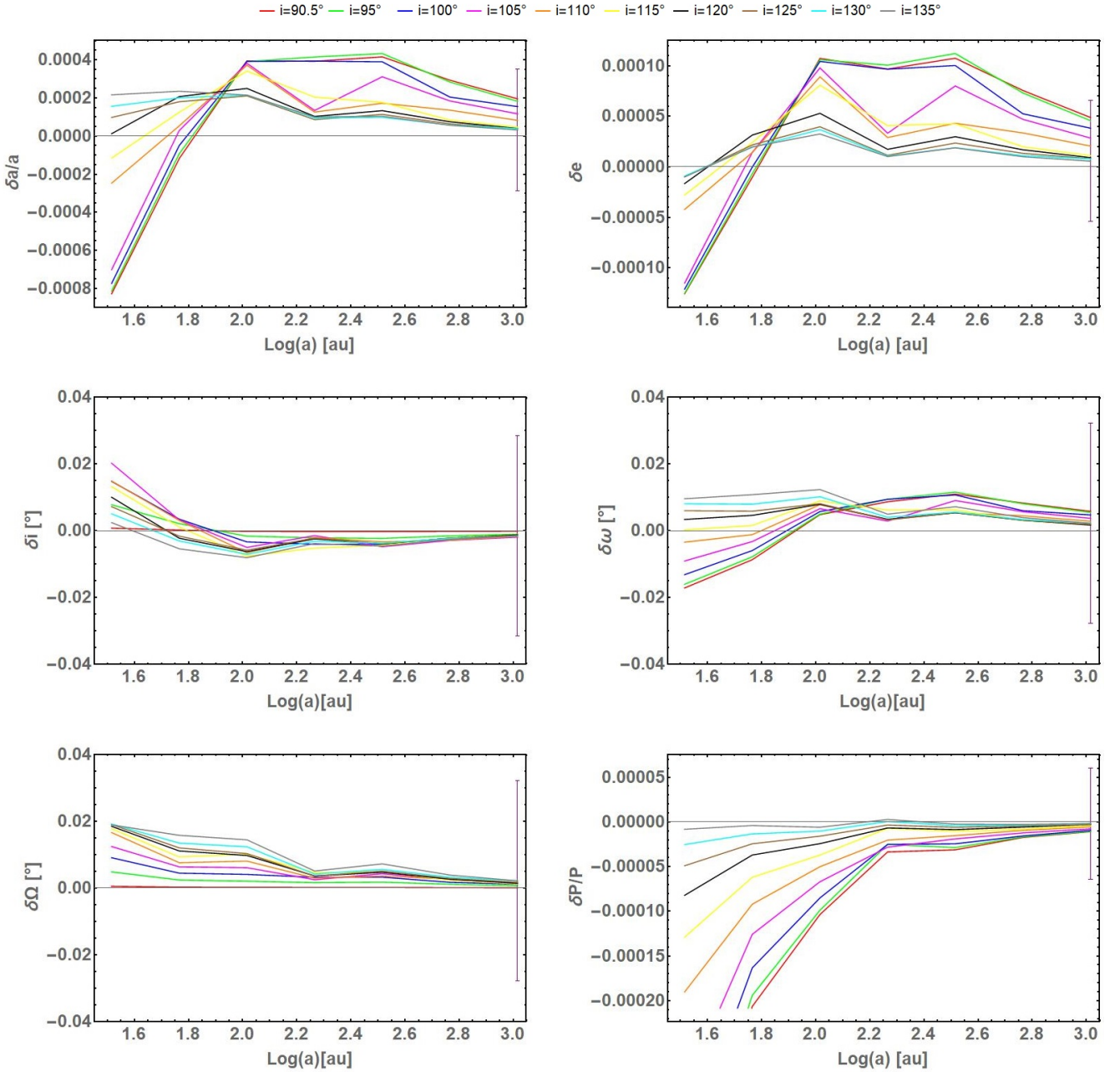


Figure 3.11: The δ obtained by varying the semimajor axis a and the inclination i . From top left to the sixth panel: δ_a/a , δ_e , δ_i , δ_ω , δ_Ω , δ_P/P as a function of $\log a$ expressed in au. The error bars on the right indicate GRAVITY's fit error, see Table 3.1.

Once more we stress the fact that the systematic shifts presented in Fig. 3.11 are independent of the statistical uncertainties. The minimum of the χ^2 does not change if we multiply or divide all σ_i by the same factor. Therefore, the significance of the parameter shifts caused by gravitational lensing can be evaluated once a given floor for the statistical noise is assigned. In this respect, Fig. 3.12 may be of some help. It represents the change in χ^2 induced by the lensing effects investigated in this section. The χ^2 depends on the uncertainty σ_i of the individual measurements and on the total number of data points. In Fig. 3.12 we have adopted $\sigma_i = \sigma \left(\frac{a}{a_{act}} \right)$, where $\sigma = 0.4$ mas is the average uncertainty of each individual measurement reported by GRAVITY [127], a_{act} is the actual

semimajor axis as we read it in Table 3.1 and a is the rescaled semimajor axis used in the plots of Fig. 3.11. In this way, the error bars of each astrometric measurement is rescaled with the same factor as the semimajor axis, which is a reasonable choice for simulated observations in which we assume to be sensitive to smaller and smaller values of a . The number of data points in our simulations is fixed to 107. Increasing the data would make the lensing signal emerge by increasing the χ^2 . This is particularly true if we add data points in the most sensitive sections of the orbit, when the star is better aligned with the black hole (minima of γ) and the distance is smaller.

With the basic setup discussed in this section, we see that the χ^2 is very modestly increased until we decrease the semimajor axis by an order of magnitude. Only at this point the χ^2 increases by more than one unit. Actually, we already have thousands of astrometric measurements on S2, which make the detection of lensing effects much closer than what may appear from Fig. 3.12.

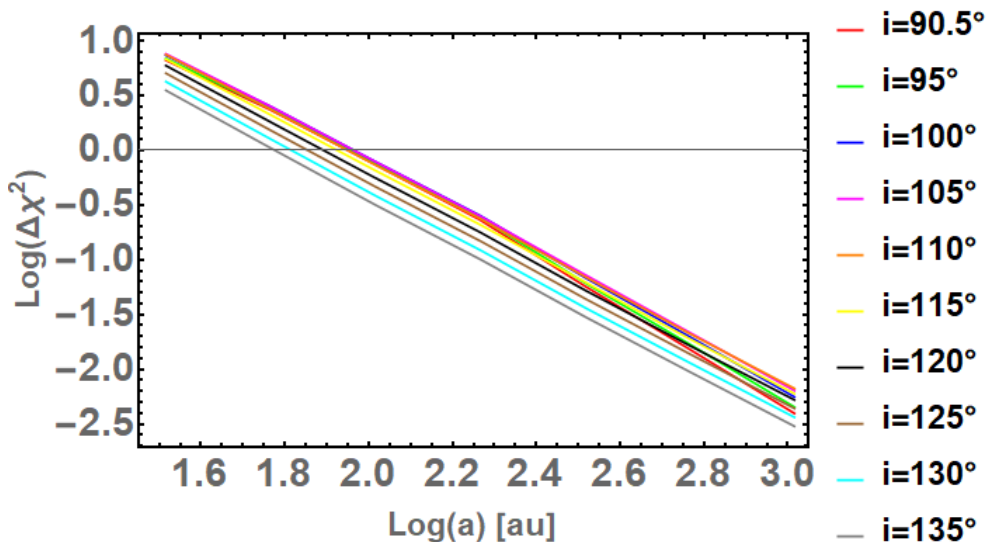


Figure 3.12: The χ^2 test of all data sets vs $\log a$ expressed in au.

3.7 Discussion

The presence of a MBH at the center of our Galaxy has inspired many studies about light deflection from such a mass concentration surrounded by a very dense stellar environment. Many relativistic effects have already been measured, such as the gravitational redshift, the Shapiro time delay and the relativistic precession of the periape [111]. This is indeed happened thanks to the existence of the star S2, which provides an ideal laboratory for testing relativistic dynamics in such strong fields. In contrast with these outstanding measurements, the long sought light deflection effect is surprisingly still hidden within the current astrometric error bars. The only manifestation of light deflection by Sgr A* currently known is through the reconstruction of the image of the shadow by the EHT collaboration [135]. In that case, mm-band observations by different stations are combined

so as to sample the interferometric visibility amplitude across several spatial frequencies. In this way, the best image including a model of the accretion flow and light deflection by the black hole metric can be selected based on the measured amplitudes. The source of the radiation detected in this band is the matter accreting onto the black hole, whose flow is modeled by sophisticated gravito-magnetic relativistic hydrodynamics simulations. Light deflection in these images is therefore only one of the many essential ingredients but cannot be studied in a clean isolated framework as it would be possible for a point source.

On the other hand, stars are ideal compact sources for probing gravitational lensing. Their emission peaks in the visible or in the NIR, which makes GRAVITY the ideal instrument. In this chapter, we have investigated the impact of gravitational lensing in current orbital fits for S2, S38 and S55. By forcing a fit ignoring lensing on the apparent orbit including the lensing effect, we estimate that the systematic shift in the orbital elements is about one tenth of the reported uncertainties. Therefore, we recommend the inclusion of the astrometric deflection of the image of S2 and other stars in the reconstruction of the orbits already at the present stage. Furthermore, by a continuous follow-up of the orbits of these stars, the light deflection should be detectable even at the current astrometric precision. Simple statistics would suggest that in order to bring down statistical errors at the same level of the systematic shift we should increase the sampling by a factor of 100. Yet, not all sections of the orbit have the same weight. The astrometric shift caused by gravitational lensing is more prominent when the star has the most favorable alignment behind the black hole. It would be ideal to concentrate the most accurate observations by NIR interferometers in this short section to have a clearer detection.

In addition to this analysis focusing on the actual orbits of the S-stars, we have presented an investigation of the systematic shift in the orbital elements after varying the semimajor axis and the orbital inclination of S2. For nearly edge-on orbits the shift in the parameters may increase by an order of magnitude. The effect becomes even more pronounced for stars orbiting closer and closer to the MBH.

The complete work is published on JCAP (Journal of Cosmology and Astroparticle Physics) and available at the following link <https://arxiv.org/abs/2207.14732>.

CHAPTER 4

CONCLUSIONS

The deflection of light has inspired many scientists starting from the XVIII century and in this thesis we showed two applications of gravitational lensing in fields of scientific interest, in the weak and in the strong regime.

We have generalized a previous study of binary lenses with $1/r^n$ potential with an extension to the case of mixed binaries which is a case important from the astrophysical point of view. This kind of investigation gave a complete atlas of the critical curves and caustics of mixed binary systems such as pairs of galaxies with different halos, or cases in which one object is made up of exotic matter and the other one is a normal star. The investigation in different limits in all three topology regimes have shown that an elliptic umbilic catastrophe exists for $mn < 1$ and it was also possible to describe the pseudocaustic in the $m = 0$ limit. We showed that these structures are quite sensitive to the parameters of the lens and that the mixed binary lens described here is still obtained by the linear superposition of the potentials of two isolated objects which is physically relevant whenever we can neglect the non-linear terms in Einstein equations.

The presence of a supermassive black hole at the center of the Milky Way inspired many studies about light deflection. This happened thanks to the existence of the star S2 and of the S-stars, which provide an ideal laboratory for testing General Relativity. Stars are ideal compact sources for probing gravitational lensing. Their emission peaks in the visible or in the NIR and makes GRAVITY the ideal instrument. The investigation of the impact of gravitational lensing in current orbital fits for S2, S38 and S55 by forcing a fit ignoring lensing on the apparent orbit including the lensing effect returns an estimation of the systematic shift in the orbital elements which is about one tenth of the reported uncertainties. The astrometric shift caused by gravitational lensing is more prominent when the star has the most favorable alignment behind the black hole. We have also presented an

investigation of the systematic shift in the orbital elements after varying the semimajor axis and the orbital inclination of S2 showing that for nearly edge-on orbits the shift in the parameters may increase by an order of magnitude and this effect becomes even more pronounced for stars orbiting closer and closer to the supermassive black hole.

More and more precise observations will allow the discovery of other S-stars around the Galactic Center which will be protagonist of future tests of General Relativity, whose results will indeed amaze us with striking confirmations or incredible surprises.

REFERENCES

- [1] M. Entwurf Einstein A.; Grossmann. *Entwurf einer verallgemeinerten Relativitätstheorie und eine Theorie der Gravitation*. Leipzig, Berlin: Teubner, 1913.
- [2] F. W. Dyson, A. S. Eddington, and C. Davidson. “A Determination of the Deflection of Light by the Sun’s Gravitational Field, from Observations Made at the Total Eclipse of May 29, 1919”. In: *Phil. Trans. Roy. Soc. Lond. A* 220 (1920), pp. 291–333. DOI: 10.1098/rsta.1920.0009.
- [3] S. L. Shapiro and S. A. Teukolsky. *Black holes, white dwarfs, and neutron stars: The physics of compact objects*. 1983.
- [4] Silvia Mollerach and Esteban Roulet. *Gravitational Lensing and Microlensing*. WORLD SCIENTIFIC, 2002. DOI: 10.1142/4890. eprint: <https://www.worldscientific.com/doi/pdf/10.1142/4890>. URL: <https://www.worldscientific.com/doi/abs/10.1142/4890>.
- [5] H. J. Witt. “Investigation of high amplification events in light curves of gravitationally lensed quasars.” In: *Astronomy and Astrophysics* 236 (Sept. 1990), p. 311.
- [6] B. Scott Gaudi. “Microlensing Surveys for Exoplanets”. In: *Annual Review of Astron and Astrophys* 50 (Sept. 2012), pp. 411–453. DOI: 10.1146/annurev-astro-081811-125518.
- [7] Hiroko Niikura et al. “Microlensing constraints on primordial black holes with Subaru/HSC Andromeda observations”. In: *Nature Astron.* 3.6 (2019), pp. 524–534. DOI: 10.1038/s41550-019-0723-1. arXiv: 1701.02151 [astro-ph.CO].
- [8] Raphael Gavazzi et al. “The Sloan Lens ACS Survey. 4. The mass density profile of early-type galaxies out to 100 effective radii”. In: *Astrophys. J.* 667 (2007), pp. 176–190. DOI: 10.1086/519237. arXiv: astro-ph/0701589.

-
- [9] Henk Hoekstra and Bhuvnesh Jain. “Weak Gravitational Lensing and its Cosmological Applications”. In: *Ann. Rev. Nucl. Part. Sci.* 58 (2008), pp. 99–123. DOI: 10.1146/annurev.nucl.58.110707.171151. arXiv: 0805.0139 [astro-ph].
- [10] Henk Hoekstra et al. “Masses of galaxy clusters from gravitational lensing”. In: *Space Sci. Rev.* 177 (2013), pp. 75–118. DOI: 10.1007/s11214-013-9978-5. arXiv: 1303.3274 [astro-ph.CO].
- [11] Martin Kilbinger. “Cosmology with cosmic shear observations: a review”. In: *Rept. Prog. Phys.* 78 (2015), p. 086901. DOI: 10.1088/0034-4885/78/8/086901. arXiv: 1411.0115 [astro-ph.CO].
- [12] Donghui Jeong and Fabian Schmidt. “Large-Scale Structure Observables in General Relativity”. In: *Class. Quant. Grav.* 32.4 (2015), p. 044001. DOI: 10.1088/0264-9381/32/4/044001. arXiv: 1407.7979 [astro-ph.CO].
- [13] Peter Schneider, Jürgen Ehlers, and Emilio E. Falco. *Gravitational Lenses*. 1992. DOI: 10.1007/978-3-662-03758-4.
- [14] Arlie O. Petters, Harold Levine, and Joachim Wambsganss. *Singularity theory and gravitational lensing*. 2001.
- [15] V. Perlick. “Gravitational lensing from a spacetime perspective”. In: *Living Rev. Rel.* 7 (2004), p. 9.
- [16] *Gravitational Lensing: Strong, Weak and Micro*. Jan. 2006. arXiv: astro-ph/0407232 [astro-ph].
- [17] Alexander Zakharov. “Lensing by exotic objects”. In: *General Relativity and Gravitation* 42.9 (Sept. 2010), pp. 2301–2322. DOI: 10.1007/s10714-010-1021-5.
- [18] Valerio Bozza. “Gravitational lensing by black holes”. In: *General Relativity and Gravitation* 42.9 (Sept. 2010), pp. 2269–2300. DOI: 10.1007/s10714-010-0988-2. arXiv: 0911.2187 [gr-qc].
- [19] S. W. Kim and Y. M. Cho. “Wormhole gravitational lens.” In: *Evolution of the Universe and its Observational Quest*. Jan. 1994, pp. 353–354.
- [20] John G. Cramer et al. “Natural wormholes as gravitational lenses”. In: *Physical Review D* 51.6 (Mar. 1995), pp. 3117–3120. DOI: 10.1103/PhysRevD.51.3117. arXiv: astro-ph/9409051 [astro-ph].
-

-
- [21] Margarita Safonova, Diego F. Torres, and Gustavo E. Romero. “Macrolensing Signatures of Large-Scale Violations of the Weak Energy Condition”. In: *Modern Physics Letters A* 16.3 (Jan. 2001), pp. 153–162. DOI: 10.1142/S0217732301003188. arXiv: astro-ph/0104075 [astro-ph].
- [22] Ernesto Eiroa, Gustavo E. Romero, and Diego F. Torres. “Chromaticity Effects in Microlensing by Wormholes”. In: *Modern Physics Letters A* 16.15 (Jan. 2001), pp. 973–983. DOI: 10.1142/S021773230100398X. arXiv: gr-qc/0104076 [gr-qc].
- [23] Margarita Safonova, Diego F. Torres, and Gustavo E. Romero. “Microlensing by natural wormholes: Theory and simulations”. In: *Phys. Rev. D* 65 (2002), p. 023001. DOI: 10.1103/PhysRevD.65.023001. arXiv: gr-qc/0105070.
- [24] Margarita Safonova and Diego F. Torres. “Degeneracy in exotic gravitational lensing”. In: *Mod. Phys. Lett. A* 17 (2002), pp. 1685–1692. DOI: 10.1142/S0217732302008083. arXiv: gr-qc/0208039.
- [25] Ryuichi Takahashi and Hideki Asada. “Observational Upper Bound on the Cosmic Abundances of Negative-mass Compact Objects and Ellis Wormholes from the Sloan Digital Sky Survey Quasar Lens Search”. In: *Astrophys. J. Lett.* 768 (2013), p. L16. DOI: 10.1088/2041-8205/768/1/L16. arXiv: 1303.1301 [astro-ph.CO].
- [26] F. Rahaman, M. Kalam, and S. Chakraborty. “Gravitational lensing by stable C-field wormhole”. In: *Chin. J. Phys.* 45 (2007), p. 518. arXiv: 0705.0740 [gr-qc].
- [27] Peter K. F. Kuhfittig. “Gravitational lensing of wormholes in noncommutative geometry”. In: (Jan. 2015). arXiv: 1501.06085 [gr-qc].
- [28] Juan Manuel Tejeiro S. and Eduard Alexis Larranaga R. “Gravitational lensing by wormholes”. In: *Romanian Journal of Physics* 57 (Jan. 2012), pp. 736–747.
- [29] Kamal K Nandi, Yuan-Zhong Zhang, and Alexander V Zakharov. “Gravitational lensing by wormholes”. In: *Physical Review D* 74.2 (2006), p. 024020.
- [30] Tushar Kanti Dey and Surajit Sen. “Gravitational lensing by wormholes”. In: *Mod. Phys. Lett. A* 23 (2008), pp. 953–962. DOI: 10.1142/S0217732308025498. arXiv: 0806.4059 [gr-qc].
- [31] H. G. Ellis. “Ether flow through a drainhole - a particle model in general relativity”. In: *J. Math. Phys.* 14 (1973), pp. 104–118. DOI: 10.1063/1.1666161.
- [32] K. A. Bronnikov. “Scalar-tensor theory and scalar charge”. In: *Acta Phys. Polon. B* 4 (1973), pp. 251–266.
-

- [33] M. S. Morris and K. S. Thorne. “Wormholes in space-time and their use for interstellar travel: A tool for teaching general relativity”. In: *Am. J. Phys.* 56 (1988), pp. 395–412. DOI: 10.1119/1.15620.
- [34] Michael S. Morris, Kip S. Thorne, and Ulvi Yurtsever. “Wormholes, Time Machines, and the Weak Energy Condition”. In: *Phys. Rev. Lett.* 61 (13 Sept. 1988), pp. 1446–1449. DOI: 10.1103/PhysRevLett.61.1446. URL: <https://link.aps.org/doi/10.1103/PhysRevLett.61.1446>.
- [35] Edward Teo. “Rotating traversable wormholes”. In: *Phys. Rev. D* 58 (1998), p. 024014. DOI: 10.1103/PhysRevD.58.024014. arXiv: gr-qc/9803098.
- [36] Kimet Jusufi and Ali Övgün. “Gravitational lensing by rotating wormholes”. In: *Phys. Rev. D* 97 (2 Jan. 2018), p. 024042. DOI: 10.1103/PhysRevD.97.024042. URL: <https://link.aps.org/doi/10.1103/PhysRevD.97.024042>.
- [37] Naoki Tsukamoto and Tomohiro Harada. “Light curves of light rays passing through a wormhole”. In: *Phys. Rev. D* 95.2 (2017), p. 024030. DOI: 10.1103/PhysRevD.95.024030. arXiv: 1607.01120 [gr-qc].
- [38] Takayuki Ohgami and Nobuyuki Sakai. “Wormhole shadows”. In: *Phys. Rev. D* 91 (12 June 2015), p. 124020. DOI: 10.1103/PhysRevD.91.124020. URL: <https://link.aps.org/doi/10.1103/PhysRevD.91.124020>.
- [39] Takayuki Ohgami and Nobuyuki Sakai. “Wormhole shadows in rotating dust”. In: *Phys. Rev. D* 94 (6 Sept. 2016), p. 064071. DOI: 10.1103/PhysRevD.94.064071. URL: <https://link.aps.org/doi/10.1103/PhysRevD.94.064071>.
- [40] L. Chetouani and G. Clement. “Geometrical optics in the Ellis geometry”. In: *General Relativity and Gravitation* 16.2 (Feb. 1984), pp. 111–119. DOI: 10.1007/BF00762440.
- [41] Volker Perlick. “Exact gravitational lens equation in spherically symmetric and static spacetimes”. In: *Phys. Rev. D* 69 (6 Mar. 2004), p. 064017. DOI: 10.1103/PhysRevD.69.064017. URL: <https://link.aps.org/doi/10.1103/PhysRevD.69.064017>.
- [42] F. Abe. “Gravitational Microlensing by the Ellis Wormhole”. In: *Astrophysical Journal* 725.1 (Dec. 2010), pp. 787–793. DOI: 10.1088/0004-637X/725/1/787. arXiv: 1009.6084 [astro-ph.CO].
- [43] Amrita Bhattacharya and Alexander A. Potapov. “Bending of light in Ellis wormhole geometry”. In: *Mod. Phys. Lett. A* 25 (2010), pp. 2399–2409. DOI: 10.1142/S0217732310033748.

-
- [44] Yukiharu Toki et al. “Astrometric Image Centroid Displacements due to Gravitational Microlensing by the Ellis Wormhole”. In: *Astrophysical Journal* 740.2, 121 (Oct. 2011), p. 121. DOI: 10.1088/0004-637X/740/2/121. arXiv: 1107.5374 [astro-ph.CO].
- [45] Naoki Tsukamoto, Tomohiro Harada, and Kohji Yajima. “Can we distinguish between black holes and wormholes by their Einstein ring systems?” In: *Phys. Rev. D* 86 (2012), p. 104062. DOI: 10.1103/PhysRevD.86.104062. arXiv: 1207.0047 [gr-qc].
- [46] Koki Nakajima and Hideki Asada. “Deflection angle of light in an Ellis wormhole geometry”. In: *Phys. Rev. D* 85 (10 May 2012), p. 107501. DOI: 10.1103/PhysRevD.85.107501. URL: <https://link.aps.org/doi/10.1103/PhysRevD.85.107501>.
- [47] G. W. Gibbons and M. Vyska. “The Application of Weierstrass elliptic functions to Schwarzschild Null Geodesics”. In: *Class. Quant. Grav.* 29 (2012), p. 065016. DOI: 10.1088/0264-9381/29/6/065016. arXiv: 1110.6508 [gr-qc].
- [48] Chul-Moon Yoo, Tomohiro Harada, and Naoki Tsukamoto. “Wave Effect in Gravitational Lensing by the Ellis Wormhole”. In: *Phys. Rev. D* 87 (2013), p. 084045. DOI: 10.1103/PhysRevD.87.084045. arXiv: 1302.7170 [gr-qc].
- [49] Takao Kitamura, Koki Nakajima, and Hideki Asada. “Demagnifying gravitational lenses toward hunting a clue of exotic matter and energy”. In: *Phys. Rev. D* 87 (2 Jan. 2013), p. 027501. DOI: 10.1103/PhysRevD.87.027501. URL: <https://link.aps.org/doi/10.1103/PhysRevD.87.027501>.
- [50] Koji Izumi et al. “Gravitational lensing shear by an exotic lens object with negative convergence or negative mass”. In: *Phys. Rev. D* 88 (2013), p. 024049. DOI: 10.1103/PhysRevD.88.024049. arXiv: 1305.5037 [gr-qc].
- [51] Naoki Tsukamoto et al. “Gravitational lensing in Tangherlini spacetime in the weak gravitational field and the strong gravitational field”. In: *Phys. Rev. D* 90.6 (2014), p. 064043. DOI: 10.1103/PhysRevD.90.064043. arXiv: 1402.6823 [gr-qc].
- [52] Koki Nakajima, Koji Izumi, and Hideki Asada. “Negative time delay of light by a gravitational concave lens”. In: *Phys. Rev. D* 90 (8 Oct. 2014), p. 084026. DOI: 10.1103/PhysRevD.90.084026. URL: <https://link.aps.org/doi/10.1103/PhysRevD.90.084026>.
- [53] Naoki Tsukamoto and Tomohiro Harada. “Signed magnification sums for general spherical lenses”. In: *Phys. Rev. D* 87 (2 Jan. 2013), p. 024024. DOI: 10.1103/PhysRevD.87.024024. URL: <https://link.aps.org/doi/10.1103/PhysRevD.87.024024>.
-

- [54] Takao Kitamura et al. “Microlensed image centroid motions by an exotic lens object with negative convergence or negative mass”. In: *Phys. Rev. D* 89 (8 Apr. 2014), p. 084020. DOI: 10.1103/PhysRevD.89.084020. URL: <https://link.aps.org/doi/10.1103/PhysRevD.89.084020>.
- [55] Valerio Bozza and Adriana Postiglione. “Alternatives to Schwarzschild in the weak field limit”. In: *14th Marcel Grossmann Meeting on Recent Developments in Theoretical and Experimental General Relativity, Astrophysics, and Relativistic Field Theories*. Vol. 4. 2017, pp. 3511–3514. DOI: 10.1142/9789813226609_0453.
- [56] G. S. Bisnovatyi-Kogan and O. Yu. Tsupko. “Gravitational lensing in a non-uniform plasma”. In: *Mon. Not. Roy. Astron. Soc.* 404 (2010), pp. 1790–1800. DOI: 10.1111/j.1365-2966.2010.16290.x. arXiv: 1006.2321 [astro-ph.CO].
- [57] Xinzhong Er and Adam Rogers. “Two families of astrophysical diverging lens models”. In: *Monthly Notices of the RAS* 475.1 (Mar. 2018), pp. 867–878. DOI: 10.1093/mnras/stx3290. arXiv: 1712.06900 [astro-ph.GA].
- [58] Adam Rogers and Xinzhong Er. “Dual-component plasma lens models”. In: *Monthly Notices of the RAS* 485.4 (June 2019), pp. 5800–5816. DOI: 10.1093/mnras/stz744. arXiv: 1903.06384 [astro-ph.GA].
- [59] Xinzhong Er and Adam Rogers. “Two families of elliptical plasma lenses”. In: *Monthly Notices of the RAS* 488.4 (Oct. 2019), pp. 5651–5664. DOI: 10.1093/mnras/stz2073. arXiv: 1907.10787 [astro-ph.GA].
- [60] Oleg Yu. Tsupko and Gennady S. Bisnovatyi-Kogan. “Hills and holes in the microlensing light curve due to plasma environment around gravitational lens”. In: *Mon. Not. Roy. Astron. Soc.* 491.4 (2020), pp. 5636–5649. DOI: 10.1093/mnras/stz3365. arXiv: 1910.03457 [gr-qc].
- [61] V. Bozza and C. Melchiorre. “Caustics of 1/rnbinary gravitational lenses: from galactic haloes to exotic matter”. In: *Journal of Cosmology and Astroparticle Physics* 2016.03 (Mar. 2016), 040–040. ISSN: 1475-7516. DOI: 10.1088/1475-7516/2016/03/040. URL: <http://dx.doi.org/10.1088/1475-7516/2016/03/040>.
- [62] Hideki Asada. “Gravitational lensing by exotic objects”. In: *Mod. Phys. Lett. A* 32.34 (2017), p. 1730031. DOI: 10.1142/S0217732317300312. arXiv: 1711.01730 [gr-qc].
- [63] Takayuki Ohgami and Nobuyuki Sakai. “Wormhole shadows”. In: *Phys. Rev. D* 91 (12 June 2015), p. 124020. DOI: 10.1103/PhysRevD.91.124020. URL: <https://link.aps.org/doi/10.1103/PhysRevD.91.124020>.

- [64] Event Horizon Telescope Collaboration et al. “First Sagittarius A* Event Horizon Telescope Results. VI. Testing the Black Hole Metric”. In: *The Astrophysical Journal Letters* 930.2, L17 (May 2022), p. L17. DOI: 10.3847/2041-8213/ac6756.
- [65] Naoki Tsukamoto and Takafumi Kokubu. “High energy particle collisions in static, spherically symmetric black-hole-like wormholes”. In: *Physical Review D* 101.4, 044030 (Feb. 2020), p. 044030. DOI: 10.1103/PhysRevD.101.044030. arXiv: 1912.07492 [gr-qc].
- [66] Thibault Damour and Sergey N. Solodukhin. “Wormholes as black hole foils”. In: *Phys. Rev. D* 76 (2007), p. 024016. DOI: 10.1103/PhysRevD.76.024016. arXiv: 0704.2667 [gr-qc].
- [67] E. M. Shin and N. W. Evans. “Lensing by binary galaxies modelled as isothermal spheres”. In: *Monthly Notices of the Royal Astronomical Society* 390.2 (Oct. 2008), pp. 505–522. ISSN: 0035-8711. DOI: 10.1111/j.1365-2966.2008.13738.x. eprint: <https://academic.oup.com/mnras/article-pdf/390/2/505/3423500/mnras0390-0505.pdf>. URL: <https://doi.org/10.1111/j.1365-2966.2008.13738.x>.
- [68] Israel Kovner. “The Quadrupole Gravitational Lens”. In: *Astrophysical Journal* 312 (Jan. 1987), p. 22. DOI: 10.1086/164846.
- [69] N. W. Evans and M. I. Wilkinson. “Lens models with density cusps”. In: *Monthly Notices of the RAS* 296.4 (June 1998), pp. 800–812. DOI: 10.1046/j.1365-8711.1998.01380.x.
- [70] Sun Hong Rhie. “Elliptically Symmetric Lenses and Violation of Burke’s Theorem”. In: *arXiv e-prints*, arXiv:1006.0782 (June 2010), arXiv:1006.0782. arXiv: 1006.0782 [astro-ph.EP].
- [71] Yun Wang and Edwin L. Turner. “Caustics, critical curves and cross-sections for gravitational lensing by disk galaxies”. In: *Mon. Not. Roy. Astron. Soc.* 292 (1997), p. 863. DOI: 10.1093/mnras/292.4.863. arXiv: astro-ph/9702078.
- [72] Nicolas Tessore and R. Benton Metcalf. “The elliptical power law profile lens”. In: *Astron. Astrophys.* 580 (2015), A79. DOI: 10.1051/0004-6361/201526773. arXiv: 1507.01819 [astro-ph.CO].
- [73] Ethan Lake and Zheng Zheng. “Gravitational lensing by ring-like structures”. In: *Monthly Notices of the RAS* 465.2 (Feb. 2017), pp. 2018–2032. DOI: 10.1093/mnras/stw2840. arXiv: 1601.03051 [astro-ph.EP].
- [74] Amir B. Aazami, Charles R. Keeton, and Arlie O. Petters. “Magnification Cross Sections for the Elliptic Umbilic Caustic Surface”. In: *Universe* 5 (2019), p. 161. DOI: 10.3390/universe5070161. arXiv: 1905.11974 [astro-ph.CO].
- [75] Sergei M Kopeikin and Gerhard Schäfer. “Lorentz covariant theory of light propagation in gravitational fields of arbitrary-moving bodies”. In: *Physical Review D* 60.12 (1999), p. 124002.

-
- [76] P. Schneider and A. Weiss. “The two-point-mass lens - Detailed investigation of a special asymmetric gravitational lens”. In: *Astronomy and Astrophysics* 164.2 (Aug. 1986), pp. 237–259.
- [77] Helmut Erdl and Peter Schneider. “Classification of the multiple deflection two point-mass gravitational lens models and application of catastrophe theory in lensing”. In: *Astronomy and Astrophysics* 268.2 (Feb. 1993), pp. 453–471.
- [78] Valerio Bozza, Silvia Pietroni, and Chiara Melchiorre. “Caustics in Gravitational Lensing by Mixed Binary Systems”. In: *Universe* 6.8 (July 2020), p. 106. DOI: 10.3390/universe6080106. arXiv: 2007.15119 [gr-qc].
- [79] GRAVITY Collaboration et al. “GRAVITY and the Galactic Centre”. In: *The Messenger* 178 (Dec. 2019), pp. 26–29. DOI: 10.18727/0722-6691/5168.
- [80] S Gillessen et al. “The orbit of the star S2 around SGR A* from very large telescope and keck data”. In: *The Astrophysical Journal* 707.2 (2009), p. L114.
- [81] Stefan Gillessen et al. “An update on monitoring stellar orbits in the galactic center”. In: *The Astrophysical Journal* 837.1 (2017), p. 30.
- [82] Event Horizon Telescope Collaboration et al. “First Sagittarius A* Event Horizon Telescope Results. I. The Shadow of the Supermassive Black Hole in the Center of the Milky Way”. In: *Astrophysical Journal, Letters* 930.2, L12 (May 2022), p. L12. DOI: 10.3847/2041-8213/ac6674.
- [83] H. Falcke and S. B. Markoff. “Toward the event horizon—the supermassive black hole in the Galactic Center”. In: *Classical and Quantum Gravity* 30.24, 244003 (Dec. 2013), p. 244003. DOI: 10.1088/0264-9381/30/24/244003. arXiv: 1311.1841 [astro-ph.HE].
- [84] A. M. Ghez et al. “The First Measurement of Spectral Lines in a Short-Period Star Bound to the Galaxy’s Central Black Hole: A Paradox of Youth”. In: *ApJL* 586.2 (Apr. 2003), pp. L127–L131. DOI: 10.1086/374804. arXiv: astro-ph/0302299 [astro-ph].
- [85] F. Eisenhauer et al. “SINFONI in the Galactic Center: Young Stars and Infrared Flares in the Central Light-Month”. In: *ApJ* 628.1 (July 2005), pp. 246–259. DOI: 10.1086/430667. arXiv: astro-ph/0502129 [astro-ph].
- [86] S. Gillessen et al. “Monitoring Stellar Orbits Around the Massive Black Hole in the Galactic Center”. In: *ApJ* 692.2 (Feb. 2009), pp. 1075–1109. DOI: 10.1088/0004-637X/692/2/1075. arXiv: 0810.4674 [astro-ph].
-

- [87] S. Gillessen et al. “An Update on Monitoring Stellar Orbits in the Galactic Center”. In: *ApJ* 837.1, 30 (Mar. 2017), p. 30. DOI: 10.3847/1538-4357/aa5c41. arXiv: 1611.09144 [astro-ph.GA].
- [88] L. Meyer et al. “The Shortest-Known-Period Star Orbiting Our Galaxy’s Supermassive Black Hole”. In: *Science* 338.6103 (Oct. 2012), p. 84. DOI: 10.1126/science.1225506. arXiv: 1210.1294 [astro-ph.GA].
- [89] A. Boehle et al. “An Improved Distance and Mass Estimate for Sgr A* from a Multistar Orbit Analysis”. In: *ApJ* 830.1, 17 (Oct. 2016), p. 17. DOI: 10.3847/0004-637X/830/1/17. arXiv: 1607.05726 [astro-ph.GA].
- [90] T. K. Fritz et al. “The Nuclear Cluster of the Milky Way: Total Mass and Luminosity”. In: *ApJ* 821.1, 44 (Apr. 2016), p. 44. DOI: 10.3847/0004-637X/821/1/44. arXiv: 1406.7568 [astro-ph.GA].
- [91] R. Schödel et al. “A star in a 15.2-year orbit around the supermassive black hole at the centre of the Milky Way”. In: *Nature* 419.6908 (Oct. 2002), pp. 694–696. DOI: 10.1038/nature01121. arXiv: astro-ph/0210426 [astro-ph].
- [92] Mark R. Morris, Leo Meyer, and Andrea M. Ghez. “Galactic center research: manifestations of the central black hole”. In: *Research in Astronomy and Astrophysics* 12.8 (Aug. 2012), pp. 995–1020. DOI: 10.1088/1674-4527/12/8/007. arXiv: 1207.6755 [astro-ph.GA].
- [93] R. Schödel, D. Merritt, and A. Eckart. “The nuclear star cluster of the Milky Way: proper motions and mass”. In: *Astronomy and Astrophysics* 502.1 (July 2009), pp. 91–111. DOI: 10.1051/0004-6361/200810922. arXiv: 0902.3892 [astro-ph.GA].
- [94] Gravity Collaboration et al. “Detection of faint stars near Sagittarius A* with GRAVITY”. In: *Astronomy and Astrophysics* 645, A127 (Jan. 2021), A127. DOI: 10.1051/0004-6361/202039544. arXiv: 2011.03058 [astro-ph.GA].
- [95] F. De Paolis et al. “The black hole at the galactic center as a possible retro-lens for the S2 orbiting star”. In: *Astronomy and Astrophysics* 409 (Oct. 2003), pp. 809–812. DOI: 10.1051/0004-6361:20031137. arXiv: astro-ph/0307493 [astro-ph].
- [96] Daniel E Holz and John A Wheeler. “Retro-MACHOs: π in the sky?” In: *The Astrophysical Journal* 578.1 (2002), p. 330.
- [97] V. Bozza and L. Mancini. “Gravitational Lensing of Stars in the Central Arcsecond of Our Galaxy”. In: *Astrophysical Journal* 627.2 (July 2005), pp. 790–802. DOI: 10.1086/430664. arXiv: astro-ph/0503664 [astro-ph].

- [98] Amitai Y. Bin-Nun. “Gravitational lensing of stars orbiting Sgr A* as a probe of the black hole metric in the Galactic center”. In: *Physical Review D* 82.6, 064009 (Sept. 2010), p. 064009. DOI: 10.1103/PhysRevD.82.064009. arXiv: 1004.0379 [gr-qc].
- [99] A. F. Zakharov et al. “Constraints on Parameters of the Black Hole at the Galactic Center”. In: *Low Dimensional Physics and Gauge Principles: Matinyan’s Festschrift. Edited by Gurzadyan V G.* Nov. 2013, pp. 264–275. DOI: 10.1142/9789814440349_0023.
- [100] Jonas Helboe Jørgensen, Ole Eggers Bjælde, and Steen Hannestad. “Probing the spin of the central black hole in the Galactic Centre with secondary images”. In: *Monthly Notices of the RAS* 458.4 (June 2016), pp. 3614–3618. DOI: 10.1093/mnras/stw546. arXiv: 1603.05856 [astro-ph.GA].
- [101] Xiao-Mei Kuang et al. “Constraining a modified gravity theory in strong gravitational lensing and black hole shadow observations”. In: *Physical Review D* 106.6, 064012 (Sept. 2022), p. 064012. DOI: 10.1103/PhysRevD.106.064012. arXiv: 2206.05878 [gr-qc].
- [102] Jitendra Kumar, Shafqat Ul Islam, and Sushant G. Ghosh. “Testing Strong Gravitational Lensing Effects of Supermassive Compact Objects with Regular Spacetimes”. In: *The Astrophysical Journal* 938.2 (Oct. 2022), p. 104. DOI: 10.3847/1538-4357/ac912c. URL: <https://doi.org/10.3847%2F1538-4357%2Fac912c>.
- [103] Jitendra Kumar, Shafqat Ul Islam, and Sushant G. Ghosh. “Investigating strong gravitational lensing effects by supermassive black holes with Horndeski gravity”. In: *The European Physical Journal C* 82.5 (May 2022). DOI: 10.1140/epjc/s10052-022-10357-2. URL: <https://doi.org/10.1140%2Fepjc%2Fs10052-022-10357-2>.
- [104] Mostafizur Rahman and Anjan A. Sen. “Astrophysical signatures of black holes in generalized Proca theories”. In: *Physical Review D* 99.2, 024052 (Jan. 2019), p. 024052. DOI: 10.1103/PhysRevD.99.024052. arXiv: 1810.09200 [gr-qc].
- [105] Rahul Kumar Walia, Sunil D. Maharaj, and Sushant G. Ghosh. “Rotating black holes in Horndeski gravity: thermodynamic and gravitational lensing”. In: *European Physical Journal C* 82.6, 547 (June 2022), p. 547. DOI: 10.1140/epjc/s10052-022-10451-5. arXiv: 2109.08055 [gr-qc].
- [106] Cheng-Yi Wang, Yu-Fu Shen, and Yi Xie. “Weak and strong deflection gravitational lensings by a charged Horndeski black hole”. In: *Journal of Cosmology and Astroparticle Physics* 2019.04 (Apr. 2019), pp. 022–022. DOI: 10.1088/1475-7516/2019/04/022. URL: <https://doi.org/10.1088%2F1475-7516%2F2019%2F04%2F022>.

- [107] F. Eisenhauer et al. “GRAVITY: getting to the event horizon of Sgr A*^{*}”. In: *Optical and Infrared Interferometry*. Ed. by Markus Schöller, William C. Danchi, and Françoise Delplancke. Vol. 7013. Society of Photo-Optical Instrumentation Engineers (SPIE) Conference Series. July 2008, 70132A, 70132A. DOI: 10.1117/12.788407. arXiv: 0808.0063 [astro-ph].
- [108] Abuter R. et al. “GRAVITY - Reaching out to SgrA* with VLTI”. In: *Highlights on Spanish Astrophysics X*. Ed. by B. Montesinos et al. Mar. 2019, pp. 609–610.
- [109] Gravity Collaboration et al. “Improved GRAVITY astrometric accuracy from modeling optical aberrations”. In: *Astronomy and Astrophysics* 647, A59 (Mar. 2021), A59. DOI: 10.1051/0004-6361/202040208. arXiv: 2101.12098 [astro-ph.GA].
- [110] Gravity Collaboration et al. “First light for GRAVITY: Phase referencing optical interferometry for the Very Large Telescope Interferometer”. In: *Astronomy and Astrophysics* 602, A94 (June 2017), A94. DOI: 10.1051/0004-6361/201730838. arXiv: 1705.02345 [astro-ph.IM].
- [111] Gravity Collaboration et al. “Detection of the Schwarzschild precession in the orbit of the star S2 near the Galactic centre massive black hole”. In: *Astronomy and Astrophysics* 636, L5 (Apr. 2020), p. L5. DOI: 10.1051/0004-6361/202037813. arXiv: 2004.07187 [astro-ph.GA].
- [112] Mark Wardle and Farhad Yusef-Zadeh. “Gravitational Lensing by a Massive Black Hole at the Galactic Center”. In: *The Astrophysical Journal Letters* 387 (Mar. 1992), p. L65. DOI: 10.1086/186306.
- [113] Michał Jaroszynski. “Gravitational Lensing and Proper Motions of Stars Surrounding the Galactic Center”. In: *Acta Astronomica* 48 (Sept. 1998), pp. 413–429.
- [114] V. Bozza and L. Mancini. “Gravitational Lensing by Black Holes: A Comprehensive Treatment and the Case of the Star S2”. In: *ApJ* 611.2 (Aug. 2004), pp. 1045–1053. DOI: 10.1086/422309. arXiv: astro-ph/0404526 [astro-ph].
- [115] Michał J. Michałowski and Przemek Mróz. “Stars Lensed by the Supermassive Black Hole in the Center of the Milky Way: Predictions for ELT, TMT, GMT, and JWST”. In: *The Astrophysical Journal Letters* 915.2, L33 (July 2021), p. L33. DOI: 10.3847/2041-8213/ac0f81. arXiv: 2107.00659 [astro-ph.GA].
- [116] V. Bozza and L. Mancini. “Observing Gravitational Lensing Effects by Sgr A* with GRAVITY”. In: *Astrophysical Journal* 753.1, 56 (July 2012), p. 56. DOI: 10.1088/0004-637X/753/1/56. arXiv: 1204.2103 [astro-ph.GA].

- [117] Fupeng Zhang, Youjun Lu, and Qingjuan Yu. “On Testing the Kerr Metric of the Massive Black Hole in the Galactic Center via Stellar Orbital Motion: Full General Relativistic Treatment”. In: *Astrophysical Journal* 809.2, 127 (Aug. 2015), p. 127. DOI: 10.1088/0004-637X/809/2/127. arXiv: 1508.06293 [astro-ph.HE].
- [118] M. Grould et al. “General relativistic effects on the orbit of the S2 star with GRAVITY”. In: *Astronomy and Astrophysics* 608, A60 (Dec. 2017), A60. DOI: 10.1051/0004-6361/201731148. arXiv: 1709.04492 [astro-ph.HE].
- [119] Idel Waisberg et al. “What stellar orbit is needed to measure the spin of the Galactic centre black hole from astrometric data?” In: *Monthly Notices of the RAS* 476.3 (May 2018), pp. 3600–3610. DOI: 10.1093/mnras/sty476. arXiv: 1802.08198 [astro-ph.GA].
- [120] Gustavo Rodríguez Coira de La Peña. “GRAVITY in the galactic center : exploring the central parsec through optical interferometry”. Theses. Université Paris sciences et lettres, Nov. 2020. URL: <https://theses.hal.science/tel-03278335>.
- [121] H. Baumgardt, P. Amaro-Seoane, and R. Schödel. “The distribution of stars around the Milky Way’s central black hole. III. Comparison with simulations”. In: *Astronomy and Astrophysics* 609, A28 (Jan. 2018), A28. DOI: 10.1051/0004-6361/201730462. arXiv: 1701.03818 [astro-ph.GA].
- [122] M. Habibi et al. “Twelve Years of Spectroscopic Monitoring in the Galactic Center: The Closest Look at S-stars near the Black Hole”. In: *The Astrophysical Journal* 847.2 (Sept. 2017), p. 120. DOI: 10.3847/1538-4357/aa876f. URL: <https://doi.org/10.3847/1538-4357/aa876f>.
- [123] F. Martins et al. “On the Nature of the Fast-Moving Star S2 in the Galactic Center”. In: *ApJL* 672.2 (Jan. 2008), p. L119. DOI: 10.1086/526768. arXiv: 0711.3344 [astro-ph].
- [124] A. Gualandris, S. Gillessen, and D. Merritt. “The Galactic Centre star S2 as a dynamical probe for intermediate-mass black holes”. In: *Monthly Notices of the RAS* 409.3 (Dec. 2010), pp. 1146–1154. DOI: 10.1111/j.1365-2966.2010.17373.x. arXiv: 1006.3563 [astro-ph.GA].
- [125] Pierre-Henri Chavanis. “Generalized thermodynamics and kinetic equations: Boltzmann, Landau, Kramers and Smoluchowski”. In: *Physica A Statistical Mechanics and its Applications* 332 (Feb. 2004), pp. 89–122. DOI: 10.1016/j.physa.2003.09.061. arXiv: cond-mat/0304073 [cond-mat.stat-mech].

- [126] M. Habibi et al. “Twelve Years of Spectroscopic Monitoring in the Galactic Center: The Closest Look at S-stars near the Black Hole”. In: *ApJ* 847.2, 120 (Oct. 2017), p. 120. DOI: 10.3847/1538-4357/aa876f. arXiv: 1708.06353 [astro-ph.SR].
- [127] Gravity Collaboration et al. “Deep images of the Galactic center with GRAVITY”. In: *Astronomy and Astrophysics* 657, A82 (Jan. 2022), A82. DOI: 10.1051/0004-6361/202142459. arXiv: 2112.07477 [astro-ph.GA].
- [128] S. Gillessen et al. “The Orbit of the Star S2 Around SGR A* from Very Large Telescope and Keck Data”. In: *ApJL* 707.2 (Dec. 2009), pp. L114–L117. DOI: 10.1088/0004-637X/707/2/L114. arXiv: 0910.3069 [astro-ph.GA].
- [129] Gravity Collaboration et al. “Detection of orbital motions near the last stable circular orbit of the massive black hole SgrA*”. In: *Astronomy and Astrophysics* 618, L10 (Oct. 2018), p. L10. DOI: 10.1051/0004-6361/201834294. arXiv: 1810.12641 [astro-ph.GA].
- [130] E. A. Becerra-Vergara et al. “Geodesic motion of S2 and G2 as a test of the fermionic dark matter nature of our Galactic core”. In: *Astronomy & Astrophysics* 641 (Sept. 2020), A34. DOI: 10.1051/0004-6361/201935990. URL: <https://doi.org/10.1051/0004-6361/201935990>.
- [131] Tuan Do et al. “Relativistic redshift of the star S0-2 orbiting the Galactic Center supermassive black hole”. In: *Science* 365.6454 (Aug. 2019), pp. 664–668. DOI: 10.1126/science.aav8137. arXiv: 1907.10731 [astro-ph.GA].
- [132] Kaj Madsen, Hans Bruun Nielsen, and Ole Tingleff. “Methods for non-linear least squares problems”. In: (2004).
- [133] Giuseppe Lodato et al. “Recent developments in the theory of tidal disruption events”. In: *Journal of High Energy Astrophysics* 7 (2015), pp. 158–162.
- [134] Z Eker et al. “Interrelated main-sequence mass–luminosity, mass–radius, and mass–effective temperature relations”. In: *Monthly Notices of the Royal Astronomical Society* 479.4 (July 2018), pp. 5491–5511. DOI: 10.1093/mnras/sty1834. URL: <https://doi.org/10.1093/mnras/sty1834>.
- [135] Event Horizon Telescope Collaboration et al. “First Sagittarius A* Event Horizon Telescope Results. VI. Testing the Black Hole Metric”. In: *The Astrophysical Journal Letters* 930.2, L17 (May 2022), p. L17. DOI: 10.3847/2041-8213/ac6756.